AN EXPERIMENTAL AND NUMERICAL STUDY OF HEAT TRANSFER AUGMENTATION NEAR THE ENTRANCE TO A FILM COOLING HOLE

Gerard Scheepers

Presented as partial fulfilment of the degree

Master of Engineering (Mechanical Engineering)

in the

Faculty Engineering, Built Environment and Information Technology

University of Pretoria

July 2007

ABSTRACT

TITLE: An experimental and numerical study of heat transfer augmentation near the entrance to a film cooling hole

AUTHOR: G. Scheepers

PROMOTERS: Mr. R.M. Morris and Prof J.A. Visser

DEPARTMENT: Mechanical and Aeronautical Engineering

DEGREE: Master of Engineering (Mechanical Engineering)

Developments regarding internal cooling techniques have allowed the operation of modern gas turbine engines at turbine inlet temperatures which exceed the metallurgical capability of the turbine blade. This has allowed the operation of engines at a higher thermal efficiency and lower specific fuel consumption.

Modern turbine blade-cooling techniques rely on external film cooling to protect the outer surface of the blade from the hot gas path and internal cooling to remove thermal energy from the blade. Optimization of coolant performance and blade-life estimation require knowledge regarding the influence of cooling application on the blade inner and outer surface heat transfer.

The following study describes a combined experimental and computational study of heat transfer augmentation near the entrance to a film-cooling hole. Steady-state heat transfer results were acquired by using a transient measurement technique in an 80 x actual rectangular channel, representing an internal cooling channel of a turbine blade. Platinum thin-film gauges were used to measure the inner surface heat transfer augmentation as a result of thermal boundary layer renewal and impingement near the entrance of a film-cooling hole. Measurements were taken at various suction ratios, extraction angles and wall temperature ratios with a main duct Reynolds number of 25×10^3*. A numerical technique, based on the resolution of the unsteady conduction*

equation, using a Crank-Nicholson scheme, was used to obtain the surface heat flux from the measured surface temperature history. Computational data was generated with the use of a commercial CFD solver.

KEYWORDS: Film-cooling, internal cooling, coolant extraction, turbine blade, heat transfer enhancement, augmentation, extraction hole, extraction angle, suction ratio, computational fluid dynamics.

ACKNOWLEDGEMENTS

The author would like to acknowledge the following individuals and institutions for their guidance and contribution to the current study:

Armscor

The South African Air Force

Prof. J.A. Visser.....The University of Pretoria

Mr. R.M. Morris.....The University of Pretoria

Dr. D.J. de Kock .....The University of Pretoria

Prof. A. Malan.....The University of Pretoria

Department of Geology.....The University of Pretoria

Mr. T.H. Roos .....Defencetek, CSIR

Mr. G.C. Snedden .....Defencetek, CSIR

Mr. S. Tuling.....Defencetek, CSIR

Mr. H. Liedberg .....Metrology Laboratory, CSIR

Dr. R. Denos .....Von Karman Institute

Dr. S. Theron.....iThemba Laboratories

Mr. B. van den Berg.....Mecalc

Mr. A. Beccaro.....Advanced Laboratory Solutions

Mr. J. Prinsloo.....National Instruments

Mr. D. Greyling.....Gemini Air

Engelhard Industries

Manserv

Master Machining

Repcal

TABLE OF CONTENTS

LIST OF FIGURES

CHAPTER 1

CHAPTER 2

CHAPTER 3

CHAPTER 4

CHAPTER 5

NOMENCLATURE

A	Area [m^2]
c'	Electrical capacitance per unit length
Cd	Discharge coefficient
C_p	Specific heat [J/kg K]
D	Hydraulic diameter [m]
$\tilde{D}$	Binary diffusion coefficient
E	Energy [kW]
EF	Enhancement factor
F	Body force
f	Friction factor
g	Gravitational acceleration [m/s^2]
h	Convective heat transfer coefficient [W/m^2K]
h_m	Mass transfer rate
i	Electrical current [A]
k	Thermal conductivity [W/m K]
l	Length [m]
LCV	Lower calorific value of fuel [kJ/kg]
$\dot{m}$	Mass flow rate [kg/s]
Nu	Nusselt number
P	Static pressure [kPa]
Pr	Prandtl number
$\dot{Q}$	Heat transfer rate [W]
r	Pressure ratio
R	Electrical resistance [Ω]
R'	Electrical resistance per unit length
Re	Reynolds number

S	Source term
s	Entropy [J/kg K]
Sh	Sherwood number
SR	Suction ratio
St	Stanton number
T	Temperature [K]
t	Time [s]
V	Velocity [m/s]
$\overline{V}$	Mean velocity [m/s]
$\dot{W}$	Work rate [W]
w	Uncertainty variable

SYMBOLS:

α	Thermal diffusivity [m^2/s]
α_T	Temperature coefficient
β	Non-dimensional heat transfer coefficient
δ	Hydrodynamic boundary layer thickness
ε	Thin-film thickness [μm]
γ	Ratio of specific heats
μ	Viscosity [kg/s m]
μ_t	Turbulent eddy viscosity
υ	Kinematic viscosity [m^2/s]
ρ	Mass density [kg/m^3]
$\sqrt{\rho ck}$	Thermal constant [$J/m^2Ks^{0.5}$]

CHAPTER 1
INTRODUCTION

Growing commercial pressure and stricter environmental regulations are putting ever increasing demands on engine designers to obtain higher levels of fuel efficiency and decrease the amount of combustion emissions. Modern developments in turbine blade cooling have provided the ability to operate gas turbines at higher turbine inlet temperatures, allowing the engine to achieve a higher thermal efficiency and power output. The thermal efficiency is defined as the ratio between the work output of the engine and the thermal energy provided by the combustion process. It is primarily influenced by the following factors [1]:

I. Compression ratio (r)

II. The turbine inlet temperature (TIT)

III. Compressor and turbine efficiencies

Advances made with regard to compressor design have extensively increased the compression ratio of modern gas turbines during the last couple of decades. A higher overall pressure ratio raises the combustor entry temperature, which in turn enhances the turbine inlet temperature at a fixed mass flow rate. This increase in pressure ratio not only contributes to higher turbine inlet temperatures but also enhances the coolant air temperature, rendering the implementation of turbine blade cooling imperative.

Turbine blade cooling makes use of film cooling to create a protective coolant film on the outer surface of the blade which reduces the amount of heat transferred by the hot gas

stream. In addition, blade cooling removes the excess heat which reaches the blade by circulating coolant air within the blade structure. The circulating coolant removes thermal energy from the internal blade wall through convection, before it is channelled through film-cooling holes to aid with external film cooling. Internal blade cooling and external film cooling are used in all high-performance production gas turbines, allowing engines to operate at turbine inlet temperatures ranging from 1650 K to 1800 K [2, 3].

Although the implementation of turbine blade cooling is vastly beneficial, it does introduce various losses. These losses include the power required for the compression and pumping of the coolant, in addition to aerodynamic and thermal losses which are introduced when the coolant enters the hot gas stream. Optimization of coolant performance and detailed knowledge of the enhancement on the external and internal surface of the blade is required to be able to accurately predict the temperature distribution throughout the wall of the blade. This enables an estimation to be made regarding the useful lifetime of a blade. An error in approximated surface temperature magnitude of 55 ºC can result in an order of magnitude change in blade life [4].

As the increase in turbine inlet temperature and compression ratio continues, blade designers attempt to implement more sophisticated and advanced cooling techniques. This requires greater understanding of these cooling techniques, their limitations and its influence on blade life. A vast amount of research has been done during the last couple of decades to determine the influence of coolant applications on blade internal and external heat transfer. However, only a limited amount of research has been done to determine the influence of coolant extraction, to aid with external cooling, on the internal surface heat transfer augmentation.

The extraction of coolant from within the blade through film cooling holes induces local heat transfer augmentation on the internal cooling channel surface, near the entrance to the film cooling hole. This local increase in surface heat transfer can primarily be attributed to coolant boundary layer renewal, due to the extraction of the warmer coolant air near the channel wall, and impinging flow further downstream.

The following dissertation describes an experimental and numerical study which was done to determine the local convective heat transfer enhancement induced by coolant extraction. The study includes the design, building and testing of an experimental rig, representing a turbine cooling passage, used to measure the convectional heat transfer near the entrance of a coolant extraction hole. Experimental investigations are done at various hole suction ratios, extraction angles and wall-to-coolant temperature ratios which fall within engine representative ranges. Near-hole surface convection results are then compared with previously published results at inverse wall-to-coolant temperature ratios.

1.1 LITERATURE REVIEW

The following literature study commences with a brief overview of the different cooling techniques which are implemented in modern gas turbine engines and a broad review of the research which has been done with regard to these cooling techniques. Studies which consider the influence of film cooling on heat transfer augmentation on the internal surface of turbine cooling channels are surveyed in detail. This is followed by a review of different experimental heat transfer measuring techniques and concluded by a proposal for the current study.

1.1.1 OVERVIEW OF COOLING TECHNIQUES

It has always been the practice to pass a quantity of cooling air over the turbine disc and blade roots to cool down the highly stressed inner core [2]. However, the term *cooled turbine* distinctively implies the application of a substantial quantity of coolant to the nozzle and rotor blades themselves. This amount of coolant air can be as high as 25% in high-performance engines [1].

The primary objective of blade cooling is to increase the lifespan of a turbine blade. Achieving this requires control of the two main parameters which affect blade life:

- The mean blade temperature level which should be kept within moderate levels with respect to the metallurgical capability of the blade.

- Thermal gradients which should be limited in order to avoid thermal fatigue and creep.

Although the objective of blade cooling is straightforward, the implementation thereof is very complex and varies from one engine manufacturer to another; to the extent that a single engine manufacturer may implement different cooling techniques for different engine types and requirements. When implementing cooling techniques, the designer has to ensure that the maximum blade surface temperatures and temperature gradients, during operation, are compatible with the maximum blade thermal stress for the life of the design.

Cooling considerations also differ between the rotor and stator sections of the engine. Rotor blades represent slightly greater challenges, since the design must take into account excessive creep and stresses induced by high rotational speeds. It should also be noted that oxidation is just as significant a limiting factor as creep. Therefore, it is important to cool unstressed components such as nozzle blades and annulus walls.

The implementation of cooling creates a fairly sensitive balance which has to be obtained, since too little cooling will result in a hotter surface area, thus resulting in reduced component life. Conversely, excessive coolant flow will lead to higher fuel consumption and may reduce overall engine performance. For a large passenger aircraft a 1% reduction in specific fuel consumption could save 560 tons of fuel per annum and reduce direct operating costs by 0.5% [5]. Hence, the optimum operational objective is to minimise compressor bleed-off, used for coolant purposes, whilst maintaining functionality of the engine and acceptable component life. This requires a greater understanding with regard to the implementation of various cooling techniques and their influence on heat transfer augmentation and pressure losses.

The design of most turbine cooling systems is proprietary in nature and therefore not readily available in open literature. However, the principal behind most cooling techniques are quite similar, regardless of the engine manufacturer or model [6]. This allows for universally applicable research to be done with regard to these methods.

Research regarding turbine blade cooling can be classified into two different approaches, i.e. the measurement of heat transfer characteristics and the numerical prediction thereof. Since the middle of the previous century, the experimental community (i.e. the measurement approach) has contributed extensively to heat transfer research regarding axial flow turbines. Advances regarding measurement techniques have been made to such an extent that time-averaged and time-resolved 3-D heat transfer data can be routinely obtained for vanes and blades [7]. Conversely, the prediction of heat transfer distributions using Computational Fluid Dynamics (CFD) has advocated that a large amount of work still needs to be done. Existing 2-D and 3-D Navier Stokes codes have shown the ability to give reasonably accurate predictions of time-averaged and unsteady pressure field distributions, but still lack the ability to generate accurate surface heat transfer distributions.

Studies with regard to turbine blade cooling can generally be divided into two categories, i.e. external and internal blade cooling. The former focuses primarily on the effect of film cooling on the external blade surface heat transfer while the latter considers the removal of heat from its internal surface with the use of internal cooling techniques such as augmented convective cooling and impingement.

The cooling arrangement on the first stage rotor and turbine blade section of a typical aircraft gas turbine is illustrated in Figure 1.1. The first stage nozzle is cooled by air extracted from the inner and outer combustion liner cavities, while coolant is provided to the rotor blade from the compressor diffuser mid-span. Augmented convective cooling, impingement cooling and film cooling are the principal turbine cooling methods, and are usually implemented in conjunction on modern engines.

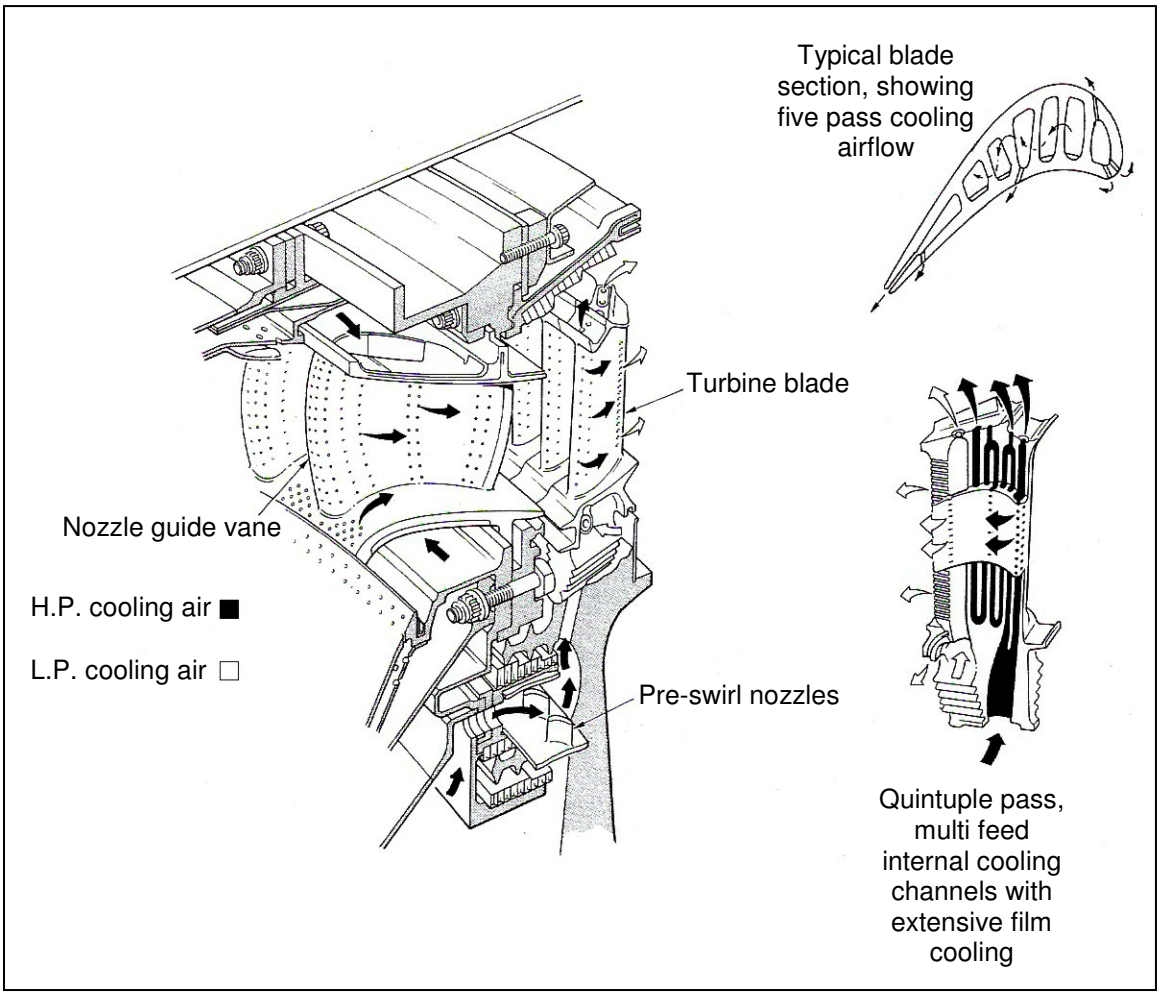

FIGURE 1.1: *Cooling arrangement of a first stage turbine and rotor blade* [1]

I. Augmented convective cooling

Coolant entering the root of the blade is directed through serpentine passages, referred to as cooling channels, thereby removing thermal energy from the channel walls through forced convection. Channel wall heat transfer enhancement by means of this method purely relies on the passage length-to-diameter ratio. As a result, turbulence promoters such as rib turbulators and pin-fins are introduced to augment the plain wall heat transfer.

Rib turbulators are easy to manufacture and provide good heat transfer augmentation. These turbulators periodically trip the boundary layer flow, as

illustrated by Figure 1.2, generating high turbulence flow near the channel wall. This enhances the surface heat transfer at the area of separation and reattachment while inducing only a minor pressure drop across the channel. Heat transfer augmentation with rib turbulators depend mainly on the geometry of the turbulator such as rib size, shape, distribution and flow-attack-angle, as well as flow parameters such as the channel Reynolds number.

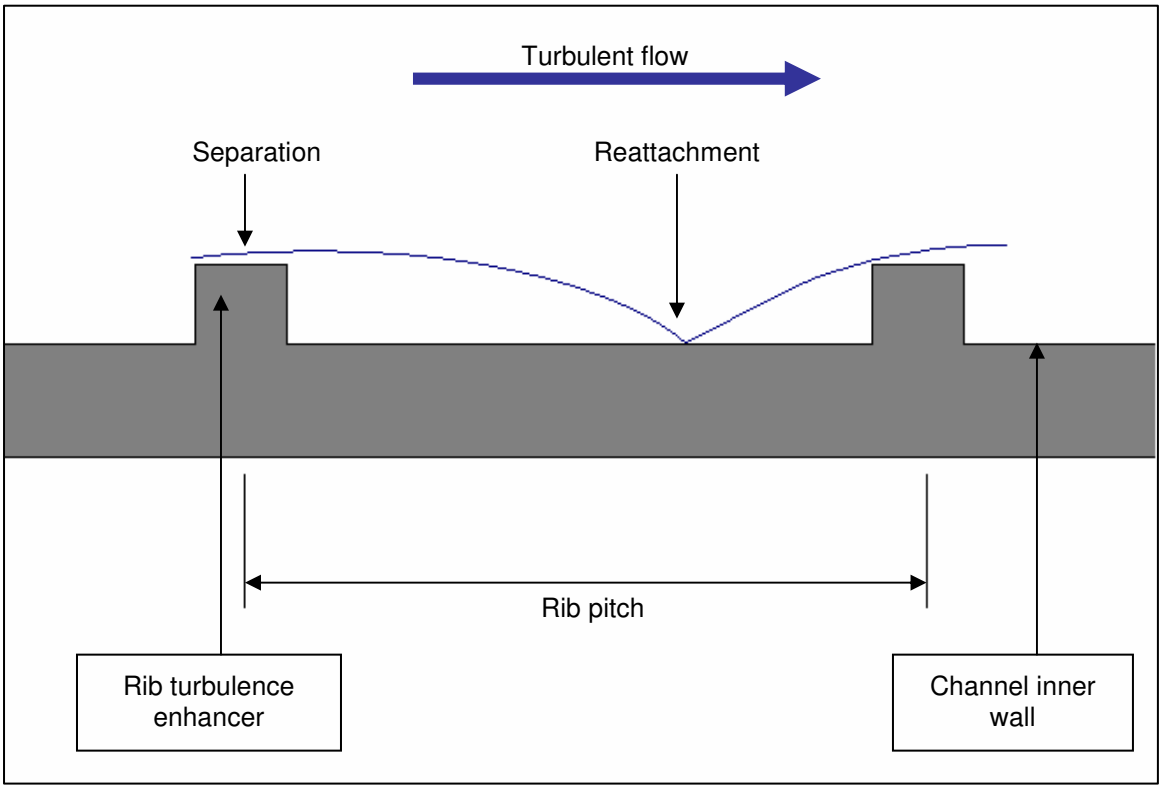

FIGURE 1.2: *Schematic illustrating flow separation induced by rib turbulators*

Pin-fins are commonly used at the narrow trailing edge of the blade where ribbed channels cannot be implemented due to manufacturing constraints. These pin-fins are orientated perpendicular to the flow direction and are typically placed in a staggered or in-line configuration. The pins not only increase the effective heat transfer area, but induce free stream turbulence, which increases the amount of convective cooling in the channel. The extent of heat transfer enhancement induced by an array of pin-fins depends primarily on the pin shape [8 -10] and its distribution and placement angle in the array [11-13].

Apart from turbulence promoters, the heat transfer in the coolant channel is also influenced by secondary flows induced by rotational effects and bends in the flow passage. Rotation generates centripetal acceleration and Coriolis forces which create a pair of counter rotating vortices in a cooling passage. These vortices redistribute the flow velocity in the passage and may enhance or decrease the heat transfer on the wall of the duct, depending on the flow direction [6, 14-16]. Figure 1.3 provides a conceptual illustration which demonstrates the effects of Coriolis and rotational buoyancy forces on the axial flow velocity profile of outward and inward flowing coolant.

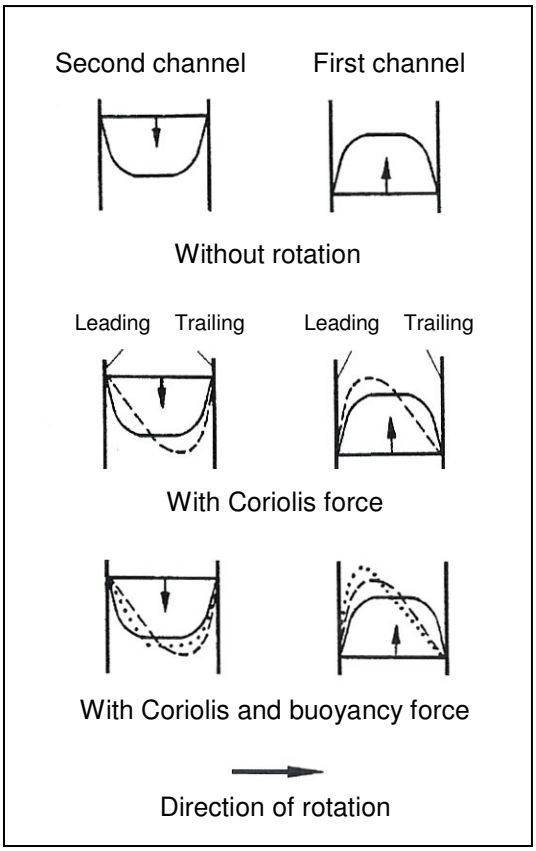

FIGURE 1.3: *Conceptual view illustrating the effect of Coriolis and rotational buoyancy on radially inward and outward flows* [16]

An extensive amount of research has been done to understand the heat transfer augmentation and pressure losses induced by various turbulator geometries and

coolant channel flow conditions. These studies have considered the influence of different rib spacings, rib layouts, rib angles, rib geometries and rib profiles on the channel heat transfer and pressure drop. Different turbulator configurations and geometries studied by Han et al. [17] are displayed in Figure 1.4. The influence of non-rectangular channels, 180º turns in serpentine passages, high-blockage-ratio ribs and the number of ribbed walls were also studied. With regard to the effects of rotation, studies have investigated the influence of rotation on smooth walled and rib turbulated passages as well as channel orientation with regard to the rotation direction. Comprehensive reviews of these studies are provided by Dunn [7] and Han et al. [6, 18, 19].

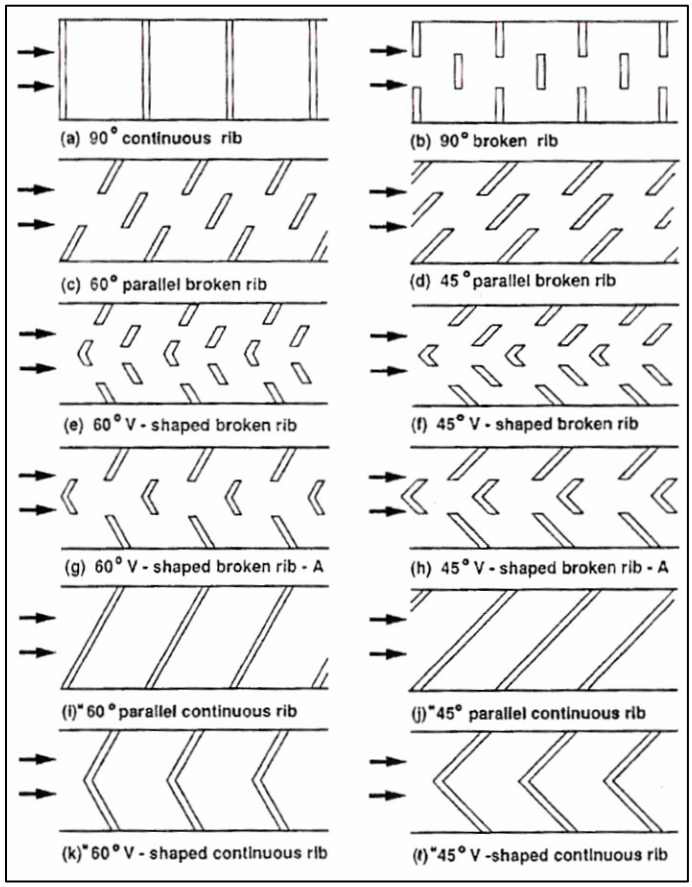

FIGURE 1.4: *Different rib configurations studied by Han et al.* [17]

II. Impingement cooling

Jet impingement is the internal cooling method with the most potential to increase the local heat transfer coefficient. With this method, coolant is directed through an array of small holes to impinge on the inner surface of the blade wall, as illustrated in Figure 1.5. Heat transfer enhancement takes place at these impingement points, from where the coolant air is then re-routed through internal channels or ejected through film-cooling holes to aid with external film-cooling. Unfortunately, the construction of these flow channels weakens the structural strength of the wall. For this reason impingement cooling is used mostly in areas such as the leading edge of rotor blades, where thermal loads are the highest and where the thicker portion of the airfoil can accommodate these cooling channels. Jet impingement is also implemented in the mid-cord region of stator blades, since the structural strength required in a stator airfoil is less than that of a rotor airfoil.

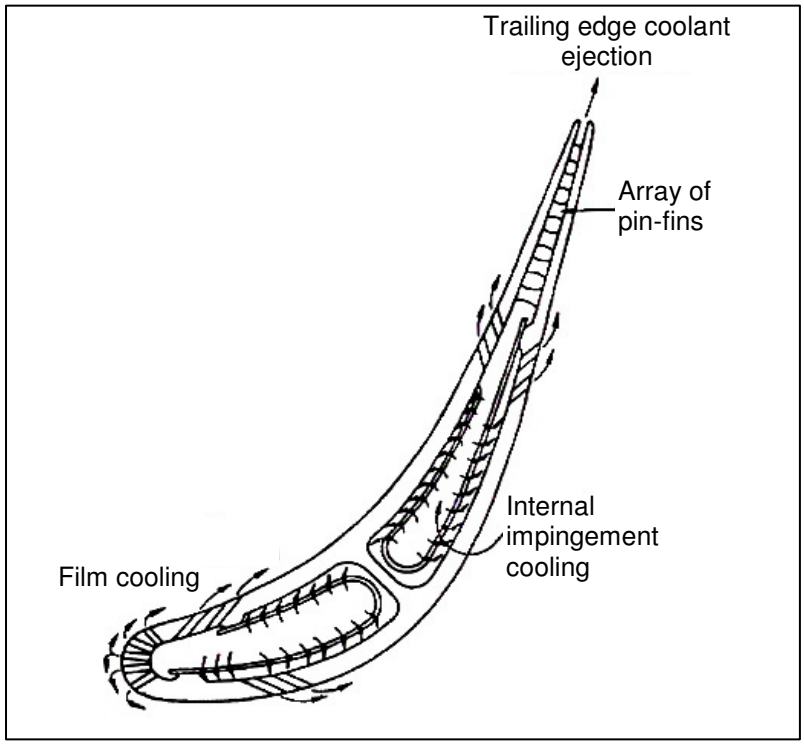

FIGURE 1.5: *Inner surface impingement* [20]

An extensive amount of design correlations for impingement cooling is available in open literature [19]. Florscheutz et al. [21, 22] and Goldstein et al. [23-25] have published research which has considered a vast array of impingement geometries and flow conditions. These studies include the influence of impingement on the mid-chord region (including the effect of cross flow) and the leading edge of the blade, where impingement on a curved surface is addressed. A comprehensive review of research which has been done with regard to jet impingement is provided by Han et al. [6].

III. Film-cooling

The main purpose of film cooling is to provide a protective coolant layer on the outer surface, as illustrated by Figure 1.6, thereby reducing the heat load on the blade. This method extracts coolant from within the blade through tiny holes at certain extraction angles to flow alongside the outer surface of the blade. The performance of external film cooling primarily depends on [18]:

I. Coolant to mainstream pressure ratio

II. Coolant to mainstream temperature ratio

III. Film-hole geometry and its location

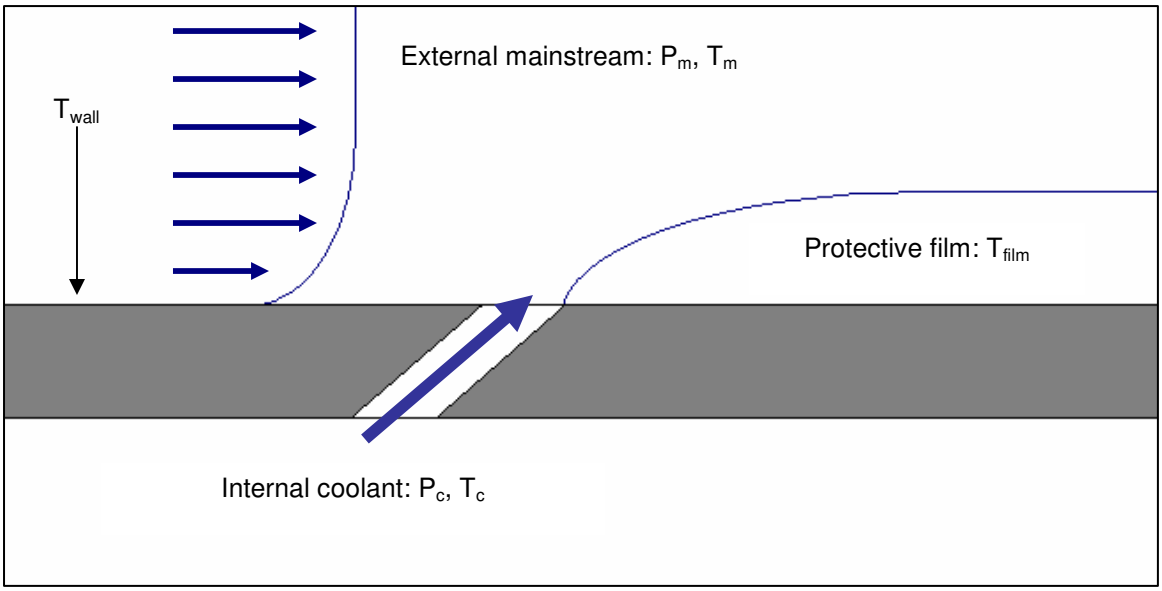

FIGURE 1.6: *Schematic illustrating the concept of external film cooling*

A vast amount of research has been done regarding these attributes [6, 7, 18, 19, 26]. This includes studies considering the injection of coolant from various blade surfaces, the effectiveness of film cooling and its influence on aerodynamic losses in addition to discharge coefficients of turbine cooling holes.

Knowledge of the discharge coefficient, *Cd*, is vital in the sizing and placement of film-cooling holes to determine whether the correct amount of coolant flow is provided to obtain the desired blowing or suction ratio (as referred to from an internal cooling perspective). The suction ratio is defined as the ratio between the coolant velocity in the film-cooling hole and the velocity in the internal cooling channel [27].

$$SR = \frac{\overline{V}_{hole}}{\overline{V}_{channel}} \qquad [1.1]$$

A suction ratio which is too low may provide inadequate reduction of the external surface heat load. Alternatively, a suction ratio which is too high might lead to the penetration of the coolant jet into the hot external free stream, which will reduce the effectiveness of the protective coolant layer. These extreme cases will both lead to a shortened blade life.

The discharge coefficient is defined as the ratio between the actual mass flow rate passing through the hole and the amount of mass which will pass through an ideal hole (neglecting any losses) [27].

$$Cd = \frac{\dot{m}_{actual}}{\dot{m}_{ideal}} \qquad [1.2]$$

Hay et al. [28] provide a comprehensive review of published data on discharge coefficients for film-cooling applications. The main geometrical parameters of a film-cooling hole which influences the discharge coefficient include:

I. Channel length

II. Inclination angle

III. Orientation

IV. Entry and exit radius

V. Hole geometry

A comprehensive study regarding the influence of external and internal cross-flow on the discharge coefficient has also been done by Gritsch et al. [29] and Hay et al. [30].

1.1.2 OVERVIEW OF PREVIOUS WORK WITH REGARD TO FILM COOLING

Contrary to internal and external cooling, a limited amount of research has focused on the influence of coolant flow extraction, to aid with external film cooling, on the internal surface convective heat transfer enhancement. Figure 1.7 shows a section of a turbine blade with film cooling holes and also the surface near the entrance of the coolant extraction hole.

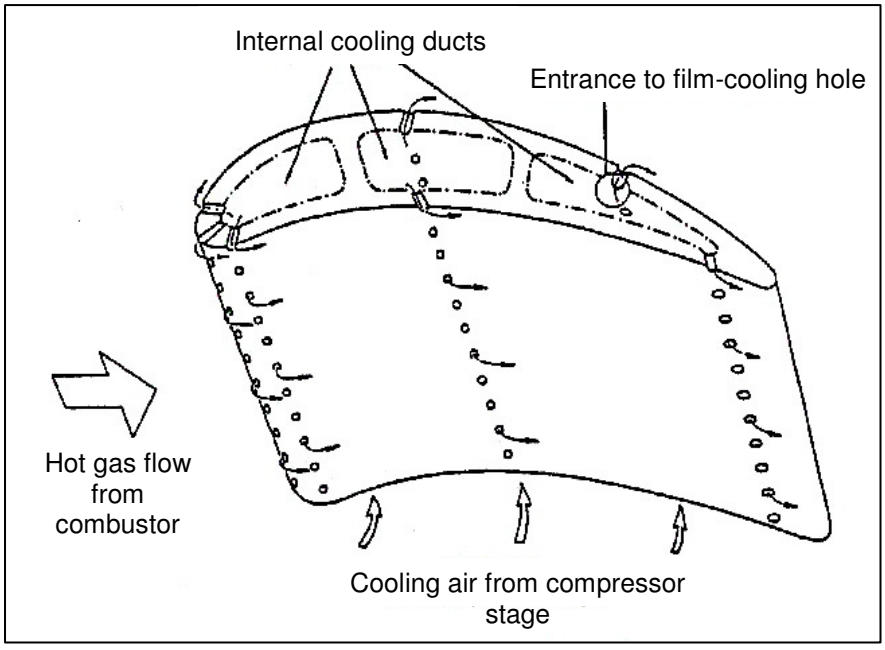

FIGURE 1.7: *Coolant extraction to aid external cooling* [27]

Studies regarding internal cooling which consider coolant extraction mostly focus on the global effect of bleed holes combined with turbulence enhancers in coolant passages [6, 18]. This implies that most of these studies do not consider the local influence of bleed hole parameters (such as suction ratio and extraction angle), in contrast to the research which has been done with regard to bleed hole discharge coefficients and external film cooling.

The influence of coolant extraction on the internal flow field can be illustrated by considering Figure 1.8, which represents a cut-away view of an internal cooling channel with a coolant extraction channel. The flow path-lines are coloured according to identity. Heat transfer enhancement takes place directly downstream of the coolant extraction hole due to the removal of the warmer boundary layer coolant. This allows cooler mainstream air to fill this void, resulting in thermal boundary layer renewal.

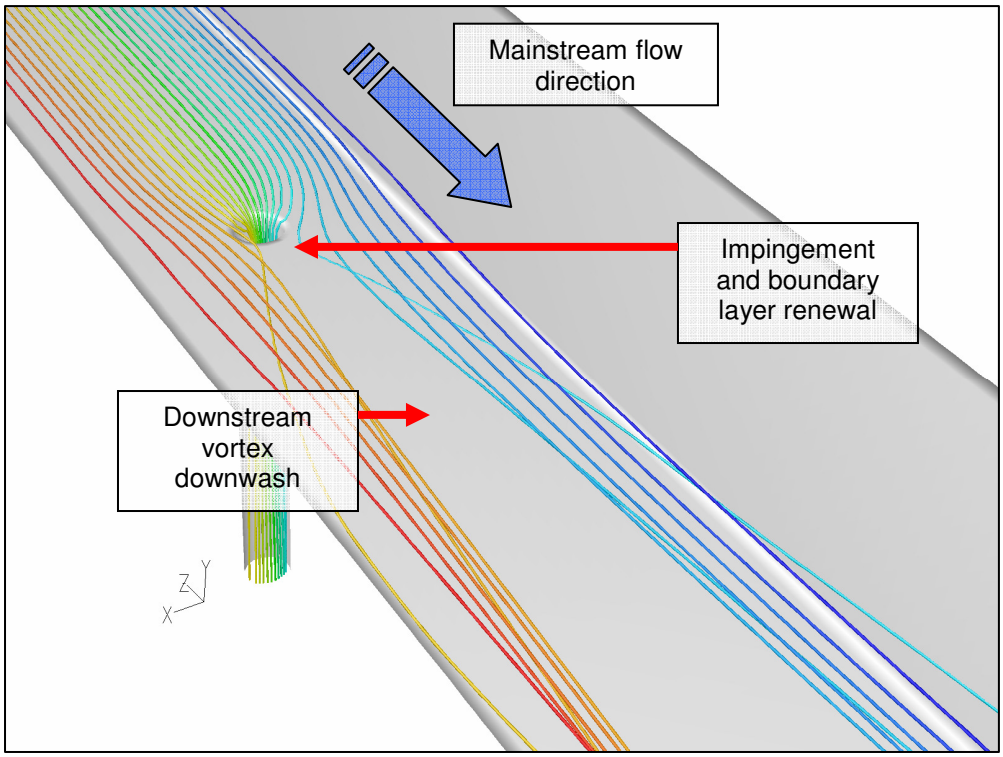

FIGURE 1.8: *Cut-away view of a square channel with coolant extraction*

Additionally, convective surface heat transfer is further enhanced by the impingement of coolant near the edge of the hole and vortex downwash, induced by the suction force, further downstream. The surface heat transfer enhancement is illustrated in Figure 1.9 which shows contours of surface heat transfer enhancement. The heat transfer augmentation induced by the extraction of coolant is clearly illustrated by the warmer contours, which indicate higher surface heat transfer values. Surface heat transfer enhancement is usually quantified by an enhancement factor, which is the ratio between the value of heat transfer in the enhanced region and the value in an unenhanced area with fully developed hydrodynamics and thermal boundary layer.

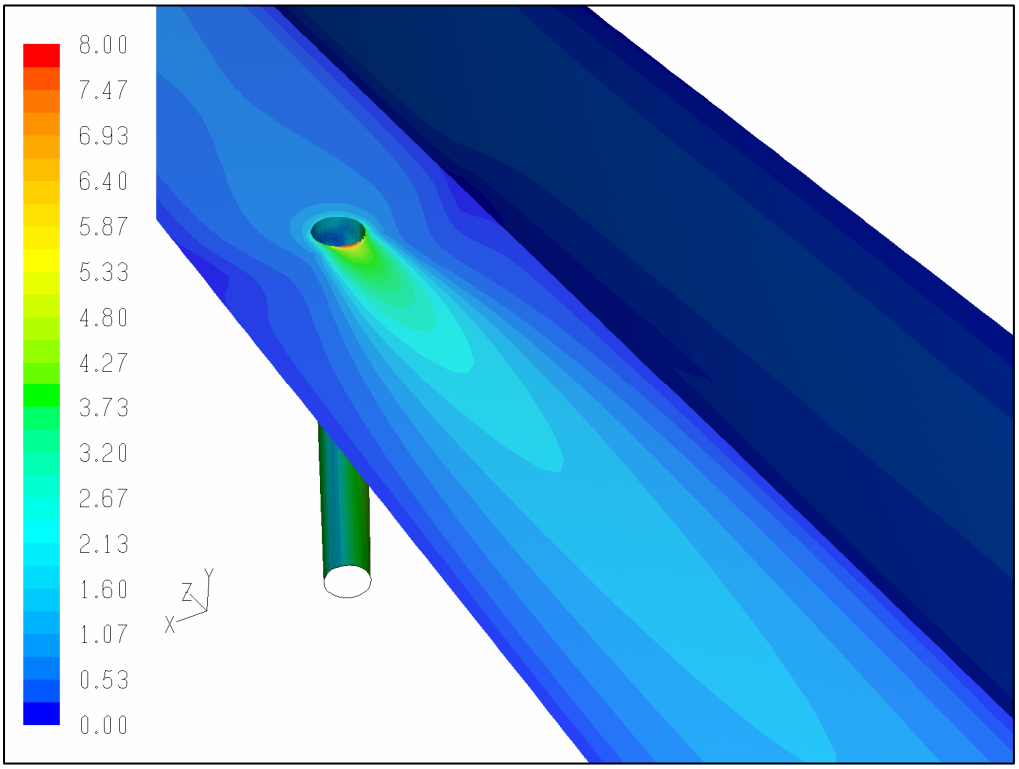

FIGURE 1.9: *Contours of heat transfer enhancement downstream of a coolant extraction hole*

One of the first publications in open literature which studied heat transfer augmentation induced by coolant extraction was that of Aintsworth et al. [31]. The study investigated the effect of mass removal through discrete holes in circular, triangular and rectangular ducts with the use of thin-film gauges. A main-channel flow velocity of Mach 0.6 was used and enhancement factors in the region of two were observed in the area directly

downstream of the hole. More importantly though, the study indicated that surface heat transfer enhancement increased proportionally with the amount of flow extracted.
Sparrow et al. [32] studied the heat transfer enhancement downstream of a perpendicular fluid withdrawal branch in a pipeline section. The study provided circumferentially averaged heat transfer enhancement values downstream of the fluid withdrawal branch. Tests were conducted at channel flow Reynolds numbers of 5 000, 10 000 and 20 000 and the suction ratio was varied between 0 and 8. Although the main-channel diameter and the extraction-channel diameter were of the same size, the study showed that heat transfer enhancement directly downstream of the fluid withdrawal branch was up to five times higher with extraction than without. The influence of the main-channel Reynolds number showed a negligible effect on the heat transfer augmentation, concluding that the amount of near-hole enhancement is primarily influenced by the suction ratio. This observation relates strongly with the findings of Aintsworth et al. [31].

An experimental study in a single channel, representative of an internal cooling passage of a turbine blade with multiple coolant extraction holes was done by Shen et al. [33]. The study made use of liquid crystal thermography to obtain detailed heat transfer enhancement contours downstream of the extraction holes. The study concluded that the heat transfer downstream of the entrance to a coolant extraction hole was insensitive to the number of holes upstream or the channel Reynolds number. Furthermore it was also shown that with the absence of suction the holes act as surface disturbances thereby affecting the heat transfer pattern. This study was further extended [34] by considering the heat transfer enhancement in a turbine cooling passage with a combination of coolant extraction holes and parallel rib turbulators. This was done with the suction ratio varying from 1.85 to 5. The results indicated that the addition of the extraction holes reduced the extent of separation downstream of the ribs. The heat transfer enhancement due to the extraction of coolant raised the average channel heat transfer coefficient by approximately 25% compared to a ribbed channel without coolant extraction. These findings relate strongly with an experimental study conducted by Taslim et al. [35]. This study also made use of liquid crystal thermography to measure area-averaged Nusselt numbers in a single-pass trapezoidal channel, representing a trailing edge coolant cavity.

The channel wall was roughened with tapered turbulators and tests were conducted with and without coolant extraction at various Reynolds numbers.

Ekkad et al. [36] also made use of a liquid crystal measuring technique to obtain detailed heat transfer results in a two-pass channel with parallel, angled and V-shaped rib turbulators. Tests were conducted with and without coolant extraction. In contrast to the studies conducted by Shen et al. [34] and Taslim et al. [35], the results indicated that the bleed holes increased the heat transfer coefficient in the near-hole region, but did not enhance the area-averaged heat transfer in the two-pass channel. This conclusion is thought to be due to the low suction ratio ($SR = 0.8$) which was used in the study.

Thurman et al. [37] studied the influence of the rib turbulator and extraction hole placement on convective heat transfer in cooling passages. The study implemented a liquid crystal measuring technique to obtain detailed heat transfer contours in a three-pass channel with parallel rib turbulators and coolant extraction holes in the first channel. Rib turbulators were placed at two different positions relative to the coolant extraction holes. The first case study considered an equidistant placement between the ribs and the extraction holes, while in the subsequent study the rib turbulators were placed directly upstream of the coolant extraction holes. The results showed an overall increase in heat transfer with the implementation of coolant extraction, which relates with the findings of Shen et al. [34] and Taslim et al. [35]. Furthermore, the study showed an increase in heat transfer when the coolant extraction hole is placed directly downstream of the rib turbulator, thereby decreasing the amount of flow separation.

An experimental study regarding the flow characteristics and heat transfer in a two-pass channel with coolant extraction was conducted by Chanteloup et al. [38]. Wall heat transfer measurements were done with a liquid crystal measuring technique and flow profiles were measured with a stereoscopic digital Particle Image Velocimetry (PIV) system. Both passages of the test channel were laid out with 45° rib turbulators and the second passage with coolant extraction holes. The study showed that varying the amount of coolant extraction from 30% to 50% of the total inlet mass flow of the channel does not show any variation in the area-averaged heat transfer.

The studies which were considered above indicated that significant heat transfer enhancement does occur near the film-cooling hole entrance and that this augmentation is relatively independent of upstream flow conditions, channel Reynolds number and supplementary hole interaction. It was shown that the local heat transfer near the entrance to the coolant extraction hole is primarily influenced by the cooling hole suction ratio and the placement of the coolant extraction hole relative to the upstream rib turbulator.

The first, and to the knowledge of the author, the only study which focused solely on near-hole heat transfer augmentation in a cooling passage was conducted by Byerley [27]. This study made use of a one-pass cooling channel with a single coolant extraction hole and investigated the near-hole heat transfer augmentation at various suction ratios and extraction angles with the use of a transient liquid crystal measuring technique. Tests were conducted at a channel Reynolds number of 25 000 and coolant extraction angles of 60°, 90° and 150° were considered. The suction ratio of the coolant extraction hole was varied from 0 to 7.5. Detailed contours of the near-hole heat transfer enhancement were obtained at the above-mentioned conditions with local enhancement factors as high as 6.3, measured directly downstream of the coolant extraction hole. Furthermore, the study indicated that the amount of heat transfer enhancement near the 60° and 90° extraction hole was similar, in contrast to the 150° extraction hole which was considerably lower. The study also showed that the amount of near-hole heat transfer augmentation increased in relation to the amount of coolant extraction up to a suction ratio of 5.

The study conducted by Byerley [27] obtained valuable and comprehensive results regarding the heat transfer near the entrance to the coolant extraction hole. However, certain areas of uncertainty still remain:

I. The majority of the experimental studies which were considered made use of liquid crystal thermography to measure the amount of heat transfer. Although this measuring technique provides detailed contours of surface heat transfer, it limits the wall temperature at which tests can be conducted. The experimental studies

conducted by Byerley [27], Shen et al. [33, 34], Ekkad et al. [36] and Chanteloup et al. [38] made use of heated coolant air in a cooled test channel to compensate for the wall temperature limitation of this experimental method. This implies that thermal energy is transferred towards the wall instead of being extracted as is the case with an actual turbine blade-cooling passage. Assuming that the absolute $T_{wall}/T_{coolant}$ gradient is representative of an actual cooling passage, this method should provide an adequate approximation of the absolute convective heat transfer enhancement in a channel without coolant extraction.

The heat transfer augmentation near the entrance to a coolant extraction hole is however, influenced by boundary layer renewal and vortex downwash further downstream of the extraction hole which may be affected by the density gradient in the near-wall region. In an actual turbine blade-cooling passage, the extraction of thermal energy from the blade wall will result in a boundary layer coolant with a lower density than that of the bulk coolant. Uncertainty exists regarding the influence of an inverted boundary layer density on the near-hole heat transfer and turbulent downwash further downstream of the coolant extraction hole.

II. The experimental studies conducted by Taslim et al. [35] and Thurman et al. [37] also made use of liquid crystals to measure heat transfer enhancement by blowing coolant at an ambient temperature into a heated channel. Although the coolant boundary layer density is representative of that in an actual turbine blade-cooling passage (i.e. the boundary layer density is lower than the mainstream coolant density), the thermal gradient across the boundary layer is fairly small due to the lower wall-to-coolant temperature ratio (wall temperatures less than 60°C). It is uncertain whether the wall-to-coolant temperature ratio will have a considerable effect on the near-hole heat transfer augmentation.

III. The study conducted by Byerley [27] made use of a rectangular experimental channel with sidewalls which were widened to neglect any interaction between the channel sidewalls and the coolant flow. Whether the sidewalls will influence downstream heat transfer augmentation is also uncertain.

A computational study was also conducted by Byerley [27]. This study compared numerically predicted centre-line heat transfer enhancement values, downstream of the coolant extraction hole, with the experimental results obtained in the same study. A commercial CFD package was used to simulate the near-hole heat transfer and flow physics. The computational capability at the time limited the numerical domain to 10 000 cells. The k-ε turbulence model was used on an unstructured grid, discretised to attempt to solve within the flow boundary layer. A reasonable comparison between the numerically predicted and experimentally measured heat transfer results was obtained. The numerical results indicated that the computational model tends to underpredict the heat transfer enhancement directly downstream of the coolant extraction hole and overpredict the amount of enhancement further downstream.

Rigby et al. [39] conducted a more detailed computational study of heat transfer and coolant flow in a cooling passage with parallel rib turbulators and coolant extraction. The numerical domain and boundary conditions of the numerical study was representative of the experimental channel used in the study which was conducted by Ekkad et al. [36]. The study made use of the k-ω turbulence model on a multi-block structured grid, with a grid resolution in the near-wall region which provided a y^+ value near unity. The numerical results showed excellent agreement with the experimental data when comparing the heat transfer enhancement downstream of the coolant extraction hole. The results did however underpredict the amount of heat transfer on top of the ribs.

1.1.3 OVERVIEW OF HEAT TRANSFER MEASUREMENT TECHNIQUES

The purpose of the current experimental investigation is to measure the amount of thermal energy which is being transferred from a heated wall. Consider the control volume represented by Figure 1.10 which illustrates the transfer of thermal energy from the surface of a heated wall to a fluid. The movement of thermal energy from the wall is known as heat transfer and can be described by Equation 1.3, which is derived from the

first law of thermodynamics [40]. It is assumed that negligible work is done during the transfer of thermal energy and that the energy transfer is achieved with the three different modes of heat transfer; namely conduction, convection and radiation.

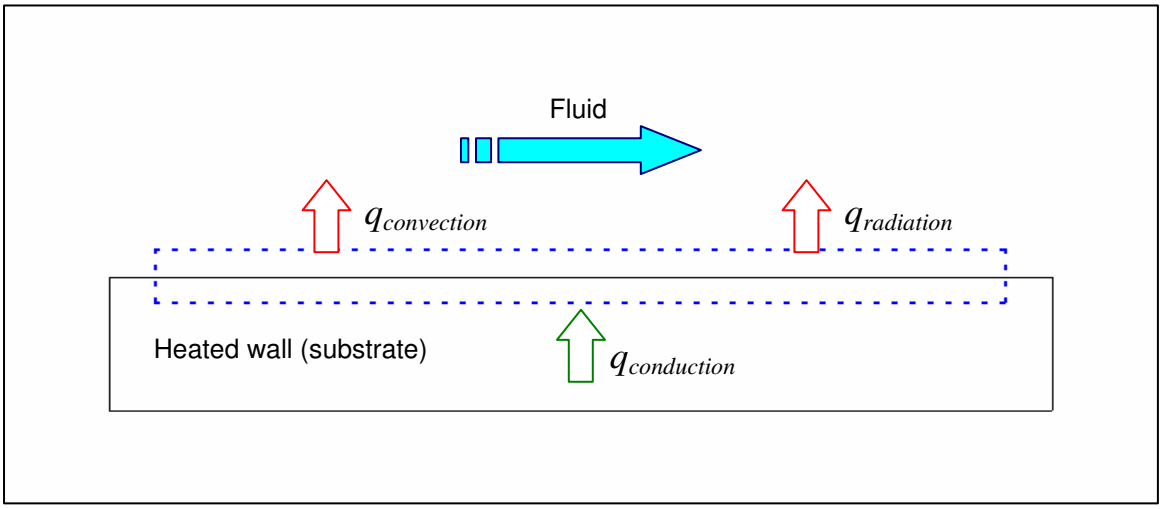

FIGURE 1.10: *Thermal energy transferred across a control volume*

$$mC_p \frac{\partial T}{\partial t} = \dot{q}_{convection} + \dot{q}_{radiation} - \dot{q}_{conduction} \qquad [1.3]$$

The term m represents the mass of the system and C_p the corresponding specific heat.

The heat transfer measuring techniques which were reviewed are the following:

I. Mass transfer analogy

II. Liquid crystal thermography

III. Heat flux gauges

Comparisons are made regarding viability, accuracy and its applicability regarding the requirements of the current study.

1.1.3.1 MASS TRANSFER ANALOGY

A multitude of mass transfer analogy techniques are available to determine heat transfer. These methods range from foreign gas concentration sampling, swollen polymer techniques, ammonia-diazo surface flow visualisation, and naphthalene sublimation. The last method was considered since it is the most popular mass transfer technique and also the most thoroughly documented method.

Naphthalene sublimation provides the ability to determine heat transfer coefficients by measuring the amount of naphthalene which sublimates when the surface is exposed to a certain flow field. The amount of mass which is lost due to sublimation can be related to the amount of thermal energy which is removed during heat transfer by means of forced or natural convection. A relation can be made between the mass and heat transfer by taking into account the different properties and assuming that the turbulent transport and boundary conditions are similar.

The local mass transfer coefficient can be determined from the rate of mass transfer per unit surface area and the difference between the local naphthalene vapour and its corresponding bulk density.

$$h_m = \frac{\dot{m}''}{\rho_{vapour} - \rho_{bulk}} \qquad [1.4]$$

The mass transfer value which is determined can then be represented in a dimensionless form as the Sherwood number:

$$S_h = h_m \frac{D}{\tilde{D}} \qquad [1.5]$$

where the term D represents the hydraulic diameter of the channel and $\tilde{D}$ the binary diffusion coefficient. The binary diffusion coefficient is a relation between the kinematic viscosity of air and the Schmidt number for naphthalene. The heat-mass transfer analogy

grants the assumption that the Sherwood number is analogous to the Nusselt number for similar conditions, $S_h \approx N_u$ [6].

This technique has been successfully implemented by Goldstein et al. [41-43] who used this method to study turbine blade endwall and external film-cooling heat transfer. Furthermore, this technique has been extensively used for internal cooling experiments by Han et al. [44] and heat transfer in rotating channels [45-47]. The naphthalene sublimation technique provides fairly high surface resolution results, although to obtain the required accuracy it requires long testing periods. Its toxicity and temperature sensitivity requires adequate safety apparatus and a temperature controlled-environment which increases its cost [48].

1.1.3.2 LIQUID CRYSTAL THERMOGRAPHY

Liquid crystals are also referred to as thermochromic crystals since they reflect different colours over a reproducible temperature range. By applying these crystals to a transparent surface, detailed high resolution surface temperature distributions can be obtained with the use of image processing. At any particular temperature, liquid crystals reflect a single wavelength of light. A change in temperature provides a sharp and precise change in colour according to which the crystals can be calibrated.

The substrate material typically used for transient experimental applications is *Plexiglas*. For a given substrate thickness and exposure time, the substrate can be assumed to represent a semi-infinite solid. Consequently, a change in wall temperature can be related to the time and thermophysical properties of the substrate to determine the convective heat transfer coefficient.

$$\frac{T_w - T_0}{T_c - T_0} = 1 - e^{(\beta^2)} erfc(\beta) \qquad [1.6]$$

where:

$$\beta = h\left(\frac{t}{\rho C_p k}\right)^{1/2} \qquad [1.7]$$

T_w represents the wall temperature at any instant in time at every pixel location, while T_0 is the initial temperature of the wall before blowdown commences. The coolant temperature is represented by T_c.

Liquid crystal thermography is one of the more popular techniques used to study internal cooling channel heat transfer [27, 33, 34]. Although this technique provides high-resolution surface temperature results, it requires an intensive calibration process as the entire surface temperature distribution needs to be captured at any particular instant in time. Noted calibration curve problems also exist with the light and camera conditions [6]. A limitation regarding the maximum permissible wall temperature is associated with this technique.

1.1.3.3 HEAT FLUX GAUGES

The implementation and development of heat flux gauges started in the early 1950s to provide a heat flux measuring capability for short-duration experimental applications which relied on high Mach number flows such as shock tubes [49]. Although various gauges with different manufacturing and operating theories evolved over the following couple of decades, the basic principle remained the same. The gauge acts primarily as a Resistance Temperature Device (RTD), consisting out of a very thin metal element (negligible heat capacity) which is bonded, painted or evaporated onto the surface of an insulating substrate. When the substrate surface is subjected to a change in the temperature field, a properly calibrated gauge can be used to accurately determine the surface temperature history of the substrate.

Consider the control volume represented by Figure 1.11 which illustrates the transfer of thermal energy from the surface of a heated wall, with an attached thin-film gauge, to a fluid. For a short enough experimental timeframe and a sufficiently thick insulation substrate, it can be assumed that the heat transfer out of the substrate is one-dimensional. This implies that the thermal flux does not reach the outer surface of the material during the measurement period, thus representing a semi-infinite solid [50]. Implementing existing theory for transient heat conduction in a non-homogenous body, the heat flux across the substrate surface can then be determined.

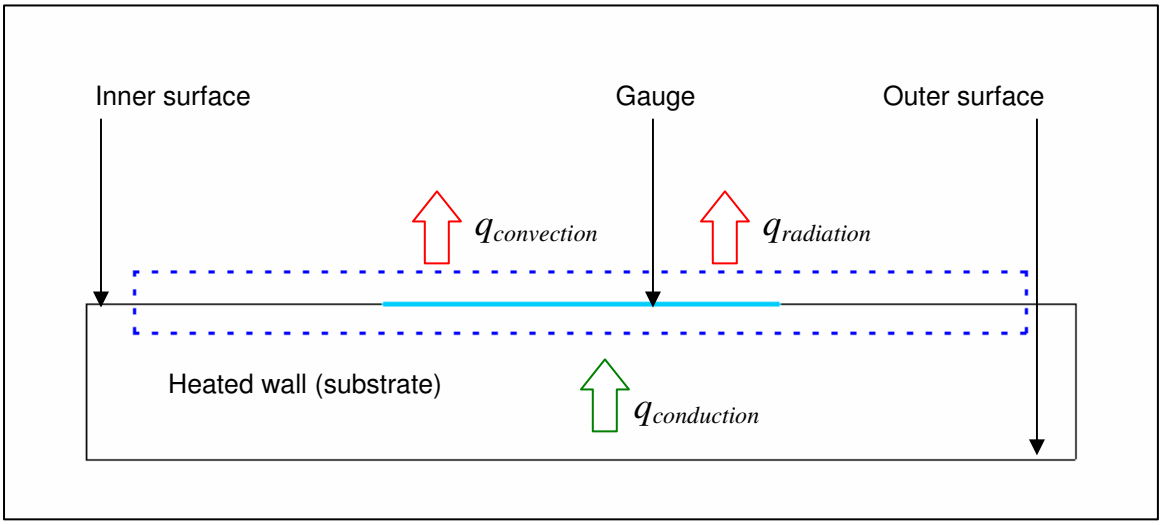

FIGURE 1.11: *Thermal energy transferred across a control volume*

A typical wall heat flux versus surface temperature profile obtained with this method is displayed in Figure 1.12. Assuming that the substrate represents a semi-infinite body, the linear regression line can be extrapolated to obtain a steady heat flux value. Figure 1.13 is an illustration of a *Macor* ceramic substrate laid out with platinum thin-film gauges and gold connection leads. These gauges are applied flush onto a polished substrate surface with the low-resistance leads connecting the gauge to a data-acquisitioning system. Platinum is the most popular gauge film material since its resistance temperature curve is linear (within the temperature range under consideration), which simplifies the calibration process.

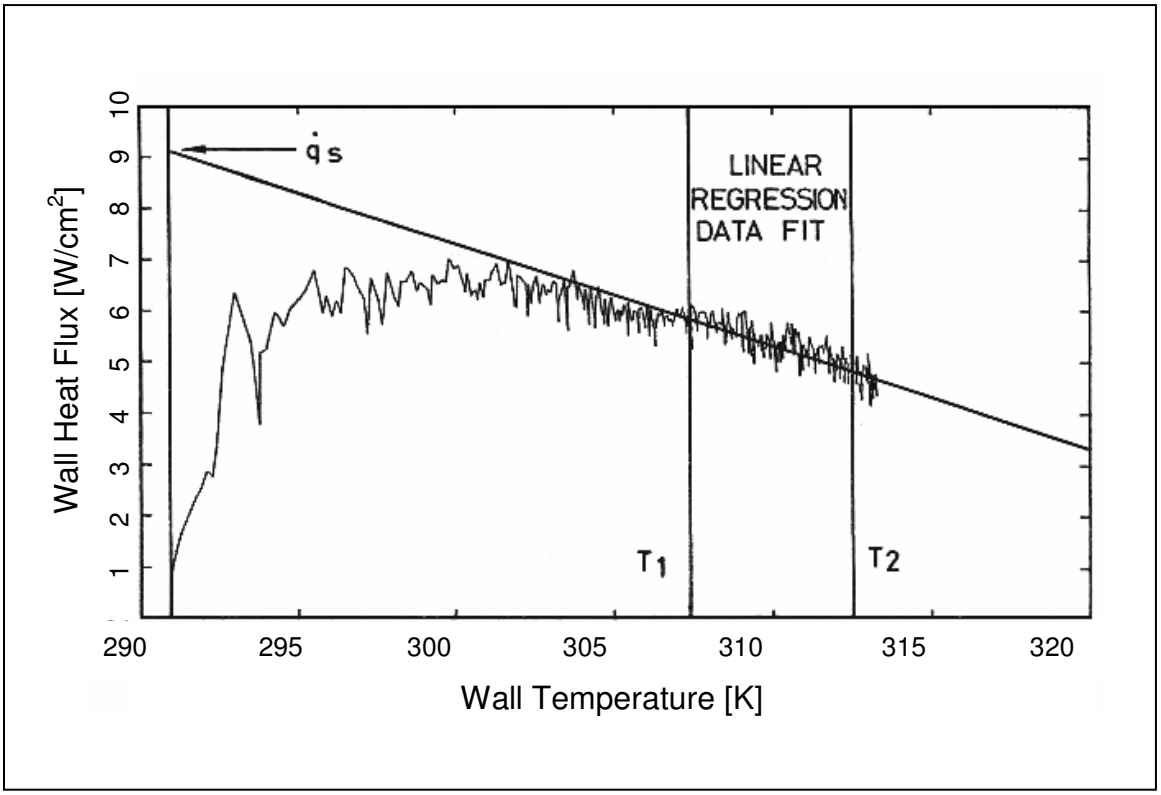

FIGURE 1.12: *Typical surface heat transfer and temperature output obtained with the heat flux measuring technique* [50]

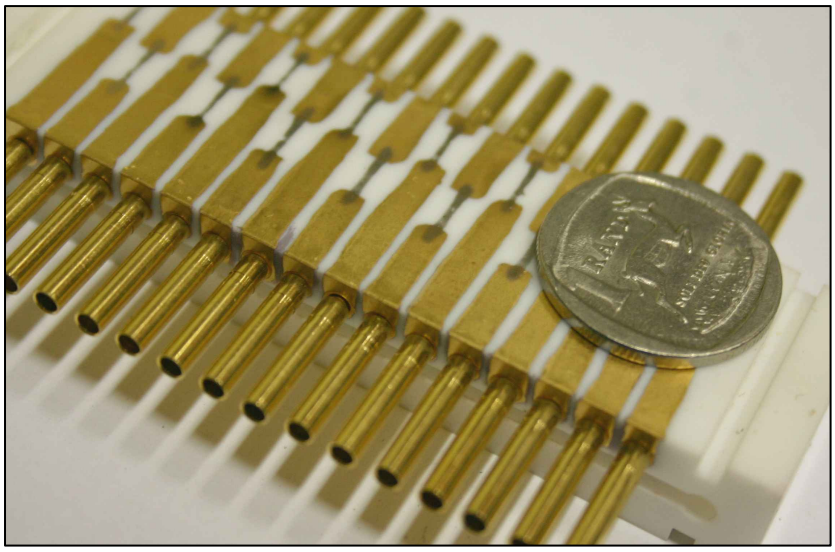

FIGURE 1.13: *Platinum thin-film gauges fired onto a Macor ceramic substrate (The diameter of the coin is approximately 20 mm)*

This measurement technique has been successfully implemented at various research institutes including the Von Karman Institute [49-53]. Although this method does not provide high-resolution surface temperature results, since local measurements are taken, it provides the ability to test at higher substrate wall temperatures in comparison with the other measurement techniques which were discussed.

1.1.4 PROPOSAL FOR THE CURRENT STUDY

The literature study primarily considered research which has been done with regard to heat transfer augmentation near the entrance of a coolant extraction hole. The review indicated that although extensive research has been done with regard to internal and external blade cooling; only a limited number of studies have examined the influence of coolant extraction on the local heat transfer augmentation on the internal surface of a turbine blade cooling channel. Furthermore the review indicates that:

I. Boundary layer renewal and coolant impingement contributes to extensive heat transfer enhancement downstream of the coolant extraction hole [27, 31-37].

II. The amount of local heat transfer enhancement increases up to a certain suction ratio [9, 32, 34, 38].

III. The main channel Reynolds number and supplementary hole interaction has a negligible effect on the local heat transfer enhancement [27, 32].

IV. The angle of coolant extraction influences the local heat transfer enhancement for extraction angles higher than 90º [27].

In Section 1.1.2 certain uncertainties with regard to these previous studies were highlighted. With the current study, the aim is to contribute to this research and resolve the uncertainties regarding:

I. The influence of higher wall-to-coolant temperature ratios and its influence on the amount of enhancement near the augmented area at different suction ratios and extraction angles.

II. The influence of the channel sidewall on the downstream heat transfer augmentation i.e. the ratio between the suction hole diameter to the main channel hydraulic diameter.

III. Determine whether the reversed boundary layer density, applied in the results of Byerley [27], had any influence on the near-hole enhancement factor or augmentation footprint.

The current study proposes to answer these uncertainties by investigating the heat transfer augmentation near the entrance to a film-cooling hole in a square cooling passage at:

I. Suction ratios ranging from 0 to 5

II. Wall-to-coolant temperature ratios of 1.3 and 1.4

III. Coolant extraction angles of 90° and 150°

In Section 1.1.3 various experimental heat transfer measuring techniques were reviewed. The transient thin-film measurement approach will be adopted as the heat transfer measurement technique in the current study. The rationale behind this decision is that the thin-film measuring technique is the most accurate method to determine heat transfer at realistic wall-to-coolant temperature ratios.

Furthermore, a commercial finite volume code will also be used to numerically simulate the experimental domain. The numerical modelling of coolant extraction requires accurate modelling of boundary layer renewal and flow impingement downstream of the film cooling hole entrance. Although promising studies have been performed with Large Eddy Simulation (LES) turbulence models on internal cooling passages without coolant extraction [54, 55], it is not yet employed in routine design simulations [56]. Consequently, in this study it was decided to solve the Reynolds Averaged Navier-Stokes

(RANS) equations with standard wall functions. A derivative of the LES model was also used to asses its ability to predict the subsequent flow field and heat transfer augmentation.

The aim of the numerical investigation is to provide more detail regarding the near-hole flow patterns and thermal interaction. Furthermore, to provide an indication of the degree of accuracy with which a wall function approach can predict the heat transfer augmentation induced by coolant extraction.

1.2 CONCLUSION

In the current chapter the background regarding internal cooling and its influence on the efficiency of a gas turbine was discussed. A literature survey considered the different cooling techniques implemented on modern gas turbines and a broad overview of the research which has been done with regard to these techniques. A detailed survey was done with regard to studies which considered heat transfer augmentation near the entrance to coolant extraction holes. Furthermore, various experimental heat transfer measuring techniques were discussed. The chapter concluded with a proposal for the current study.

In Chapter 2, the governing equations regarding one-dimensional heat transfer measurement are discussed. This forms the foundation of the experimental technique used in the current study.

Chapter 3 discusses the experimental process in detail. This includes a description of the experimental rig, gauge-manufacturing process, instrumentation, uncertainty analysis and testing procedure.

In Chapter 4, the considerations regarding the numerical investigation are presented. This includes a discussion of the governing numerical equations, turbulence modelling, near-wall treatment and the numerical model.

Chapter 5 will present the experimental results and draw a comparison between previously published results and the numerical predictions.

The study is concluded in Chapter 6 and recommendations for further work are provided.

CHAPTER 2
HEAT TRANSFER MEASUREMENT

2.1 PREAMBLE

Estimating the life of a turbine blade requires knowledge of the surface temperatures and thermal gradients within the blade. This can be obtained by solving the conduction equation iteratively throughout the blade wall, with the inner and outer surface temperatures as boundary conditions. A final result will be obtained by updating the solution after each iteration, until the heat flux due to internal and external convection and the conduction through the blade wall reaches equilibrium.

The convective heat transfer on the inner and outer surface of the blade can be estimated with the use of experimental correlations. If the gas temperature and wall temperature are also known, or assumed during the initial approximation, then the heat flux can be determined with the use of Equation 2.1.

$$\dot{q}_{wall} = h(T_{gas} - T_{wall}) \qquad [2.1]$$

The convective heat transfer values on the surface of the blade are usually presented dimensionless to provide similarity regarding the representation of experimental results or correlations. The dimensionless representation is done either through a Nusselt number, defined by Equation 2.2:

$$Nu = \frac{\dot{q}_{wall} D}{(T_{gas} - T_{wall}) k_{gas}} = \frac{hD}{k_{gas}} \qquad [2.2]$$

or the Stanton number which can also be defined as a function of the Nusselt number:

$$St = \frac{h}{\rho C_p V} = \frac{Nu}{RePr} \qquad [2.3]$$

An alternative expression, used for measurements in internal cooling channels, is the enhancement factor, defined by Equation 2.4. The enhancement factor is the ratio between the surface heat transfer coefficient in an enhanced region, and a surface heat transfer coefficient in an unenhanced region with a fully developed flow and thermal boundary field. The enhancement factor thus provides an indication of the relative augmentation in convective heat transfer.

$$EF = \frac{h_{enhanced}}{h_0} \qquad [2.4]$$

Experimental measurements within turbine cooling channels provide the designer with the convective heat transfer coefficient on the inner surface of the blade. The flow and temperature characteristics of the experimental setup should be representative of those encountered in a real engine to ensure that useful data is obtained. These flow and temperature characteristics refer to properties such as the flow Reynolds number, Mach number and wall-to-coolant temperature ratio. Correlations can then be established as a function of these properties for various internal flow conditions.

2.2 GOVERNING EQUATIONS TO THE ANALYTICAL SOLUTION

Two factors contribute to thermal equilibrium when considering one-dimensional thermal propagation through a substrate. The first being the heat transferred via conduction into the substrate at a certain depth *x* and time *t*, which can be described as:

$$Q_{conduction(x,t)} = -kAl\frac{\partial^2 T_{(x,t)}}{\partial x^2} \qquad [2.5]$$

The second factor is the heat transferred due to thermal inertia of the substrate:

$$Q_{inertia(x,t)} = V\rho C_p \frac{\partial T_{(x,t)}}{\partial t} \qquad [2.6]$$

The familiar one-dimensional unsteady heat conduction equation is obtained when Equation 2.5 and Equation 2.6 are combined:

$$\frac{\partial T_{(x,t)}}{\partial t} = \alpha \frac{\partial^2 T_{(x,t)}}{\partial x^2} \qquad [2.7]$$

The term $\alpha = k/\rho C_p$ is known as the thermal diffusivity and represents the ratio between the thermal conductivity and the volumetric heat capacity of the substrate. The larger the thermal diffusivity, the faster temperature changes will propagate through the substrate. Consequently, the further the heat flux will penetrate after a specific time of abrupt exposure to the coolant.

The heat flux at the surface of the substrate is defined as:

$$\dot{q}_{(x=0,t)} = -k\left(\frac{dT_{(t)}}{dx}\right)\Bigg|_{x=0} \qquad [2.8]$$

An analytical solution for Equation 2.7 can be found by implementing a Laplace transformation, where the Laplace variable is expressed by $p=e^{\sigma+j\omega}$. The terms σ and ω represent real values [51].

$$T_{(x,p)} = \frac{\bar{\dot{q}}_{(x,p)}}{\sqrt{\rho C_p k}\sqrt{p}} e^{-x\sqrt{p/\alpha}} \qquad [2.9]$$

At the substrate wall ($x = 0$), it follows that:

$$T_{(x=0,p)} = \frac{\bar{\dot{q}}_{(x=0,p)}}{\sqrt{\rho C_p k}\sqrt{p}} \qquad [2.10]$$

The constant $\sqrt{\rho C_p k}$ is known as the thermal product.

By using the convolution theorem [57], the inverse Laplace transformation in the time domain can then be obtained and expressed as:

$$T_{(x=0,t)} = \frac{1}{\sqrt{\pi}\sqrt{\rho C_p k}} \int_0^t \frac{\dot{q}_{(x=0,t)}(\tau)}{t-\tau} d\tau \qquad [2.11]$$

Equation 2.11 describes the variation of surface temperature with time, assuming:

I. The substrate is semi-infinite.

II. The heat transfer into the substrate is one-dimensional.

Rewriting Equation 2.11 for the wall heat flux as a function of time and wall temperature gives:

$$\dot{q}_{(x=0,t)} = \sqrt{\frac{\rho C_p k}{\pi}} \left[\frac{T(t)}{\sqrt{t}} + \frac{1}{2} \int_0^t \frac{T(t)-T(\tau)}{(t-\tau)^{3/2}} \right]_{x=0} \qquad [2.12]$$

The transient experimental technique, used in the current study, blows coolant air through a heated channel. This provides constant values of pressure and temperature during the initial stages of the experiment, which in effect replicates a step change in surface heat flux. If it is assumed that the heat flux to the surface is constant for $t > 0$, then the change in surface temperature can be represented by a parabolic function as illustrated by Figure 2.1.

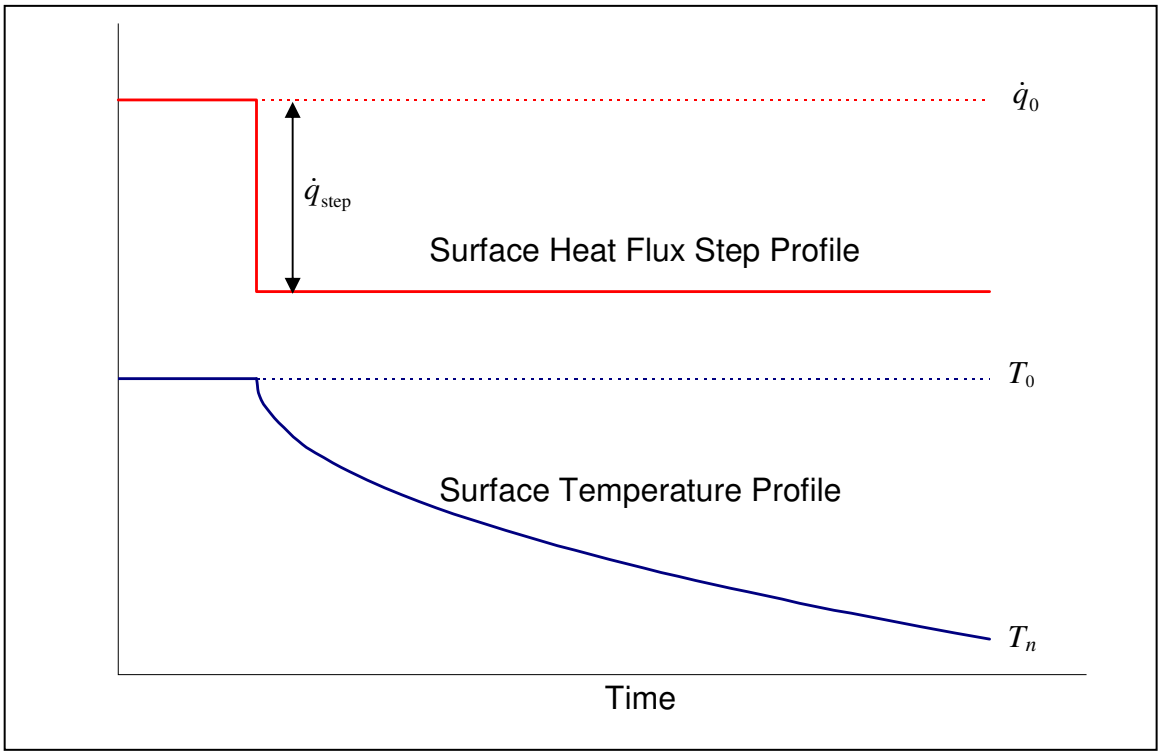

FIGURE 2.1: *Surface heat flux and corresponding change in temperature*

The following boundary conditions are applied in Equation 2.11 to represent a step change in heat flux on the surface of a semi-infinite substrate:

$$\begin{aligned} T_{(x,t=0)} &= T_0 \\ \dot{q}_{(x=0,t)} &= \dot{q}_0 \\ T_{(x=\infty,t=t_\infty)} &= T_0 \end{aligned} \qquad [2.13]$$

This allows Equation 2.11 to be reduced to:

$$T_{(x=0,t)} - T_0 = \frac{2\dot{q}_{(x=0,t)}}{\sqrt{\pi}}\sqrt{\frac{t}{\rho C_p k}} \qquad [2.14]$$

The heat flux and temperature values across the substrate can then be derived analytically with [51]:

$$\frac{\dot{q}_{(x,t)}}{\dot{q}_{(x=0,t)}} = 1 - \frac{2}{\sqrt{\pi}}\int_0^{\eta} e^{-u^2}\,du = erfc(\eta) \qquad [2.15]$$

$$\frac{T_{(x,t)}}{T_{(x=0,t)}} = e^{-\eta^2} - \sqrt{\pi}\,\eta\,erfc(\eta) \qquad [2.16]$$

where $\eta = x(4\alpha t)^{1/2}$ and u is a variable used for integration.

The function $\frac{2}{\sqrt{\pi}}\int_0^{\eta} e^{-u^2}\,du$ is known as the *error function* and is represented by *erf(η)*.

The *complementary error function* equals 1 – *erf(η)* and is represented by *erfc*. The error function can be approximated by:

$$erf(\eta) = 1 - (a_1 t + a_2 t^2 + a_3 t^3)e^{-\eta^2} \qquad [2.17]$$

where [58]:

$$t = (1 + p\eta)^{-1}$$

$$p = 0.47047 \qquad [2.18]$$

$$a_1 = 0.3480242;\ a_2 = -0.0958798;\ a_3 = 0.7478556$$

The analytical solution provides understanding regarding the surface temperature and the internal temperature of a semi-infinite substrate which is exposed to a step change in surface heat flux. It can, however, not be used to determine the surface heat flux from a measured surface temperature profile during a blowdown test. To measure the heat flux during an experimental blowdown, analogue and numerical techniques will be reviewed which will be validated against the analytical solution before being implemented.

2.3 INITIAL MEASUREMENT CONSIDERATIONS

Determining the heat transfer coefficient requires the measurement of three quantities as shown by Equation 2.1:

I. The gas temperature [T_{gas}]

The bulk gas temperature within the experimental channel is determined from a temperature correlation [27]. This requires measuring the centre-point inlet and outlet gas temperatures and the inner surface substrate wall temperature in a region with fully developed flow.

II. The channel wall surface temperature [T_{wall}]

Platinum thin-film gauges are used to measure the wall surface temperature. Consequently, the temperature is measured indirectly by measuring the electrical resistance of the platinum. The change of electrical resistance with the temperature of platinum can be approximated using the following linear relationship:

$$R = R_0 (1 + \alpha_T (T - T_0)) \qquad [2.19]$$

R_0 represents the electrical resistance at the reference temperature T_0, and α_T the temperature coefficient.

III. The heat flux at the wall [$\dot{q}_{wall}$]

When the inner surface of a heated substrate is suddenly exposed to a cooler gas, a step change in surface heat flux takes place. If the inner surface of the substrate is exposed for a short enough time, to prohibit the propagating heat flux from reaching the unexposed outer surface, it can be assumed that the substrate represents a semi-infinite solid [58]. This allows the heat flux out of the substrate to be measured directly with an analogue measuring technique, or to be calculated numerically from the measured inner surface temperature history.

2.4 INITIAL GAUGE CONSIDERATIONS

The thin-film measuring technique was adopted in the current study. When using this technique it is important that the platinum thin-film gauges have a negligible effect on the heat conduction process. The following assumptions and considerations are of importance to ensure that the influence of the gauge remains insignificant:

I. The substrate thickness should emulate a semi-infinite solid

The thickness of the substrate on which the gauge is fired should be deep enough so that the heat transfer into the solid will be comparable to a semi-infinite solid. Therefore, the thermal gradient in the wall should equal zero near the outer unexposed surface of the substrate. This implies that the outer surface temperature of the substrate should be equal to the ambient temperature throughout the experimental measuring period.

A semi-infinite ceramic substrate section will now be considered to illustrate the penetration of flux, be it negative (cooling) or positive (heating). The section, which is at an initial steady-state ambient temperature, will be exposed to a step in constant heat flux on its inner surface. The change in temperature profile through the semi-infinite substrate can be described by Equation 2.20 [58].

$$T - T_0 = \frac{\dot{q}}{k}\left[\left(\frac{4\alpha t}{\pi}\right)^{1/2} e^{-x^2/4\alpha t} - x\, erfc\frac{x}{(4\alpha t)^{1/2}}\right] \qquad [2.20]$$

The temperature distribution into a *Macor* ceramic substrate, suddenly exposed to a constant heat flux, is displayed in Figure 2.2. The profiles display the temperature distribution into the substrate after 0.25, 0.5, 1, and 2 seconds of exposure to a flux of -5 kW/m^2 with an initial temperature of 100 °C. As can be seen, the maximum penetration into the substrate is in the region of 3 mm when the substrate is exposed for a period of 1 second.

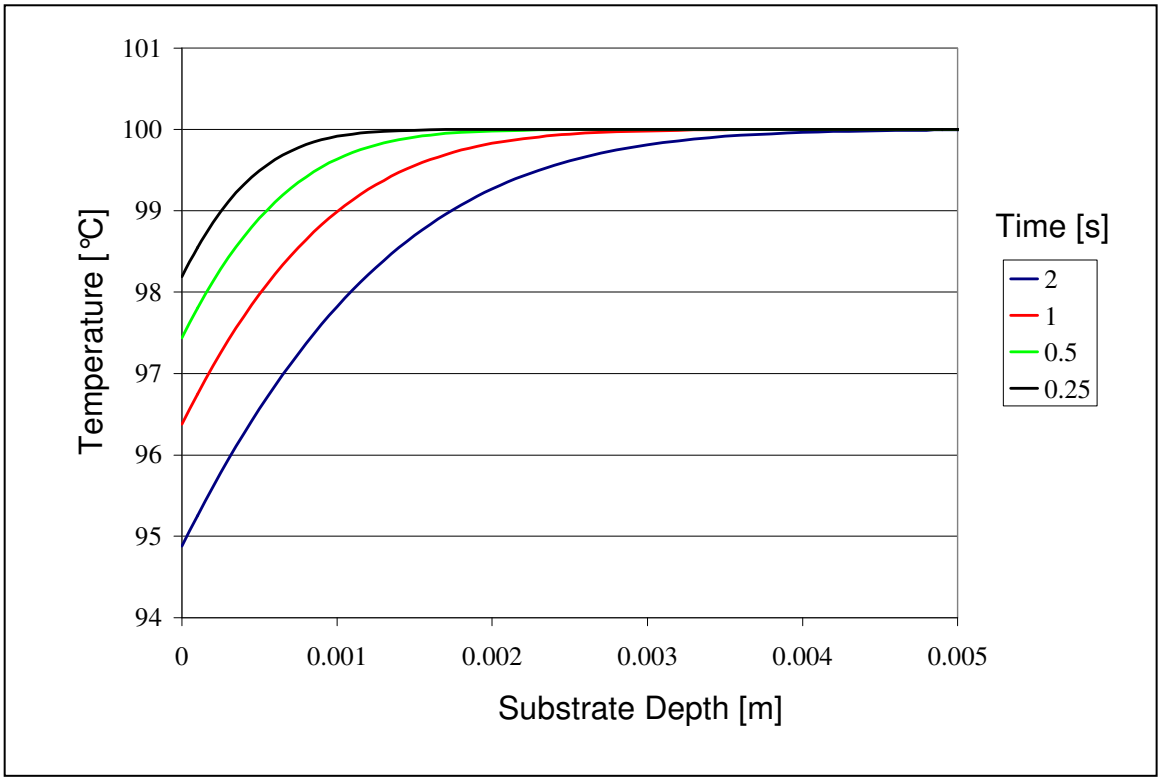

FIGURE 2.2: *Temperature profile within the substrate*

The error in heat flux which is made for a certain substrate thickness, using the semi-infinite substrate assumption, can be determined by using Equation 2.15. Figure 2.3 displays the ratio $\dot{q}_x / \dot{q}_{x=0}$ in relation to η for a time period of 1 second.

From the figure, it can be seen that the error in heat flux, when assuming that the substrate is a semi-infinite substrate, falls below 1% for a η value of 1.85. This is equivalent to a substrate thickness of approximately 3 mm. The thickness of the *Macor* ceramic substrate used in the current study is 12 mm, therefore it can be assumed to represent a semi-infinite solid since the error estimation is less than 1%.

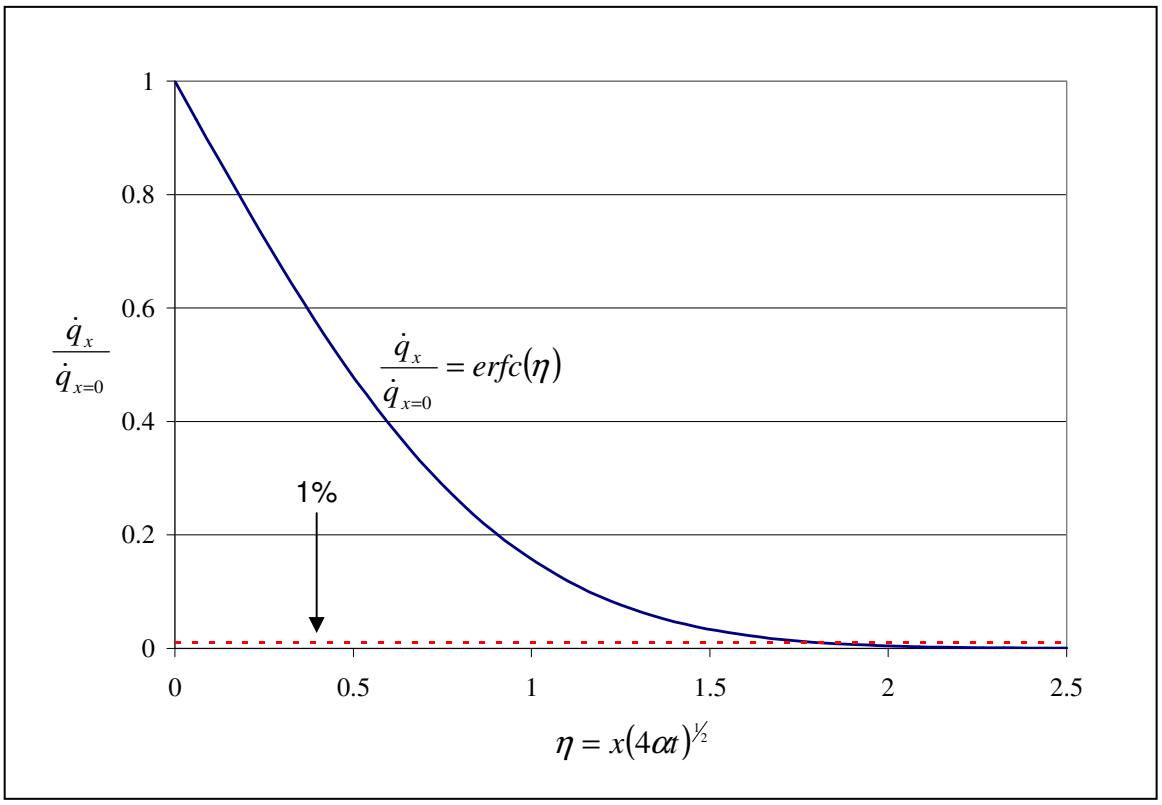

FIGURE 2.3: *Constant heat flux as a function of η*

II. Thermal conductivity of the gauge must be extensively higher than that of the substrate material and its thickness negligible

The thermal conductivity of platinum is approximately 50 times higher than that of the ceramic substrate. Furthermore, the thickness of the thin-film gauge must not influence the surface heat flux into the substrate. Generally, this is the case since the film has an average thickness of approximately 0.1 to 1 μm [51].

Consider Equation 2.21 which describes the ratio between the heat flux through the thin-film and the actual heat flux from the surface [50].

$$\frac{\dot{q}}{\dot{q}_0} = 2a\frac{\sqrt{\alpha_1 t}}{\varepsilon}\left[\frac{1}{\sqrt{\pi}} - \frac{2}{1+a}\sum_{n=0}^{\infty}\left(\frac{1-a}{1+a}\right)^n i\,erfc\left(\frac{n+1/2}{\sqrt{\alpha_1 t}/\varepsilon}\right)\right] \qquad [2.21]$$

Where $i = \sqrt{-1}$ and a is defined as:

$$a = \sqrt{\frac{\rho_1 c_1 k_1}{\rho_2 c_2 k_2}} \qquad [2.22]$$

The footnotes, 1 and 2, represent the thin-film medium and substrate medium. Equation 2.21 is represented graphically in Figure 2.4 and illustrates the varying response time of a platinum thin-film gauge which is exposed to a step change in heat flux. As can be seen, it takes a gauge with a thickness of 1 μm, 0.4 ms to reach 95% of the actual exposed flux which is acceptable for the current application.

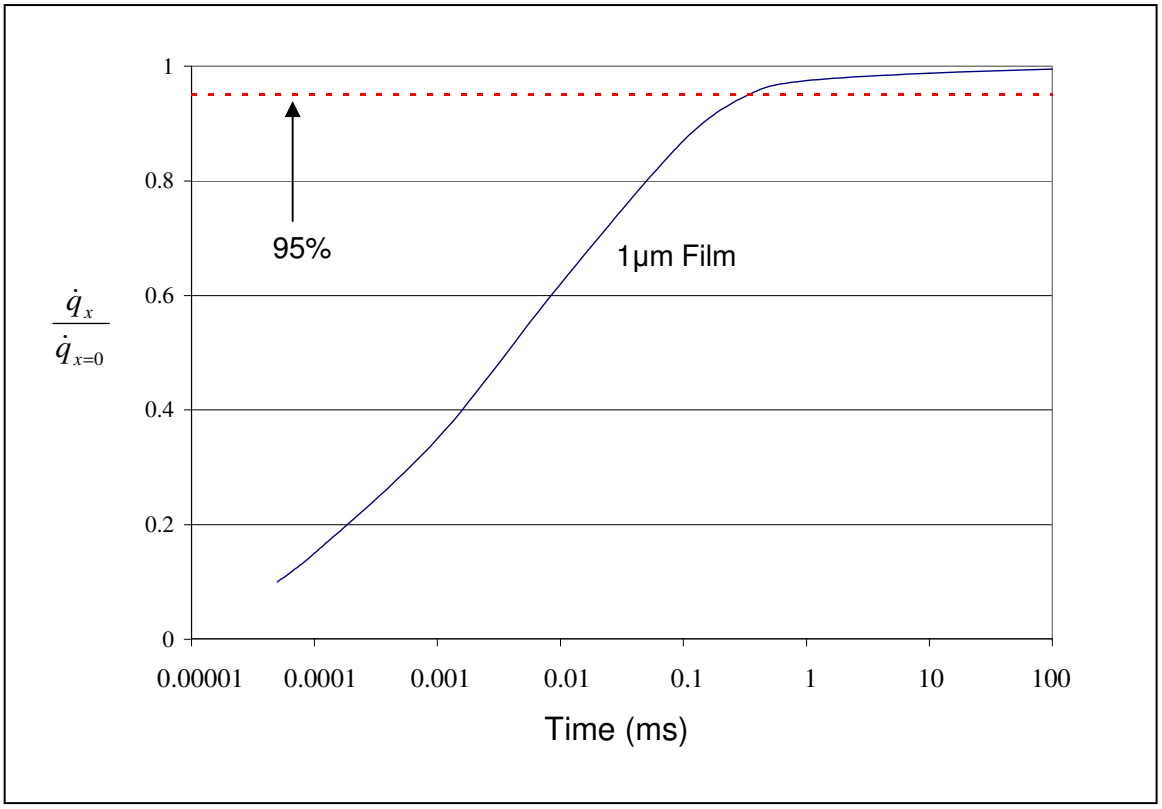

FIGURE 2.4: *Time response of a thin-film platinum gauge*

III. Characteristic time of the gauge must be smaller than that of the actual experiment

The characteristic time of the gauge must be small enough to capture the simulated step change in heat flux imposed on the ceramic wall during an experimental blowdown. The response time of the gauge, which is approximately 0.4 MHz, is comprehensively smaller than the experimental sampling period of 1 to 3 seconds [50]. In similar experimental applications at the Von Karman Institute [52], a data-sampling rate of 10 kHz proved to be adequate to capture the step change in heat flux imposed during the experiment.

IV. The gauge must be situated in an area where the conduction into the substrate is one dimensional

The gauge should not be placed too close to the edge of the substrate to ensure that the heat transfer, being measured by the gauge, is propagating in a one dimensional direction. This implies that the gauge should be placed a distance, from the edge, which is beyond the depth that the heat flux will penetrate during the experimental measuring period.

With these considerations taken into account, it was therefore assumed that the measuring gauges will have a negligible effect on the heat conduction process and need not be taken into account.

2.5 ANALOGUE SIMULATION OF THE HEAT CONDUCTION EQUATION

Two different methods were evaluated to determine the heat flux with thin-film gauges. The first method to be discussed will be referred to as the analogue measuring technique. This method measures surface heat flux directly, from which the corresponding surface temperature can be obtained. The second technique is a numerical approach where the surface temperature history is used to calculate the relating surface heat flux.

The analogue measuring technique had been the favoured heat flux measurement method for the last couple of decades. This is due to the amplification of inherent signal noise during experimental heat flux measurement by numerical techniques and the limited performance of computers. The analogue measuring method makes use of an electronic circuit laid out with a network of resistances and capacitances which reproduces the transfer function described by Equation 2.11 for an applicable range of frequencies [50]. The analogue circuit thus mimics the one-dimensional heat transfer equation into a semi-infinite substrate with a circuit as illustrated in Figure 2.5.

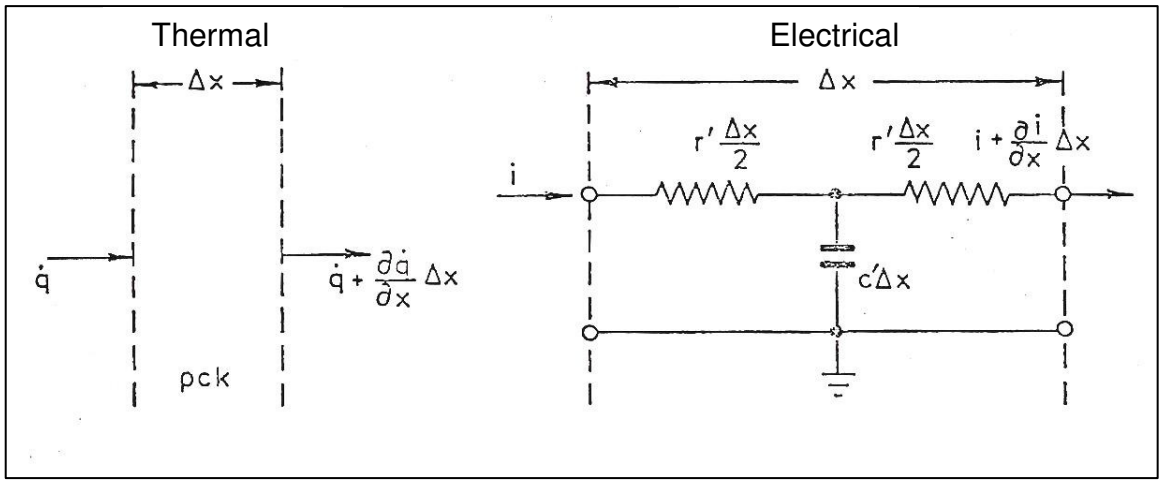

FIGURE 2.5: *Thermal-electrical analogue relation* [50]

In Figure 2.5, the relation between the energy (thermal) and charge (electrical) which is gained and conserved in an element with a thickness Δx is represented by Equation 2.23.

$$\frac{\partial q}{\partial x} = -\rho C_p \frac{\partial T}{\partial t} \quad \Leftrightarrow \quad \frac{\partial i}{\partial x} = -c' \frac{\partial V}{\partial t} \qquad [2.23]$$

The heat transfer in the substrate is analogous to the current and the temperature to the voltage as can be seen from the equivalence between the conduction equation and Ohm's law expressed by:

$$\dot{q} = -k \frac{\partial T}{\partial x} \quad \Leftrightarrow \quad i = -\frac{1}{R'} \frac{\partial V}{\partial x} \qquad [2.24]$$

The diffusion equation can be obtained by combining Equation 2.23 and 2.24. Likewise, the electrical equivalent, i.e. the transmission line equation, can also be obtained:

$$\frac{\partial^2 T}{\partial x^2} = -\frac{\rho C_p}{k} \frac{\partial T}{\partial t} \quad \Leftrightarrow \quad \frac{\partial^2 V}{\partial x^2} = -R' c' \frac{\partial V}{\partial t} \qquad [2.25]$$

where R' and c' represent resistance and capacitance per unit length.

The introduction of a voltage input into the circuit, proportional to the surface temperature, allows a voltage output value which represents the surface heat flux. Further details regarding this technique can be found in Ligrani et al. [50] and Schultz and Jones [51].

The virtual thermal product of the circuit can be determined by applying a voltage change as a square root of time which should provide a constant voltage output. The temperature and flux values in Equation 2.11 can then be replaced by the corresponding voltage input and output values from which it follows that:

$$\sqrt{\rho C_p k_{virtual}} = \frac{2V_{out}}{\sqrt{\pi}} \frac{\sqrt{t}}{V_{in}} \qquad [2.26]$$

The output voltage can then be divided by the virtual thermal product and multiplied by the thermal product of the substrate to obtain the correct value of heat flux.

The use of analogue circuits does not require complex data processing and provides real-time results. The biggest advantage, however, is that by measuring heat flux directly, the substrate temperature history can be recreated by means of an integral approach which inherently reduces the signal noise.

The analogue circuit measuring technique is the preferred method to measure heat flux. This method has been extensively used and its applications have been well documented [50, 51, 60-62]. Unfortunately, the capacitors which are required for the preferred accuracy of circuit operation have not been mass-produced since 1999, either for industrial nor military applications. This greatly increases the manufacturing cost of the analogue circuits, since the once-off manufacturing of these capacitors would be very costly.

Consequently, other methods of heat flux measurement, i.e. numerical schemes, had to be considered.

2.6 NUMERICAL SIMULATION OF THE HEAT CONDUCTION EQUATION

The implementation of a numerical scheme to reproduce the surface heat flux profile from a measured temperature history was initially not the preferred method in the current study. The disadvantage of a numerical scheme is the amplification of electronically induced noise of the experimental surface temperature measurement. This is clearly illustrated in Figure 2.6 which is a comparison between heat flux measured by the analogue approach and heat flux reconstructed by the numerical approach.

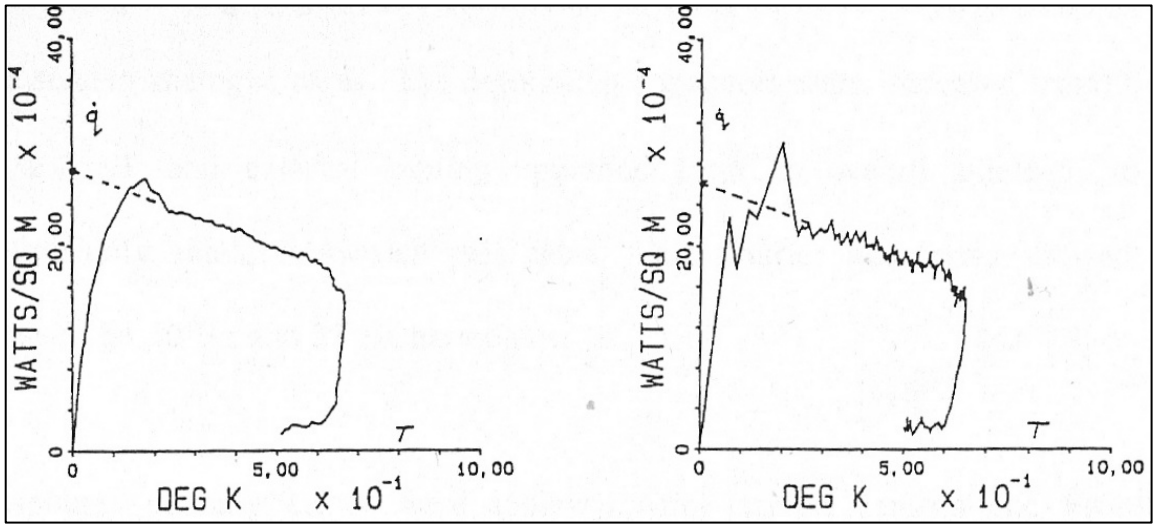

FIGURE 2.6: *Comparison between heat flux measured directly (left-hand side) and heat flux numerically reconstructed (right-hand side)* [60]

Unfortunately, due to the reasons discussed in the previous section, the analogue measuring approach was not a viable option. It was, therefore, decided to make use of a numerical technique and the following approaches were evaluated:

I. <u>The Cook-Felderman algorithm</u>

The most obvious or simplest solution would be to implement an analytical approximation, thus integrating Equation 2.11 to reproduce a heat flux profile from a temperature contour. The numerical integration of this particular equation was proposed by Cook and Felderman [63] and is shown in Equation 2.27.

$$\dot{q}_{(x=0,t_n)} = \sqrt{\frac{\rho C_p k}{\pi}} \left[\frac{T_{(t_n)}}{\sqrt{t_n}} + \sum_{i=1}^{n-1} \left(\begin{array}{l} \dfrac{T_{(t_n)} - T_{(t_i)}}{(t_n - t_i)^{1/2}} - \dfrac{T_{(t_n)} - T_{(t_{i-1})}}{(t_n - t_{i-1})^{1/2}} \\ + 2\dfrac{T_{(t_i)} - T_{(t_{i-1})}}{(t_n - t_i)^{1/2} + (t_n - t_{i-1})^{1/2}} \\ + \dfrac{T_{(t_n)} - T_{(t_{n-1})}}{(t_n - t_{n-1})^{1/2}} \end{array} \right) \right]_{x=0} \qquad [2.27]$$

The most notable disadvantage of this method, other than noise amplification, is that the Cook-Felderman algorithm is computationally expensive. To determine the solution at the n^{th} point, requires the summation of n-1 points. Thus for increased accuracy a smaller temporal discretization will result in an exponential increase in solution time.

II. Fourier transform

An attractive alternative to the Cook-Felderman algorithm is to make use of a Fourier transform to convert surface temperature history into a flux history. By performing a Fast Fourier Transform (FFT) on the temperature time function T(t), an equivalent temperature representative series in the frequency domain is obtained (T(ω)) [57]. A complex product is then performed on the temperature frequency function using a complex transfer function H($j\omega$) which provides the flux solution in the domain $\dot{q}(j\omega)$. An inverse FFT is performed on the complex domain flux solution to obtain a time-representative flux profile.

The main disadvantage concerning the application of an FFT is that the Fourier domain only deals with periodic signals. This implies that the input signal is considered to be periodic by the transformation, entailing that the time series from t_0 to t_n is regarded as an infinite time series of period t.

Denos et al. [52] suggested that this phenomenon can be avoided by adding a zero-padding extension to the end of the input signal. When employing this in the case of a non-periodic signal, it tends to become computationally expensive since the computational effort to compute the suggested zero-padding extension nullifies the speed advantage of this algorithm.

III. Crank-Nicholson scheme

An alternative to the previously discussed methods is to make use of a numerical solution to obtain the internal substrate temperature distribution. By using the initial ambient substrate temperature and the measured inner surface temperature history as boundary conditions, the temperature profile within the substrate can be calculated by making use of the Crank-Nicholson method. The heat flux at the wall can then be derived from the derivative of the numerically obtained wall substrate temperature profile.

It has been shown by Denos et al. [52] that the Crank-Nicholson numerical scheme can be used as a viable alternative to the analogue approach if over-sampling and low pass filtering is used. The Crank-Nicholson scheme promises the most flexibility and also to be the most computationally inexpensive method in comparison with the other numerical methods which were reviewed. It was therefore decided to make use of this method in the current study.

2.7 IMPLEMENTATION OF THE CRANK-NICHOLSON SCHEME

The Crank-Nicholson method is an implicit finite difference algorithm which was developed to solve parabolic partial differential equations. The current study makes use of this scheme to solve Equation 2.7, the one-dimensional heat conduction/diffusion equation, to calculate the thermal gradients within a heated ceramic substrate when its inner surface is suddenly exposed to cooler air.

Equation 2.28 characterises Equation 2.7 with the particular function variables notated and all the terms moved to the left-hand side.

$$\frac{\partial T}{\partial t}(x_i, t_j) - \alpha \frac{\partial^2 T}{\partial x^2}(x_i, t_j) = 0 \qquad [2.28]$$

Let x_i and t_j describe a reference grid point, with i and j representing the particular spatial and temporal node arrangement. A forward difference approximation for the heat conduction/diffusion equation can be obtained by applying a Taylor series expansion in t to form the difference quotient:

$$\frac{\partial T}{\partial t}(x_i, t_j) = \frac{T(x_i, t_j + k) - T(x_i, t_j)}{k} - \frac{k}{2}\frac{\partial^2 T}{\partial t^2}(x_i, \mu_j) \qquad [2.29]$$

where $\mu_j \in (t_j, t_{j+1})$ and k represent a time-step increment.

Likewise a forward difference can be obtained by a Taylor series expansion in x forming the difference quotient:

$$\frac{\partial^2 T}{\partial x^2}(x_i, t_j) = \frac{T(x_i + h, t_j) - 2T(x_i, t_j) + T(x_i - h, t_j)}{h^2} - \frac{h^2}{12}\frac{\partial^4 T}{\partial x^4}(\xi_i, t_j) \qquad [2.30]$$

where $\xi_i \in (x_{i-1}, x_{i+1})$ and h represents a spatial-step increment.

Inserting the corresponding difference quotients (Equation 2.29 and Equation 2.30) into Equation 2.28 provides:

$$\frac{T_i^{j+1} - T_i^j}{k} - \alpha \frac{T_{i+1}^j - 2T_i^j + T_{i-1}^j}{h^2} = 0 \qquad [2.31]$$

where T_i^j denotes $T(x_i, t_j)$ with its local truncation error being:

$$\tau_{ij} = \frac{k}{2}\frac{\partial^2 T}{\partial t^2}(x_i, \mu_j) - \alpha\frac{h^2}{12}\frac{\partial^4 T}{\partial x^4}(\xi_i, t_j) \qquad [2.32]$$

This provides a forward difference approximation of the heat conduction/diffusion equation as illustrated in Figure 2.7. This approximation is of order $O(k+h^2)$ and is conditionally stable, which implies that a solution may not necessarily be obtained.

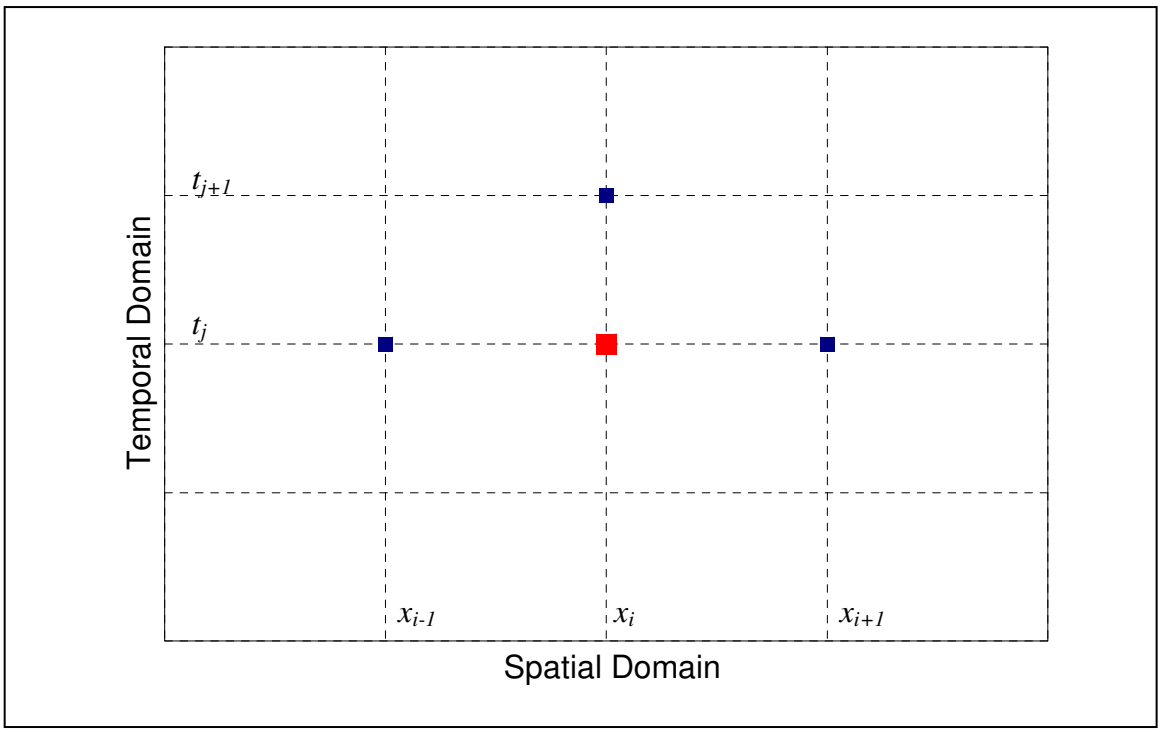

FIGURE 2.7: *Forward difference discretization*

An implicit backward difference quotient for $\partial T/\partial t(x_i, t_j)$ will now be considered to obtain an unconditionally stable approximation of Equation 2.28. The backward difference approximation is obtained by implementing the previously discussed Taylor expansion around t as illustrated in Figure 2.8 and described by Equation 2.33:

$$\frac{\partial T}{\partial t}(x_i, t_j) = \frac{T(x_i, t_j) - T(x_i, t_j - k)}{k} - \frac{k}{2}\frac{\partial^2 T}{\partial t^2}(x_i, \mu_j) \qquad [2.33]$$

where $\mu_j \in (t_{j-1}, t_j)$.

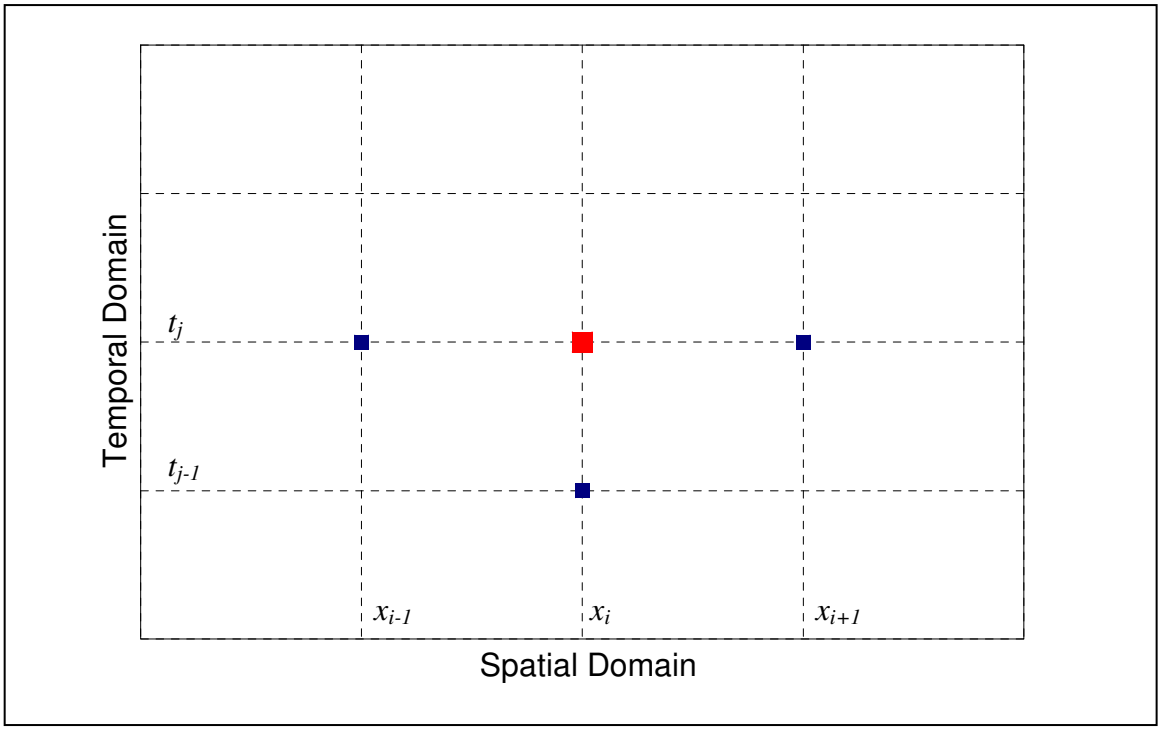

FIGURE 2.8: *Backward difference discretization*

Substituting this approximation combined with Equation 2.30 into Equation 2.28 provides Equation 2.34:

$$\frac{T_i^{\,j} - T_i^{\,j-1}}{k} - \alpha \frac{T_{i+1}^{\,j} - 2T_i^{\,j} + T_{i-1}^{\,j}}{h^2} = 0 \qquad [2.34]$$

An implicit backward difference approximation for the heat conduction/diffusion equation with a local truncation error being:

$$\tau_{ij} = -\frac{k}{2}\frac{\partial^2 T}{\partial t^2}(x_i, \mu_j) - \alpha \frac{h^2}{12}\frac{\partial^4 T}{\partial x^4}(\xi_i, t_j) \qquad [2.35]$$

The backward difference approximation is an unconditionally stable solution, however, its truncation error is still of the order $O(k+h^2)$.

An averaging of the forward difference approximation at the j^{th} step in t (Equation 2.31) and the backward difference approximation at step j+1 in t (Equation 2.34 at a forward time step) is done to obtain a solution which provides an approximation of order $O(k^2+h^2)$ and is unconditionally stable. The averaged algorithm is shown in Equation 3.36 and is known as the Crank-Nicholson scheme [64, 65].

$$\frac{T_i^{j+1}-T_i^{j}}{k}-\frac{\alpha}{2}\left(\frac{T_{i+1}^{j}-2T_i^{j}+T_{i-1}^{j}}{h^2}+\frac{T_{i+1}^{j+1}-2T_i^{j+1}+T_{i-1}^{j+1}}{h^2}\right)=0 \qquad [2.36]$$

Assuming that the second-order derivatives represented by the truncation errors (Equation 2.32 and 2.35) approach equality, it implies:

$$\frac{\partial^2 T}{\partial t^2}(x_i,\mu_{j+1})\approx\frac{\partial^2 T}{\partial t^2}(x_i,\mu_j) \qquad [2.37]$$

Rewriting the temporal and spatial increments, k and h, as Δt and Δx in Equation 2.36 and introducing the weighting factor η gives Equation 2.38:

$$\frac{T_i^{j+1}-T_i^{j}}{\Delta t}=\frac{\alpha}{2}\left(\frac{\eta\left(T_{i+1}^{j}-2T_i^{j}+T_{i-1}^{j}\right)+(1-\eta)\left(T_{i+1}^{j+1}-2T_i^{j+1}+T_{i-1}^{j+1}\right)}{\Delta x^2}\right) \qquad [2.38]$$

The weighting factor, η, provides the ability of reducing this scheme to either an explicit scheme (η = 0, conditionally stable), the classic Crank-Nicholson scheme which is implicit (η = 0.5) or a fully implicit scheme (η = 1). The influence of the different weighting factor values is shown in Figure 2.9 for a temporal interpreted solution obtained from node T_i^{j}.

From Figure 2.9, it can be seen that the explicit approximation assumes that the value T_i^{j} prevails throughout the entire time step, except at time t+Δt. The opposite is noted for the fully implicit approximation which postulates that the value of T suddenly drops from T_i^{j} to T_i^{j+1} and stays at a value T_i^{j+1} for the rest of the time step. Initially, it may seem that

the Crank-Nicholson approximation which assumes a linear transition in value T between time step T_i^j and T_i^{j+1} is the preferred solution. It has, however, been shown that for a large enough time step this is not necessarily true [66].

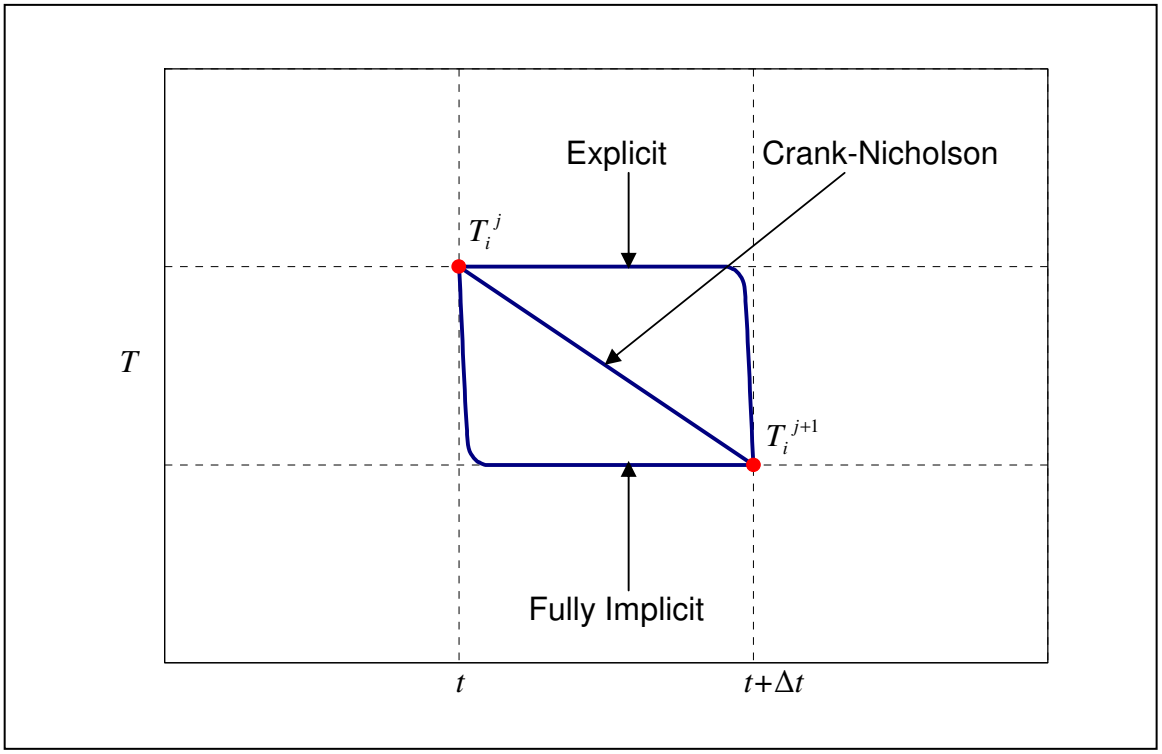

FIGURE 2.9: *Variation of temperature with time for three different schemes*

This statement implies that although the Crank-Nicholson scheme is usually described as unconditionally stable, oscillatory solutions which are not physically realistic may be obtained if the time step is too large. The Crank-Nicholson scheme is, however, more accurate than the fully implicit variation at smaller time steps. Therefore initially, processed data were compared with the profiles of solutions obtained by implementing the fully implicit scheme to ensure negligibility of the time-step size.

When implementing this scheme, the unknown temperatures at time j+1 in Equation 2.38 are expressed as a function of the computed solution, at time j. This provides a tri-diagonal matrix which is solved with Crout factorisation [64]. This scheme was implemented in a computer program (Appendix A) and validated against an analytical

case with constant heat flux. The substrate discretization depth was 7mm and discretized using 5 000 node points, clustered towards the surface where the higher gradients are expected. Figure 2.10 shows excellent agreement between the numerically predicted temperature profiles in the substrate and the analytical values at different time increments.

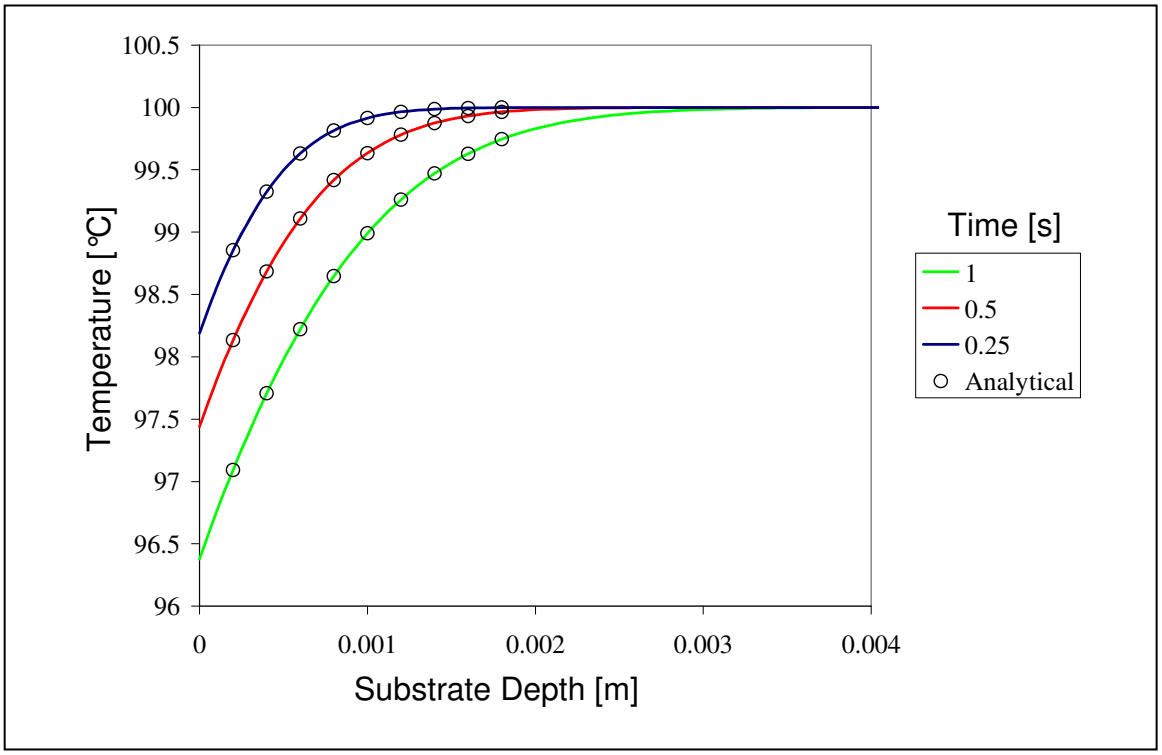

FIGURE 2.10: *Numerical temperature profile approximation within the substrate*

2.8 CONCLUSION

The current chapter considered the governing equations of unsteady one dimensional heat conduction in detail. Initial measurement and gauge considerations were discussed along with a comparison between the analogue and numerical measurement techniques. The chapter was concluded with a detailed discussion regarding the implementation of the Crank-Nicholson numerical scheme.

CHAPTER 3
EXPERIMENTAL METHOD

3.1 PREAMBLE

As previously stated, the primary objective of the current study is the measurement of heat transfer enhancement near the entrance of a film cooling hole in a turbine blade cooling passage. A transient experimental measurement technique is used, which makes use of platinum thin-film gauges, to measure the substrate surface temperature history during an experimental blowdown. A numerical scheme is then implemented to obtain the corresponding surface heat flux from the measured surface temperature.

Surface temperature measurements are made downstream and upstream of the coolant extraction hole as illustrated in Figure 3.1. The measurement area downstream of the coolant extraction hole is concentrated near the entrance of the hole to provide line-averaged measurements of the surface heat transfer enhancement induced by the extraction of coolant. An upstream measurement is made to obtain a reference surface temperature measurement in an unenhanced region, i.e. the region where the surface heat transfer is not directly influenced by the extraction of coolant. The purpose of this reference measurement point is to provide a dimensionless representation of the near-hole heat transfer enhancement as defined in the enhancement factor.

The enhancement factor is obtained by dividing the heat transfer value in the enhanced region, downstream of the extraction hole surface, by the heat transfer value of the region upstream of the coolant hole. This unenhanced surface area is situated approximately ten

bleed-hole diameters upstream of the suction hole, in a section with fully developed flow and thermal boundary layer characteristics.

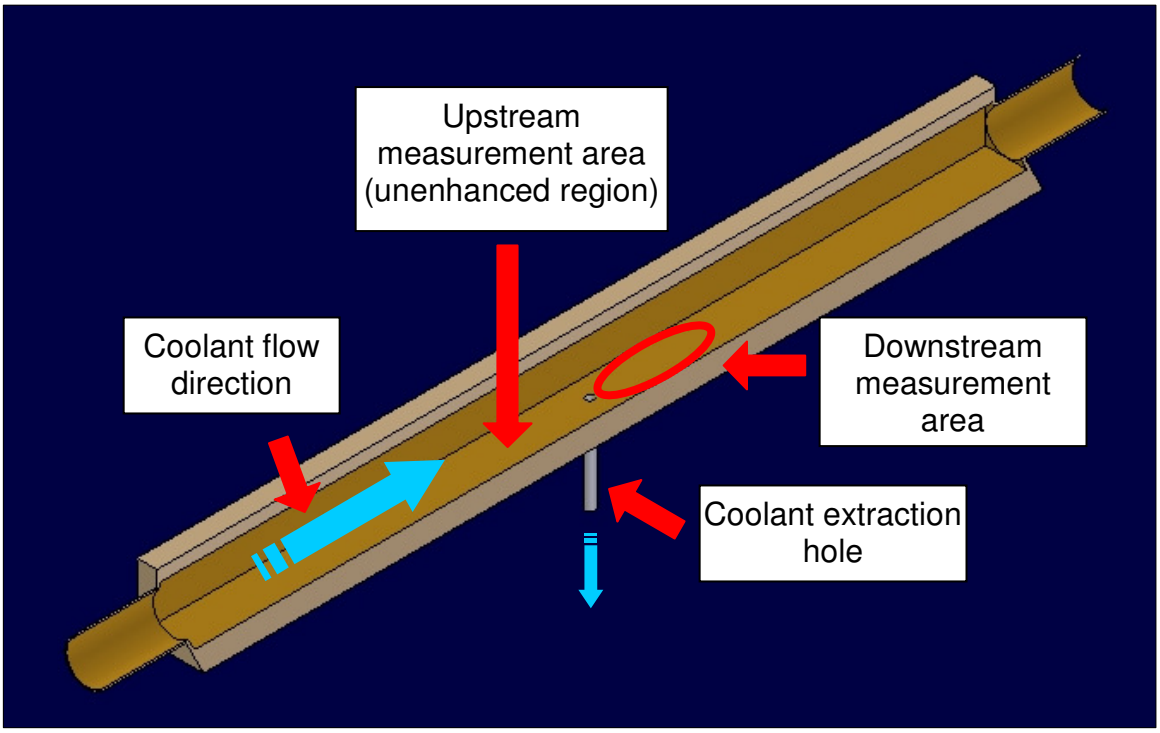

FIGURE 3.1: *Schematic cut-away of the experimental channel*

3.2 THE EXPERIMENTAL CHANNEL

The test channel, displayed in Figure 3.2, is representative of a square turbine blade cooling channel, with internal dimensions of 25 mm × 25 mm. The walls are made from *Erthalyte* (nylon compound) and *Macor* (ceramic) plates, which are sealed and clamped together within an aluminium casing. The *Macor* and *Erthalyte* materials were chosen because of their low thermal conductivity, i.e. good insulation properties. Adequate insulation properties are required if the heat transfer to the gauges is to be one-dimensional and representative of a semi-infinite substrate. Additionally, the advantage of the *Macor* ceramic is that it can be heated to a 1 000ºC without any significant geometric deformations. This makes it an ideal substrate for the platinum gauges to be fired on, since temperatures close to this value will be required during the manufacturing of the gauges.

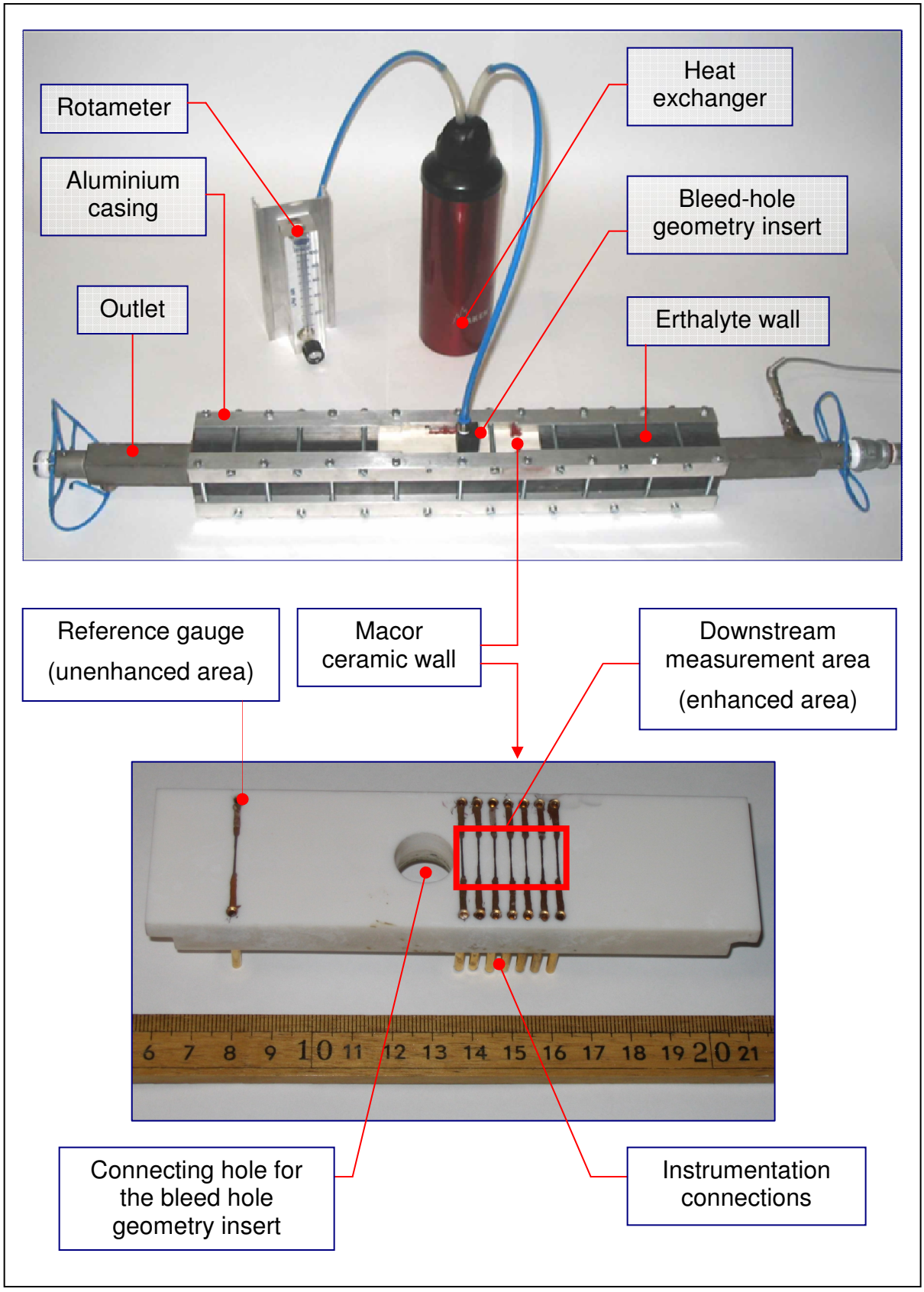

FIGURE 3.2: *Experimental channel section and inner ceramic wall surface*

A close-up view of the *Macor* ceramic section is displayed in Figure 3.2. This ceramic section provides the substrate on which the platinum thin-film gauges are fired and also serves as housing for the instrumentation connections and the bleed hole geometry plug connection. From this figure, the concentrated gauge positioning downstream of the insertion hole should be noted. Seven gauges are placed in this area to capture the line-averaged surface heat transfer augmentation downstream of the coolant extraction hole. The isolated gauge on the left-hand side is situated in the unenhanced heat transfer region and is used for the reference surface temperature measurement, as previously noted.

The bleed hole geometry insert is manufactured from *Erthalyte* and is shown in Figure 3.3. Interchangeable bleed hole geometry inserts are manufactured for the various bleed hole extraction angles. The geometry is inserted into the ceramic section, fitting flush with the substrate inner wall surface, and then sealed. When the test channel is heated, the ceramic substrate expands, compressing the tight-fitting *Erthalyte* geometry, resulting in a shrink fit. As a result, the geometry insert, slightly deformed due to compression, is replaced after each set of tests.

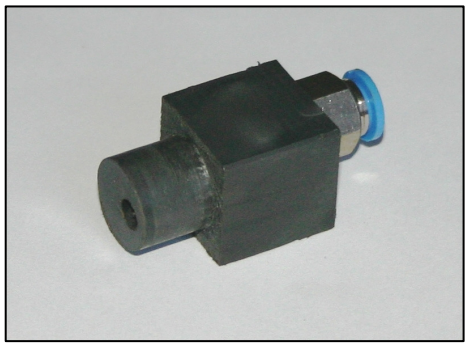

FIGURE 3.3: *Bleed-hole insert*

The furnace displayed in Figure 3.4, was initially used during the manufacturing of the platinum thin-film gauges and subsequently modified to house the experimental channel section. The furnace offers a thermally controlled environment, providing the capability to control the wall temperature of the test channel.

Coolant flow is provided by a compressor, delivering air at a maximum pressure of 600 kPa and a mass flow rate of 2 kg/s. The feed from the compressor is controlled via a solenoid valve placed upstream of the channel section. The solenoid valve is a high-speed open/shut valve which provides a step change in flow when desired. Pressure regulators are fitted at the inlet and outlet of the main channel to ensure a steady pressure during blowdown. Furthermore, the regulators provide the ability to adjust the mass flow rate and pressure inside the channel to the required level.

FIGURE 3.4: *Furnace used to control the experimental channel wall temperature*

An orifice plate (manufactured according to BS 1042) is situated downstream of the experimental channel and is used to determine the mass flow rate in the main channel. The amount of coolant extracted from the bleed hole is controlled and determined by a rotameter, which is situated on the extraction channel outlet. The extracted air flows through a heat exchanger, cooling the bleed air down to the prescribed temperature for which the rotameter is calibrated. Pressure measuring points and PT100 sensors are placed at the inlet and outlet of the main channel to measure the channel pressure drop and centre-point temperature. The PT100 sensors are BS1904 class A type and coupled in

a 4-wire circuit configuration to prevent any lead-resistance errors. Figure 3.5 provides a schematic illustration of the experimental setup.

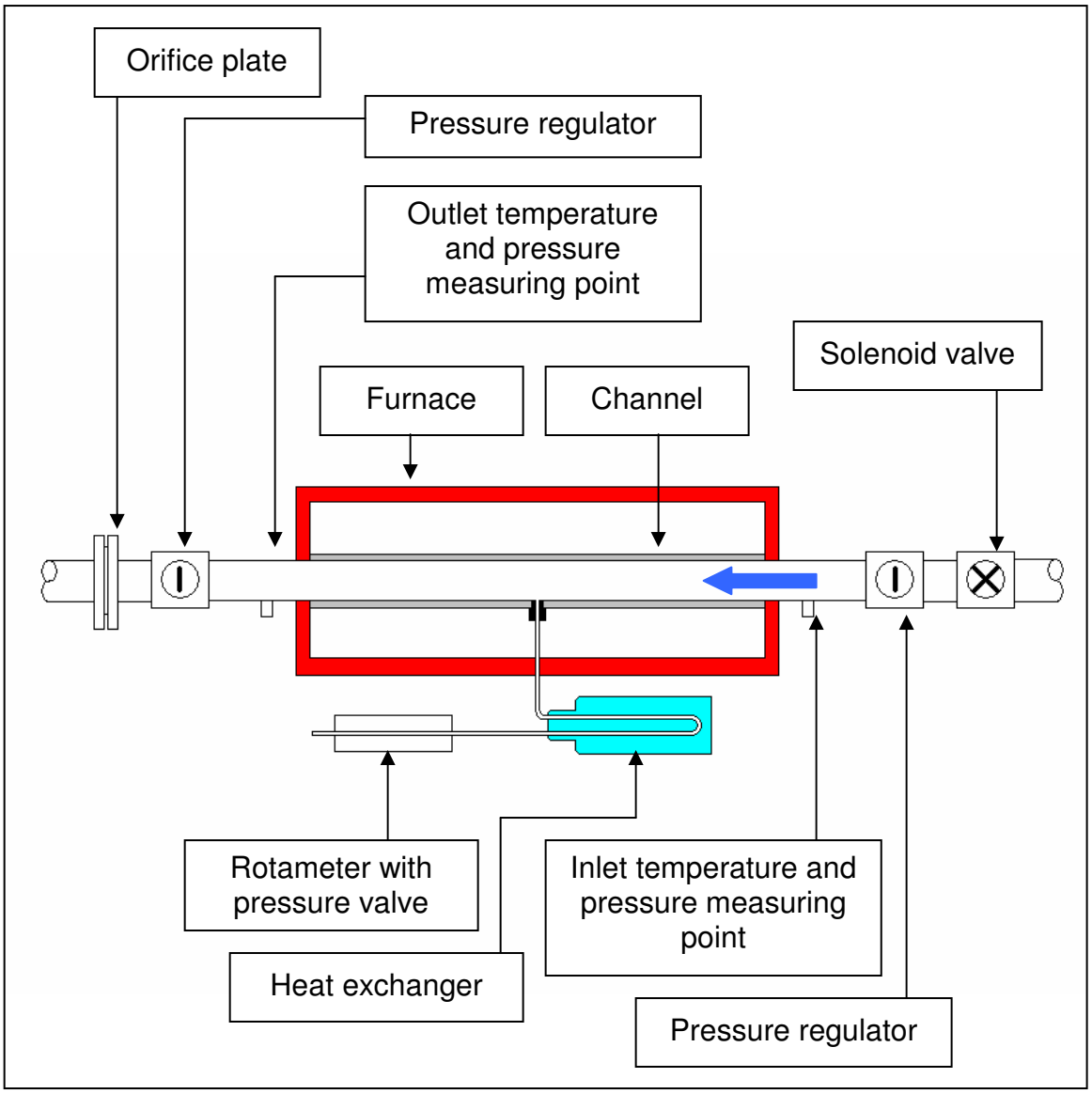

FIGURE 3.5: *Schematic layout of the experimental setup*

3.3 GAUGE CONSTRUCTION AND CALIBRATION

The manufacturing of the thin-film gauges was done according to specifications set up by Ligrani et al. [50].

The *Macor* ceramic surface was smoothed and thoroughly polished as preparation for the application of the platinum gauges. Any inconsistency or discontinuity on the substrate surface may influence the quality of the final gauge. In order to smooth the chosen surface for polishing, silicon carbide sandpaper with #600, #800 and #1200 grain were used for initial polishing. The surface was polished on a rotating wheel for a period of 4-7 minutes with each grain of paper. For the final stage of polishing, the manufacturing specification suggested using an abrasive known as cerium oxide powder (also referred to as ceria); initially combined with small amounts of metal polish and then later mixed with kerosene during the polishing process.

Cerium oxide was previously widely used in the ceramic and glass polishing industry, but is not imported into South Africa anymore. As an alternative abrasive, silica suspension was used. Initial trials showed that the silica suspension provided a better-quality surface finish when compared with earlier ceramic sections which were polished with cerium oxide.

Figure 3.6 shows the *Macor* section being polished on a polishing wheel. The black disc is a polishing cloth soaked with suspended silica solution. The surface is polished for a period of 10 minutes, cleaned with a liquid detergent and then inspected under a microscope for any discontinuities on the substrate surface. Once a proper surface finish has been obtained, the *Macor* section is placed in an oven at a temperature of 100 ºC to remove any remaining moisture.

FIGURE 3.6: *Final polishing stage of the substrate surface (Insert: Silica suspension)*

Once the surface has been properly cleaned and any surface moisture has been removed, the application of the platinum begins. During the current study it was found that liquid platinum solutions from different manufacturers may provide different thermal resistance curve gradients. The author believes that this occurrence may be attributed to tainted liquid platinum solutions or certain platinum suspensions which do not completely evaporate during the firing process. For this reason, identical platinum, gold and essence solutions were obtained from the same manufacturer as prescribed by Ligrani et al. [50]:

I. *Liquid Bright Platinum 05-X*.

II. *Liquid Bright Gold FL-8*.

III. *Thinning Essence # 4* (This thinning solution was suggested by *Engelhard Industries* to serve as a replacement for the *VKI*-prescribed *Thinning Essence 730, w*hich is not manufactured under this reference anymore. It proved to be an adequate substitution).

Figure 3.7 illustrates the paint and some of the utensils which were used during the painting of the gauges.

FIGURE 3.7: *Platinum, gold and thinning essence solutions along with stylus, brushes and other utensils used during gauge application*

Initial trails were done with various platinum and essence mixtures as well as various stylus tips to obtain the correct mixture and application technique. A mixture of 100% platinum solution may be used although the addition of thinning essence allows for an easier application. Conversely, too much thinning agent in the compound will result in non-uniform film gauge boundaries. A sufficient compound consisting of 80% platinum solution and 20% thinning agent was found to be adequate. Mixing was also done in a clean environment, since any impurities either from the containers or mixing bowl may contribute to a defective gauge.

Once a layer of the platinum compound has been applied to the ceramic substrate surface, it was placed under a high-power lamp to dry. Again care was taken to avoid the collection of dust or any impurities on the drying platinum layer. This is illustrated in Figure 3.8.

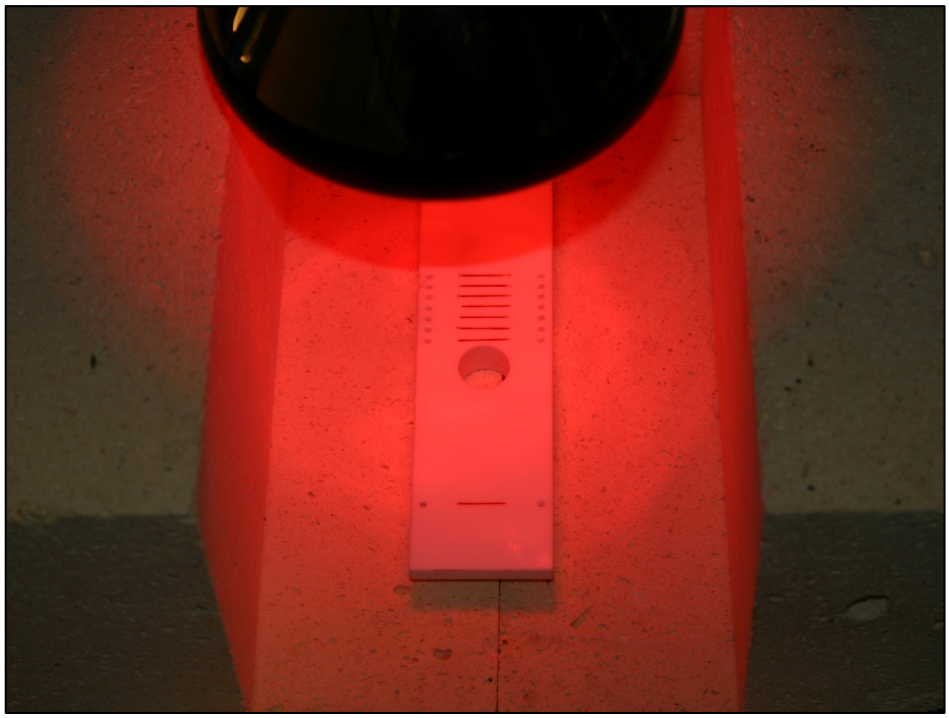

FIGURE 3.8: *Platinum layers on substrate surface drying under a high-power lamp*

After the platinum gauges have dried, it was baked in an electrical furnace. Prior to inserting the gauges, the furnace was purged of foreign gases and other impurities by heating it to a 1 000 ºC. Once it cooled down overnight, the baking process was started. This is a temperature-controlled heating process, by which the ceramic is inserted into the furnace when it reaches a 100 ºC. The temperature of the oven is then increased to 250 ºC, with its door open to allow ventilation. The ventilation period lasts about 10 to 15 minutes and allows moisture and any thinning essence to evaporate from the oven. Once this period is over, the furnace door is closed and its temperature is increased to 670 ºC-690 ºC where the ceramic is left to bake for approximately an hour.

When the baking cycle is complete, the gauge resistances are checked and the painting and baking cycle is repeated if the resistance is too high. Once all the platinum gauges were at the desired resistance, the thin-film gold leads were painted on, following the same baking cycle as with the platinum application.

Instrumentation connections to the thin-film gold leads were made from gold-plated "banana" plugs. These plugs are inserted into specially drilled holes in the ceramic substrate and can be seen protruding from the back of the ceramic in Figure 3.2. Prior to the insertion of these plugs, the holes are filled with a silver-loaded epoxy to aid with the conductivity between the gold thin-film on the hole surface and the plug. Once the epoxy has set, the plug provides a simple connection point for the thin-film gauge instrumentation.

Calibration of the finished gauges was done with the calibration bath displayed in Figure 3.9. Silicon calibration oil was used as bath liquid and resistance measurements were done with an 8.5 digit HP3485A multi-meter. To ensure accuracy, Kelvin cables were used to make a 4-wire connection between the gauge and multi-meter.

FIGURE 3.9: *Calibration bath*

3.4 DATA ACQUISITIONING

The data-acquisitioning system can be divided into two segments. The first segment or front-end is the Resistance Temperature Device (RTD) interface, displayed in Figure 3.10, which connects the platinum gauges with the data-acquisitioning system. The front-end card is an 8-channel 4-wire high bandwidth RTD interface, designed specifically for the current study. The purpose of this card is to provide a filtering and amplification aptitude for the gauge signal. It also provides an adjustable constant current source, selectable gain and the option of AC or DC coupling at the output.

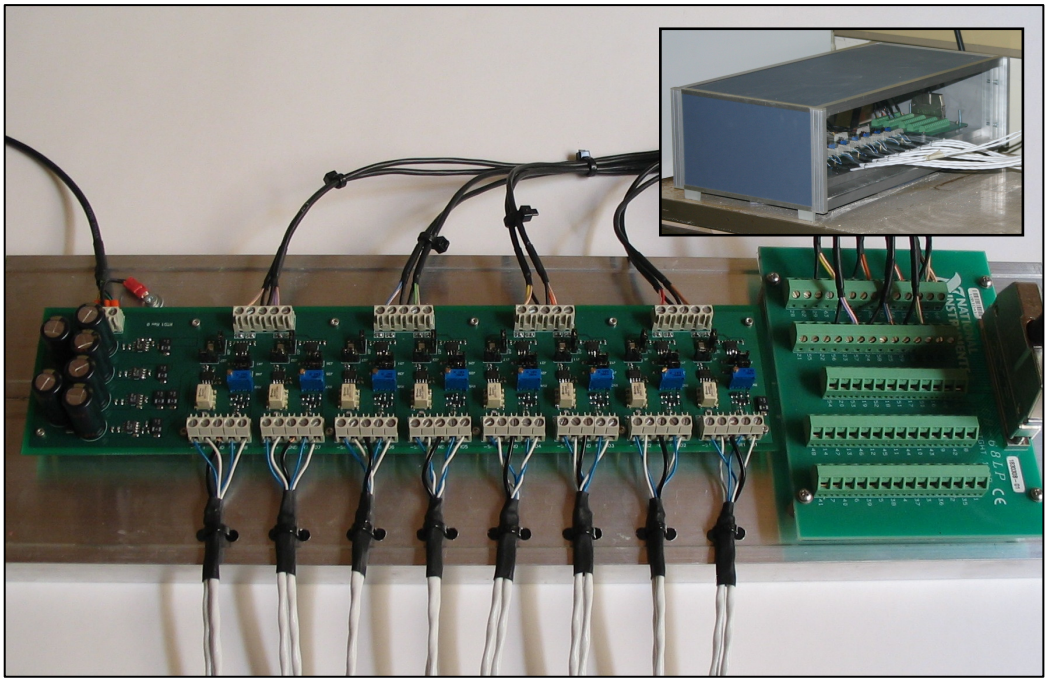

FIGURE 3.10: *RTD interface card (Insert: RTD interface card housing)*

Figure 3.11 shows a schematic function description of the RTD interface (the electronic layout of the RTD interface can be found in Appendix B).

The second segment or back-end is the data-acquisitioning card. For the current study, the NI 6250 D/A card was used which provided the capability of sampling at 250 kHz per channel, for an 8-channel application (4-wire coupling).

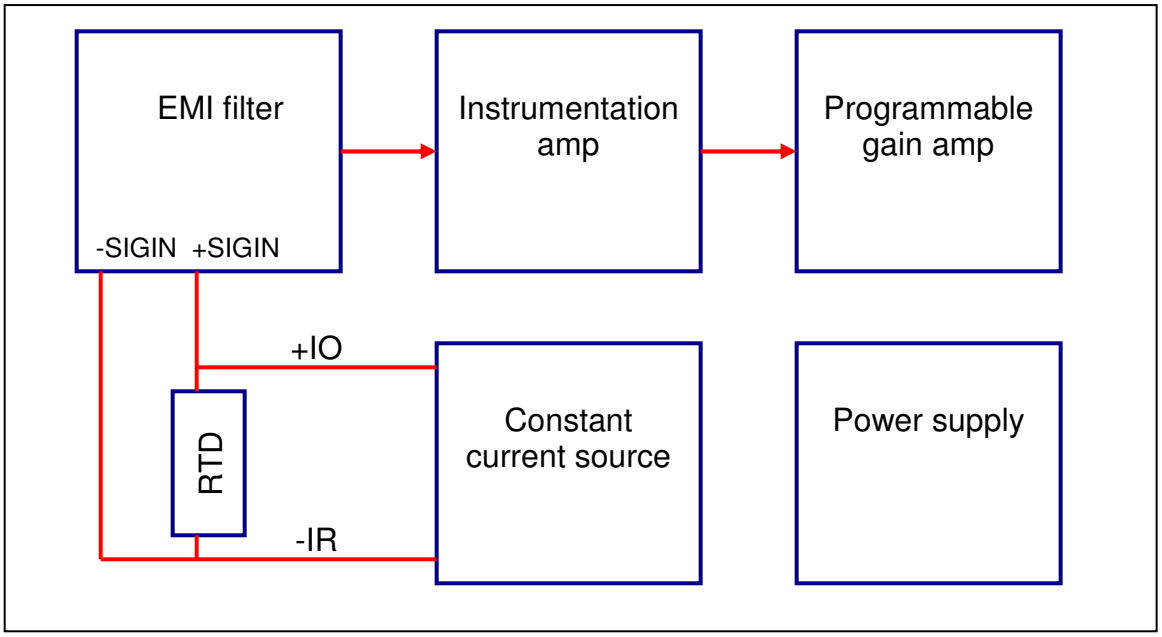

FIGURE 3.11: *RTD interface: Schematical layout*

3.5 ISSUES REGARDING DATA REDUCTION

The following aspects do not relate directly with the experimental measurement process, but should be highlighted to provide further insight. This includes a discussion of the channel velocity and temperature profile, bulk temperature estimation, radiation effects and material properties.

I. Velocity and temperature profile

The upstream and downstream surface temperature measurement area within the experimental channel is situated in a region beyond 10 channel diameters from the inlet and outlet of the channel section. This is done to ensure that the measurement area is situated in a region with fully developed hydrodynamics and thermal boundary layer and that any effects induced by the main channel outlet would not propagate upstream.

Centre-line velocity measurements were done in the region where the reference surface temperature measurement is taken to ensure that the flow field in this area is unaffected by the extraction of coolant further downstream. The measured velocity profile is then compared with a flow profile obtained by the $1/7^{th}$ power law [67]. The $1/7^{th}$ power law profile is characteristic of fully developed, turbulent channel flow and a comparison with the measured velocity profile at maximum coolant extraction (suction ratio = 5) is displayed in Figure 3.12. As can be seen, the velocity profile in the unenhanced region resembles a fully developed profile and is unaffected by the coolant extraction.

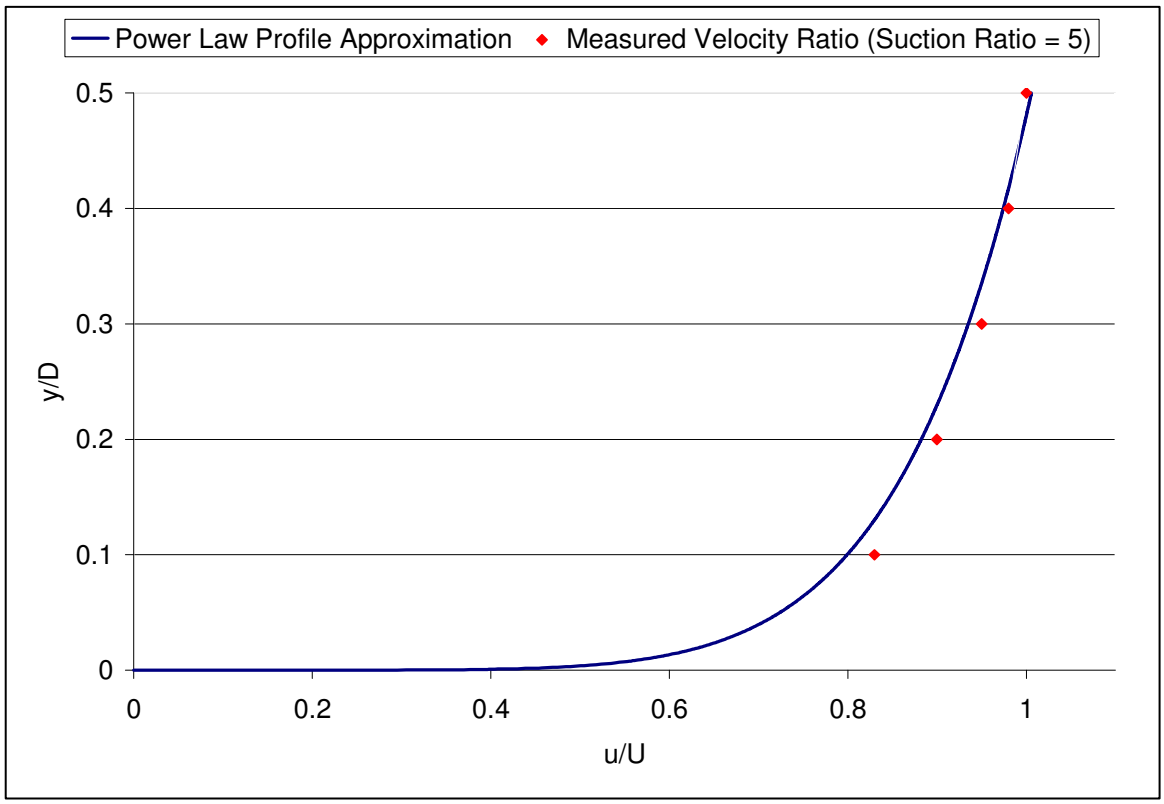

FIGURE 3.12: *Velocity profile in the unenhanced region*

II. Bulk fluid temperature (or mixed mean fluid temperature)

If it is assumed that the channel coolant bulk temperature in the upstream unenhanced region is the same as the bulk temperature in the downstream measurement region, then the dimensionless enhancement factor can be

determined solely from the measured surface heat flux values. This implies that it is not necessary to approximate the channel bulk temperature, which is used to determinine the surface heat transfer coefficient and dimensionless Nusselt number.

However, to validate the experimental channel, a comparison was made against an experimentally obtained channel surface Nusselt number value and an analytical approximation thereof for the case of turbulent flow in a rectangular channel without suction. This requires an accurate estimate of the channel bulk temperature which was obtained by making use of an approximation provided by Byerley [27].

The approximation allows for the conversion of a centre-point temperature measurement into a bulk temperature value for a square channel. If it is assumed that the 1/7th power law accurately approximates the velocity and temperature profile within the channel, then the velocity profile is described by:

$$u = u_{centre}\left(\frac{y}{\delta}\right)^{1/7} \qquad [3.1]$$

and the temperature profile described by:

$$T = \left(T_{centre} - T_{wall}\right)\left(\frac{y}{\delta}\right)^{1/7} + T_{wall} \qquad [3.2]$$

which can be substituted into:

$$T_{bulk} = \frac{\int_0^{\delta} uT\,dy}{\int_0^{\delta} u\,dy} \qquad [3.3]$$

yielding:

$$T_{bulk} = \frac{8}{9}\left(T_{centre} - T_{wall}\right) + T_{wall} \qquad [3.4]$$

This provides an experimental approximation of the bulk temperature in the channel with δ representing the hydrodynamic boundary layer thickness.

Furthermore, taking into account that the coolant flow inside the channel is incompressible, the momentum equation can then be decoupled from the governing energy equation. This allows the heat transfer coefficient to be described by:

$$h = \frac{9}{8}\left(\frac{\dot{q}}{T_{centre} - T_{wall}}\right) \qquad [3.5]$$

III. Material properties

The data-reduction technique used to derive the heat flux from the surface temperature measurements requires knowledge of the substrate thermal product $\sqrt{\rho C_p k}$. As the *Macor* ceramic substrate material is baked during the gauge construction, there is generally some diffusion of the platinum into the substrate which changes its thermal properties [50]. Therefore, the thermal properties of the ceramic should be experimentally measured after the gauges have been fired onto the substrate.

An additional piece of *Macor* ceramic with a single thin-film platinum gauge, to be used to determine the thermal properties, underwent the same thermal processing procedures as the actual test channel. To determine the thermal product of this section, a simple technique reffered to as the Joule effect was implemented. This method is well documented by Dunn [49], Schultz and Jones

[50] and Skinner [70]. This involves the measurement of the thermal product by applying a step function in heat flux of known amplitude to the surface of the gauge and sampling the temperature history to obtain the thermal product from Equation 2.12.

Two measurements are made; the first in air and the second in distilled water. For the first measurement (in air), the assumption is that thermal energy is only diffusing into the substrate. Although this measurement would be more accurate when performed in a vacuum (thereby ensuring that all the heat flux goes into the substrate), a measurement in air is of acceptable accuracy since the gauge dimensions are so small and the heat flux extracted due to natural convection can be assumed to be negligible. The second measurement is done in distilled water where it is assumed that thermal diffusion occurs both into the substrate and into the liquid with the gauge representing a constant area to both these heat sinks.

The respective heat fluxes from both measurements can be represented by Equation 2.14, with the magnitude of the fluxes estimated from the current intensity and the gauge resistance. Knowing the thermal parameters of distilled water, the lumped thermal parameter can then be determined. This method was applied to obtain 10 individual measurements which provided a dispersion of 7% and an overall mean thermal product value of 2061 $J/m^2Ks^{0.5}$. A comparison between the experimentally obtained thermal product and values obtained by Denos et al. [52] showed a discrepancy of less than 6%.

IV. Radiation Effects

The test channel is placed in a controlled ambient environment (inside the furnace) and as a result radiation losses to the surrounding "environment" can be assumed to be negligible. During testing, it is assumed that the wall temperature of the various inner surfaces decrease at approximately the same rate, resulting in a negligible temperature difference between the various surfaces. Therefore, convection heat transfer dominates any radiation effects that might be present.

3.6 UNCERTAINTY ANALYSIS

The experimental uncertainty of the channel was determined using a case study which considered a channel flow Reynolds number of 25 000 without any coolant extraction. Figure 3.13 shows the surface heat flux profile which was obtained from the case study with relation to time. A linear regression data fit was obtained from the surface heat flux versus surface temperature profile, displayed in Figure 3.14, to obtain this surface heat flux measurement. Table 3.1 provides a summary of the measured results.

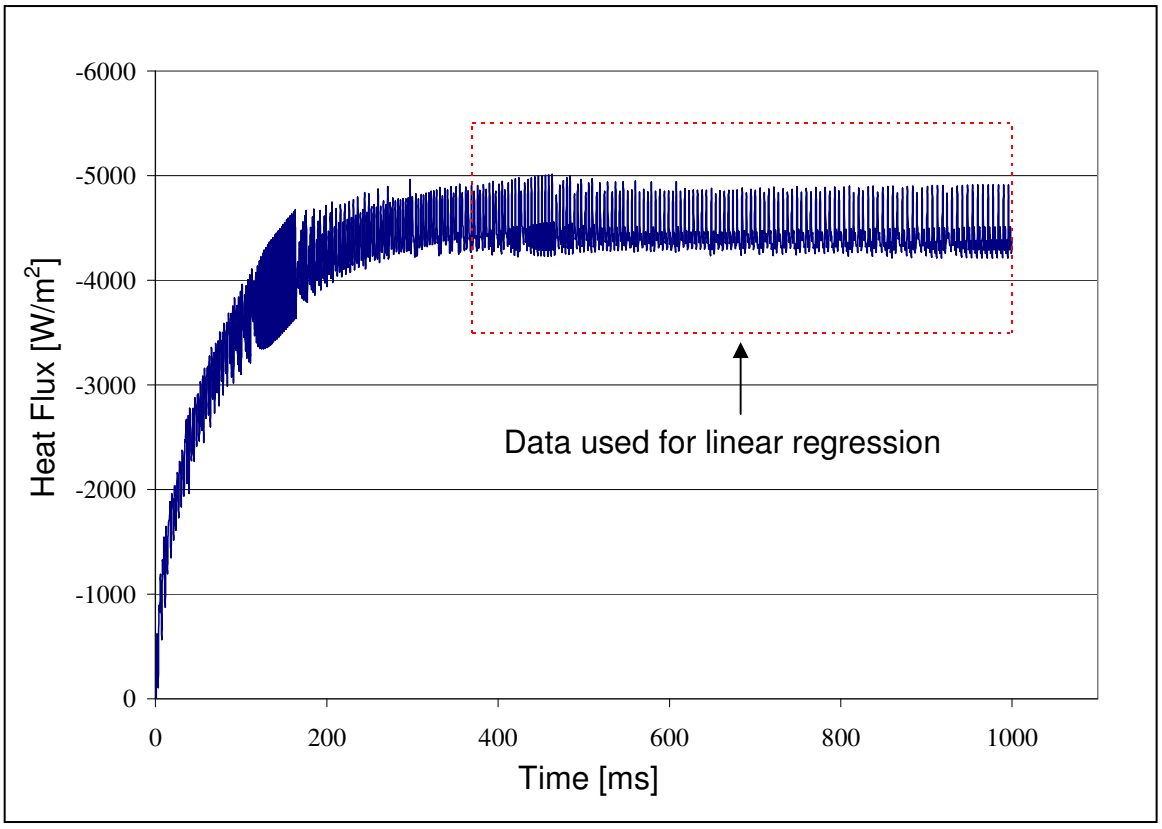

FIGURE 3.13: *Surface heat flux profile*

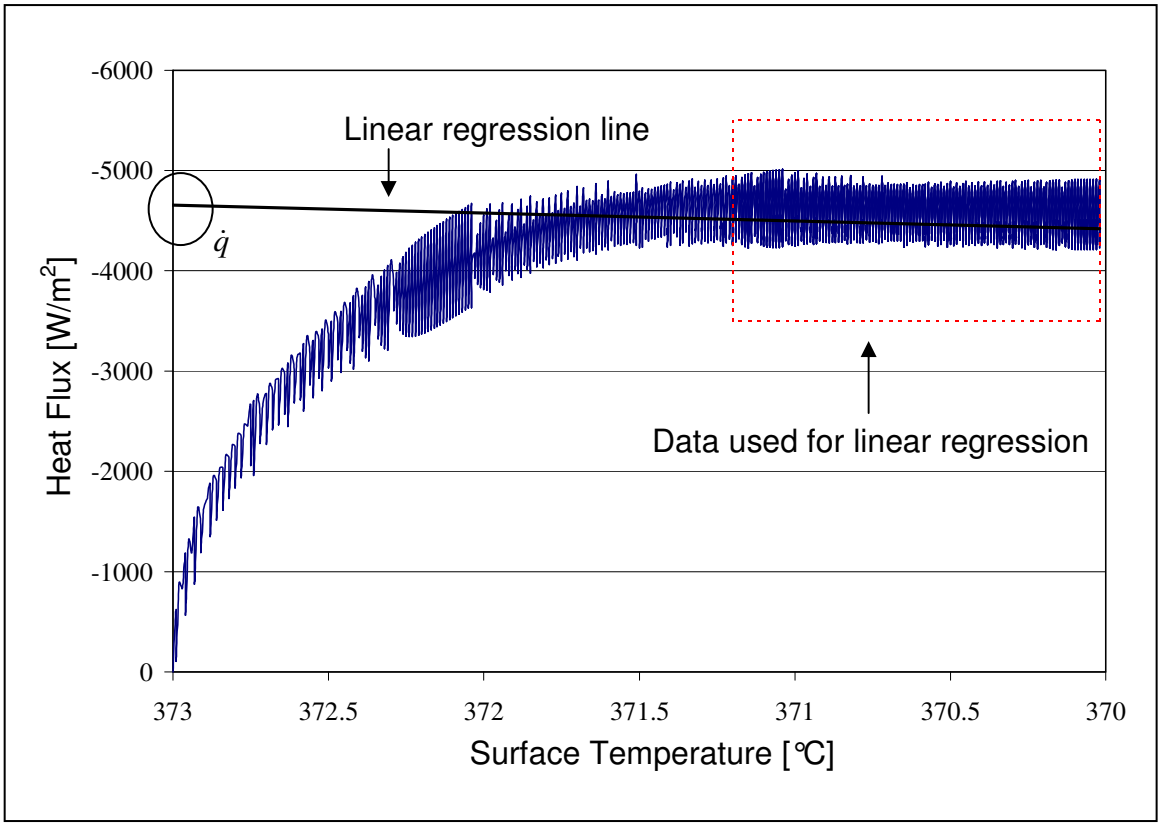

FIGURE 3.14: *Heat flux versus surface temperature*

TABLE 3.1: *Experimental results*

T_{bulk} [K]	300.56
$\dot{q}$ [W/m^2]	-4682
h [W/m^{2}K]	64.63
Nu	59.97

An uncertainty analysis was performed on the experimental results using the method developed by Kline and McClintock [69] for single-sample experiments. The proposed method describes the uncertainty of a function:

$$U = U(z_1, z_2, ..., z_n) \qquad [3.6]$$

With the following relation:

$$w_u = \left[\left(\frac{\partial U}{\partial z_1} \cdot w_{z_1} \right)^2 + \left(\frac{\partial U}{\partial z_2} \cdot w_{z_2} \right)^2 + \ldots + \left(\frac{\partial U}{\partial z_n} \cdot w_{z_n} \right)^2 \right]^{1/2} \qquad [3.7]$$

The term, $w_{u,}$ represents the amount of uncertainty when using the function U, as indicated by the footnote.

The experimentally determined thermal product provided a dispersion of 7% which represents a surface flux uncertainty of approximately 2%. The oil bath temperature gauge, used to calibrate the thin-film gauges on the substrate wall, has an uncertainty of ±0.3 °C and the gas temperature sensors in the test channel an uncertainty of ±0.8 °C. This implies that the maximum temperature difference uncertainty between the wall temperature and gas temperature can be considered to be ±1.1 °C.

The uncertainty regarding the parameters in Equation 3.5 can be expressed as:

TABLE 3.2: *Heat transfer coefficient error analysis*

$w_{\dot{q}} = \pm 93.6\ \mathrm{W/m^2}$	$\left(\frac{\partial h}{\partial q} \cdot w_{\dot{q}} \right)^2 = 1.669$
$w_{\Delta T} = \pm 1.1\ ^\circ\mathrm{C}$	$\left(\frac{\partial h}{\partial \Delta T} \cdot w_{\Delta T} \right)^2 = 0.761$
$\therefore w_h = \pm 1.559\ \mathrm{W/m^2K}$	

The terms $w_{\dot{q}}$ and $w_{\Delta T}$ represent the amount of uncertainty regarding the heat flux measurement and the net temperature measurement. This provides a heat transfer coefficient uncertainty of $w_h = \pm 1.559\ \mathrm{W/m^2K}$ which is equivalent to a Nusselt number uncertainty of less than 3%.

The experimental results were also compared with an analytical Nusselt number correlation for turbulent flow in a square duct with smooth isothermal walls and fully developed hydrodynamics and heat transfer [58]:

$$Nu = \frac{(f/8)(\mathrm{Re}-1000)\mathrm{Pr}}{1+12.7(f/8)^{1/2}\left(\mathrm{Pr}^{2/3}-1\right)} \qquad [3.8]$$

The term f represents the friction factor and is defined as:

$$f = (0.79\ln \mathrm{Re}-1.64)^{-2} \qquad [3.9]$$

The analytical results for a flow Reynolds number of 25 000 are displayed in Table 3.3:

TABLE 3.3: *Analytical results*

f	0.0247
Pr	0.69
Nu	61.052

A comparison between the measured and the analytical Nusselt number values provided excellent agreement, indicating a disparity of less then 2%.

3.7 EXPERIMENTAL SCOPE

The principal factors which influence near-hole heat transfer augmentation are:

I. The film-cooling hole suction ratio

II. The film-cooling hole extraction angle

The objective of the experimental investigation is to test within the same scope as Byerley [27] and address the uncertainties which were stipulated in Section 1.1.4. The experimental scope of the current study is schematically illustrated in Figure 3.15.

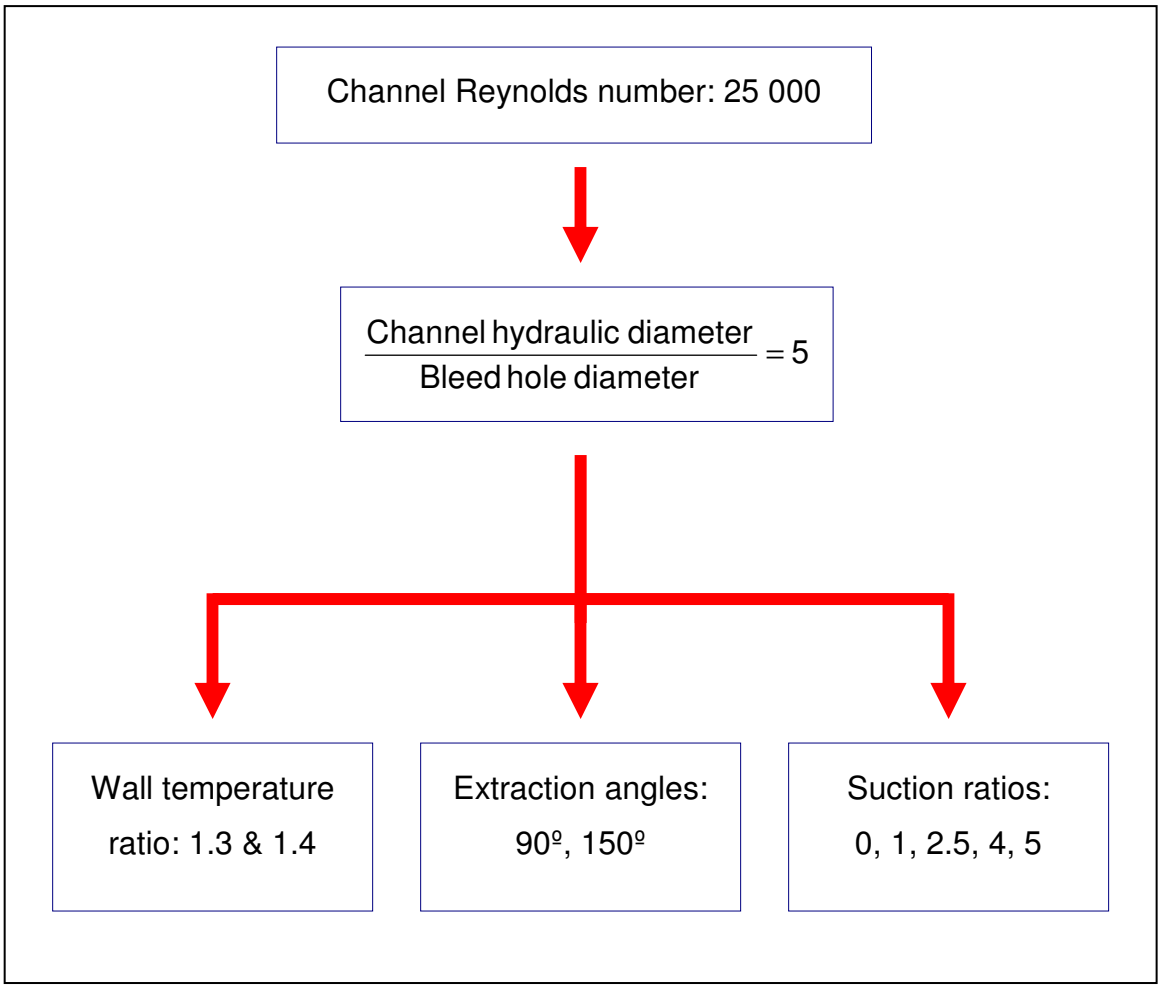

FIGURE 3.15: *Schematic of the experimental scope*

All tests were done at a channel Reynolds number of 25 000. A coolant extraction hole diameter of 5 mm was chosen to provide a channel hydraulic diameter to bleed hole diameter ratio of 5, which is representative of the ratio found on actual turbine blades. Two wall-to-coolant temperature ratios were considered. That is a ratio of 1.3 and 1.4 which translates to a wall temperature of 100 °C and 130 °C. Bleed hole extraction angles of 90º and 150º were used. Although the 150º extraction angle may not be as common, previous studies indicated that augmentation induced by the 150º extraction angle

diverges enough that it should be considered. The suction ratio was varied between zero and five. The experimental study published by Byerley [27] was conducted in a rectangular channel with widened sidewalls to neglect its possible influence on the downstream heat transfer. The current study implements a square channel to determine whether channel sidewalls will influence the heat transfer augmentation.

3.8 EXPERIMENTAL PROCEDURE

The following is a step-by-step description of the experimental procedure.

I. The required extraction hole geometry insert is fitted to the experimental channel and sealed in the furnace. The furnace is then heated to the desired temperature and left for a prolonged period (12 hours) to ensure that the channel and furnace reaches thermal equilibrium.

II. Once thermal equilibrium has been reached, the compressor is started and all regulators and valves are adjusted to obtain the correct duct Reynolds number and hole suction ratio.

III. The data-acquisitioning system is switched on and the system is inspected for any discrepancies.

IV. Prior to coolant blowdown, data sampling commences.

V. Channel blowdown is initiated by charging the solenoid valve and measurements are taken for approximately 10 seconds.

VI. Once the data acquisitioning is stopped, the extraction hole pressure is adjusted to the correct suction ratio for the following test. The channel flow is then stopped.

VII. The unprocessed results are quickly reviewed for any inconsistencies.

VIII. Testing is resumed after a period of 40-50 minutes, thereby allowing the heated substrate to reach thermal equilibrium.

3.9 CONCLUSION

The experimental setup was discussed in the current chapter. This included a discussion of the experimental channel, the gauge construction, data acquisitioning and an uncertainty analysis. The chapter concluded with a summary of the experimental scope and procedure

CHAPTER 4
NUMERICAL INVESTIGATION

4.1 PREAMBLE

The objective of the numerical investigation is to compare the experimental results with computational predictions of the surface heat transfer enhancement downstream of the coolant extraction hole. A commercial Computational Fluid Dynamics (CFD) package, *Fluent* 6.2, was used to numerically model the experimental domain.

The modelling of turbulent flow is one of the most challenging problems in CFD. The accuracy with which the turbulent boundary layer can be predicted numerically depends on the turbulence closure model which is being used. The accuracy of the turbulent boundary layer prediction affects the accuracy of the surface heat transfer prediction, since wall and fluid interaction will influence the amount of convection.

In general, there are three methods with which turbulence can be predicted:

I. Turbulence modelling in which Reynolds averaging is implemented to model the turbulent eddies instead of directly calculating it. This is the most widely adopted method for practical engineering applications since it vastly reduces the computational effort.

II. The Large Eddy Simulation (LES) approach where the computational grid is refined enough to directly calculate the larger turbulent eddies and model the sub-grid scale eddies.

III. The direct simulation method where the Navier-Stokes equations are applied directly on a mesh which is fine enough to resolve the smallest length scale of turbulence. This method requires a very fine grid scale and is therefore also computationally the most expensive.

The numerical modelling of coolant extraction requires accurate modelling of boundary layer renewal and flow impingement downstream of the film-cooling hole entrance. The best method of simulating this flow condition will be to implement direct simulation to solve the flow within the boundary layer.

This approach is currently not a practical engineering tool since it is computationally too expensive and is therefore not implemented in the current study. As an alternative, various Reynolds averaging turbulence models and a derivative of the LES model are considered which will be implemented with the use of wall functions to model the flow condition inside the boundary layer of the flow field instead of solving it directly. Although this approach will provide results which are less accurate than a direct simulation or even a dedicated LES model, it will provide an indication regarding the ability of turbulence models to predict the flow field considered

4.2 GOVERNING EQUATIONS

The equations which govern fluid motion and heat transfer constitute the continuity, momentum and energy equations. Collectively, these equations are known as the Navier-Stokes equations.

The Navier-Stokes equations consist of non-linear partial differential equations with a complex dependency within the equation system. This greatly confines the applicability of these equations, since only in specific cases are they solvable with the current known mathematics. There are also only a very limited amount of flow conditions that entitle the simplification of these governing equations to allow the possibility of achieving an

analytical solution. Consequently, for the majority of these cases, the Navier Stokes equations can only be solved through numerical approximation.

These equations will now be considered individually:

I. Continuity equation

The continuity equation states the conservation of mass, which is valid except for nuclear reaction environments. In its conservative form it is represented by:

$$\frac{\partial \rho}{\partial t} + \frac{\partial \rho U_i}{\partial x_i} = 0 \qquad [4.1]$$

The first term represents the rate at which density changes and the second term characterises the net outflow of mass across the boundary.

II. Momentum equation

The momentum equation describes a force balance which from Newton's 2nd law states that mass times acceleration is equal to the imposed force. For an incompressible Newtonian fluid, the momentum equation is represented by:

$$\frac{\partial \rho U_i}{\partial t} + \frac{\partial \rho U_i U_j}{\partial x_j} = \rho g_i + F_i - \frac{\partial P}{\partial x_i} + \frac{\partial}{\partial x_j}\left(2\mu S_{ij}\right) \qquad [4.2]$$

where F_i represents an additional body force that can affect the fluid motion such as rotation or a magnetic field.

III. Energy equation

The first law of thermodynamics states that the exchange of energy for a system is the result of applied work and heat transfer through that region. The energy equation is obtained by applying the first law of thermodynamics to a

fluid, passing through an infinitesimal, fixed control volume. In its most complete form, the energy equation is described by [71]:

$$\frac{\partial \rho E_0}{\partial t} + \frac{\partial \rho U_i E_0}{\partial x_i} = \rho U_i F_i - \frac{\partial q_i}{\partial x_i} + \frac{\partial}{\partial x_j}\left(U_i T_{ij}\right) \qquad [4.3]$$

where T_{ij} represents surface forces similar to the viscosity and pressure terms in the momentum equation. The term E_0 represents the total internal energy, including the kinetic energy.

4.3 TURBULENCE MODELLING

Turbulence is the unsteady three-dimensional process by which flow velocity fluctuates seemingly randomly over a wide range of frequencies. Since these fluctuations can be of a small scale and high frequency, they are computationally too expensive to simulate directly in practical engineering calculations. To account for this problem turbulent flow is modelled instead of solved. This significantly decreases the computational effort involved and is referred to as Reynolds averaging.

With Reynolds averaging, the solution variables in the Navier-Stokes equations are decomposed into mean and fluctuating components to form the Reynolds-Averaged-Navier-Stokes (RANS) equations. These equations have the same general form as the instantaneous Navier-Stokes equations, but with the velocities and other solution variables represented by time-averaged values. A supplementary Reynolds stress term, $-\rho\overline{u_i' u_j'}$, is added to represent the effects of turbulence.

The Reynolds-averaged approach to turbulence modelling requires that the added Reynolds stresses be adequately modelled. The modelling of the stress terms can be done

by one of two methods, i.e. the Boussinesq method (or eddy viscosity model) or the Reynolds Stress Model (RSM):

I. The Boussinesq model

With the Boussinesq hypothesis, the Reynolds stresses are related to the mean velocity gradients as represented by:

$$-\rho\overline{u_i'u_j'} = \mu_t\left(\frac{\partial U_i}{\partial x_j}+\frac{\partial U_j}{\partial x_i}\right)-\frac{2}{3}\mu_t\frac{\partial U_k}{\partial x_k}\delta_{ij}-\frac{2}{3}\rho k\delta_{ij} \qquad [4.4]$$

where μ_t represents the turbulent eddy viscosity.

The advantage of the Boussinesq approach is that it requires relatively low computational cost with regard to the computation of the turbulent viscosity. However, the main disadvantage of this method is that it assumes that the turbulent viscosity is an isotropic scalar quantity which is not necessarily true.

This approach has been adopted in turbulence models like the Spalart-Allmaras model [72] (which represents turbulent viscosity with a single transport equation), the *k*-*ε* model [73] and the *k*-*ω* model [74]. In the two *k* models, the turbulent viscosity is represented by two additional transport equations where the term *k* characterises the turbulent kinetic energy, *ε* the turbulent dissipation rate and *ω* the specific dissipation rate.

A derivative of the *k*-*ω* model is the shear-stress transport (SST) *k*-*ω* model [75], which effectively implements the *k*-*ω* model in the near-wall region and the *k*-*ε* model in the far field.

II. The Reynolds-stress model

The Reynolds-stress model [76] solves individual transport equations to solve the Reynolds stresses. Turbulent viscosity is therefore not employed, implying that no

isotropic assumptions are made. This however, means that seven additional transport equations must be solved (for a three-dimensional flow field) which increases the computational expense.

The transport terms used to describe the Reynolds stresses with the RSM model are represented by Equation 4.5. The terms on the right-hand side represent convection, turbulent diffusion, molecular diffusion, stress production, buoyancy production, pressure strain and dissipation.

$$\frac{\partial}{\partial t}\left(\rho\overline{u_i'u_j'}\right) = -C_{ij} - D_{T,ij} + D_{L,ij} - P_{ij} - G_{ij} + \phi_{ij} - \varepsilon_{ij} \qquad [4.5]$$

where :

$$C_{ij} = \frac{\partial}{\partial x_k}\left(\rho u_k \overline{u_i'u_j'}\right)$$

$$D_{T,ij} = \frac{\partial}{\partial x_k}\left[\rho\overline{u_k u_i'u_j'} + \overline{p\left(\delta_{kj}u_i' + \delta_{ik}u_j'\right)}\right]$$

$$D_{L,ij} = \frac{\partial}{\partial x_k}\left[\mu\frac{\partial}{\partial x_k}\left(\overline{u_i'u_j'}\right)\right]$$

$$P_{ij} = \rho\left(\overline{u_i'u_k'}\frac{\partial u_j}{\partial x_k} + \overline{u_j'u_k'}\frac{\partial u_i}{\partial x_k}\right)$$

$$G_{ij} = \rho\beta\left(g_i\overline{u_j'\vartheta} + g_j\overline{u_i'\vartheta}\right)$$

$$\phi_{ij} = \overline{p\left(\frac{\partial u_i'}{\partial x_j} + \frac{\partial u_j'}{\partial x_i}\right)}$$

$$\varepsilon_{ij} = 2\mu\frac{\partial u_i'}{\partial x_k}\frac{\partial u_j'}{\partial x_j}$$

An alternative to Reynolds averaging is the LES model which computes the large eddies in a time-dependent solution by implementing the filtered Navier-Strokes equations. The rationale behind the LES method is that by resolving the larger turbulence eddies and modelling the smaller eddies, fewer errors will be introduced in the final analysis.

Filtering is a mathematical manipulation of the exact Navier-Stokes equations to remove eddies which are smaller than the mesh size from the solution. These smaller eddies tend to be more isotropic than the larger eddies, which render their modelling via a Boussinesq approach more acceptable. For this reason, the LES approach requires highly accurate spatial and temporal discretizations, which inherently increases the computational time and effort.

The Detached Eddy Simulation model (DES) is a practical alternative to the LES approach. The DES model implements an unsteady Reynolds-averaging version of the Spalart-Allmaras model with a filtered LES version of the same model to create two separate regions inside the flow domain [77]. With this RANS-LES model, the LES-based model is used to solve the mainstream flow domain, whereas the RANS-based model is used to solve the near-wall domain.

In the current study, the *k-ω, k-ω* SST, RSM and DES turbulence models are implemented.

4.4 NEAR-WALL TREATMENT

The prediction of the channel frictional drag, pressure drop and near-wall heat transfer will depend on the accuracy of near-wall modelling. The near-wall region can largely be subdivided into three layers as displayed in Figure 4.1. The innermost region is referred to as the viscous sub-layer. The flow in this region is almost laminar since turbulence is damped out by viscous shear. Molecular viscosity plays a dominant role in the momentum and heat or mass transfer in this region.

The interim region, between $5 \leq y^+ \leq 30$, is also referred to as the buffer layer where the influence of molecular viscosity and turbulence is equally important. In this region, the velocity profile is neither linear nor logarithmic, but instead a smooth transition between

the two. This leads to the third layer, known as the fully turbulent region or log law layer where turbulence dominates the flow region.

Equation 4.6 is formula deduced by Spalding [78] which describes the transition of the velocity profile between the wall, throughout the inner layer, up to the point where the outer layer begins (usually at $y^+>100$) [67]. The terms κ and B are constants with values of 0.4 and 5.

$$y^+ = u^+ + e^{-\kappa B}\left[e^{\kappa u^+} - 1 - \kappa u^+ - \frac{(\kappa u^+)^2}{2} - \frac{(\kappa u^+)^3}{6}\right] \qquad [4.6]$$

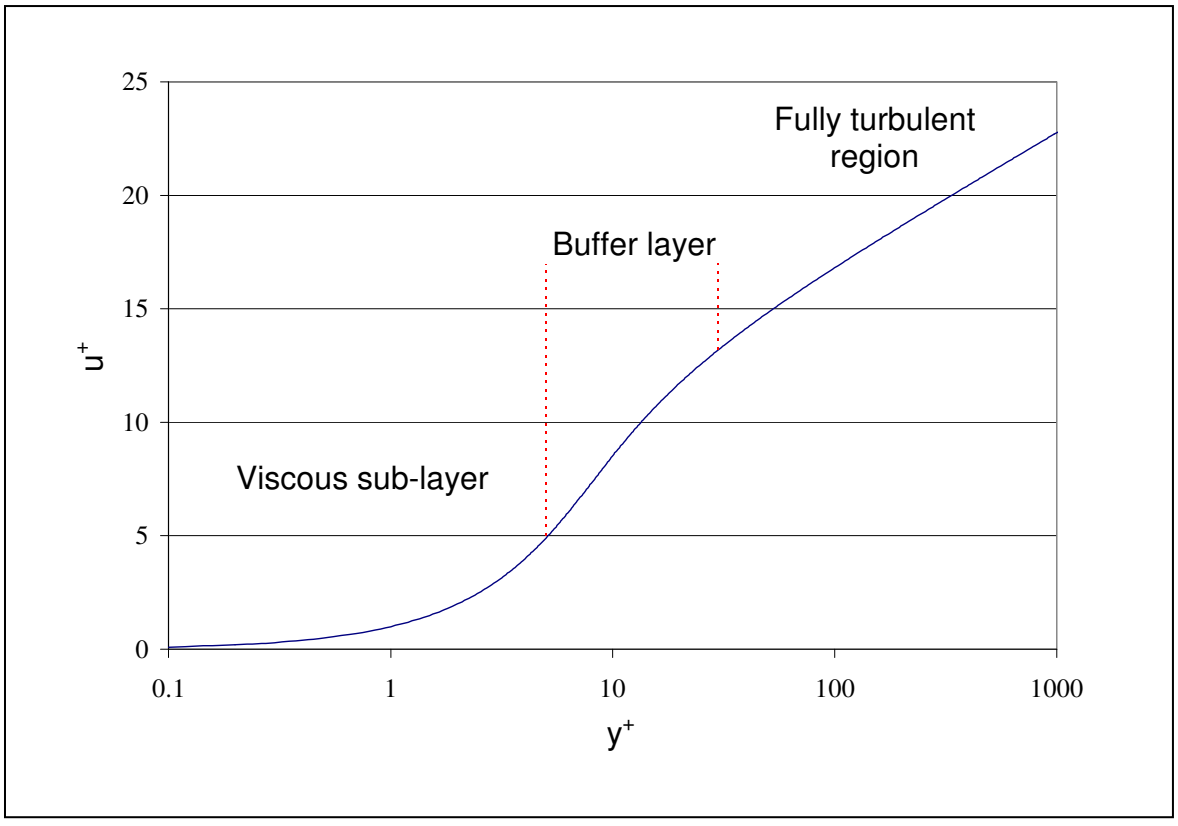

FIGURE 4.1: *Subdivisions of the near-wall region*

The numerical models under consideration provide the following approaches regarding near-wall treatment:

I. The *k-ω* and *k-ω* SST turbulence models implement a low-Reynolds number boundary condition with an enhanced wall treatment if the wall adjacent cells are situated in the viscous sublayer ($y^+ \leq 5$). If, however, the wall adjacent cells are outside the buffer layer ($y^+ \geq 30$), wall functions are used to model the near-wall region. Wall functions are a collection of semi-empirical formulas which are used to link the solution variables in the near-wall cell and the corresponding quantity on the wall [79].

II. The RSM turbulence model provides the option of implementing a standard or a non-equilibrium wall function approach [80]. Non-equilibrium wall functions are recommended for a flow field involving separation, reattachment and impingement. This requires that the wall adjacent cells be located within the log-law layer, $30 < y^+ \leq 300$, preferably close to the lower boundary ($y^+ \approx 30$).

III. The DES model implements the Spallart-Allmaras turbulence model in the near-wall region. This model is implemented outside the laminar sub-layer, which implies that the law of the wall is implemented to solve the near-wall velocity profile.

An initial y^+ sensitivity study was done to determine the influence of the wall adjacent cells regarding the boundary layer flow simulation with the *k-ω* turbulence model. Simulations were done for turbulent air flow in a square channel with y^+ values of 40, 32, 27 and 23. A comparison was made regarding the surface heat transfer values. Similar values were obtained for the y^+ values of 40, 32 and 27 while a divergence in the region of 12% was noted for a y^+ value of 23.

4.5 NUMERICAL MODEL

The numerical model represents the square experimental channel section. The length of the channel is 500 mm long, which is equal to 20 internal diameters. The extraction hole is situated in the middle of the channel and has a distance of 10 bleed hole diameters. The channel walls are modelled as smooth.

The computational grid and boundary conditions implemented on the numerical model will now be considered:

I. Computational grid

An unstructured hexahedral mesh was used to discretize the numerical domain. The number of cells which were implemented was determined through a mesh independence study. The study considered mesh sizes with different degrees of non-uniform grid spacing in the main channel and a constant boundary layer cell size which provided a y^+ value of approximately 30. The grid spacing was dense in the region of the extraction hole, where the higher flow gradients were expected, and gradually increased further away where the flow properties were assumed to be more uniform. Grid sizes of 2×10^5, 4×10^5, 8×10^5 and 1.6×10^6 cells were considered and comparisons were made regarding the magnitude of surface heat transfer. The results of the various simulations are displayed in Table 4.1.

TABLE 4.1: *Mesh-independence study*

Number of cells	Surface heat transfer [W/m^2]
200 000	3944
400 000	4614
800 000	4672
1 600 000	4649

As can be seen, similar surface heat transfer values were obtained for the 4×10^5 to 1.6×10^6 cell models while the 2×10^5 cell model showed a small divergence regarding surface heat transfer. The near-hole mesh configuration and cell distribution of the 4×10^5 cell model are displayed in Figure 4.2 and 4.3.

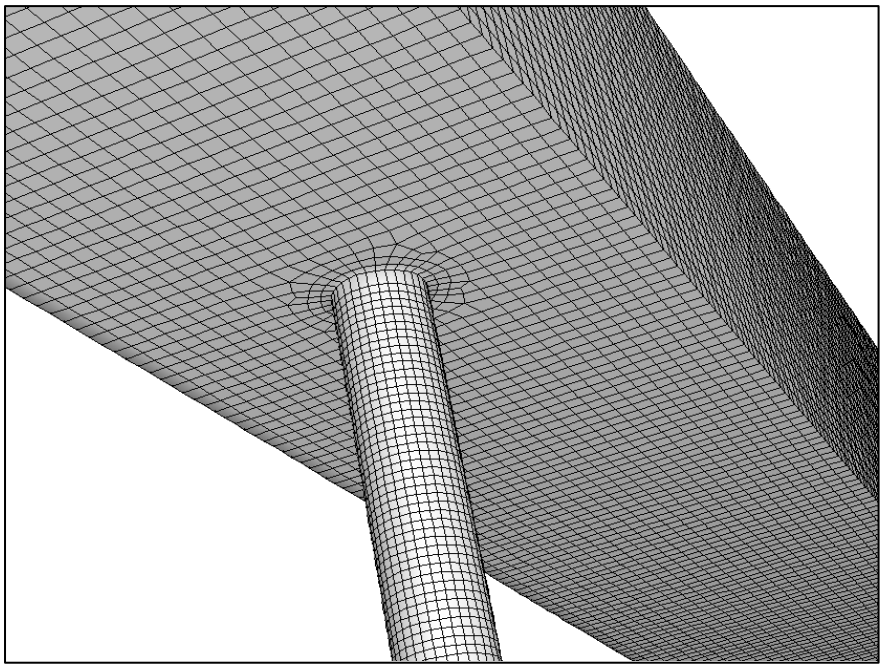

FIGURE 4.2: *Near-hole mesh configuration*

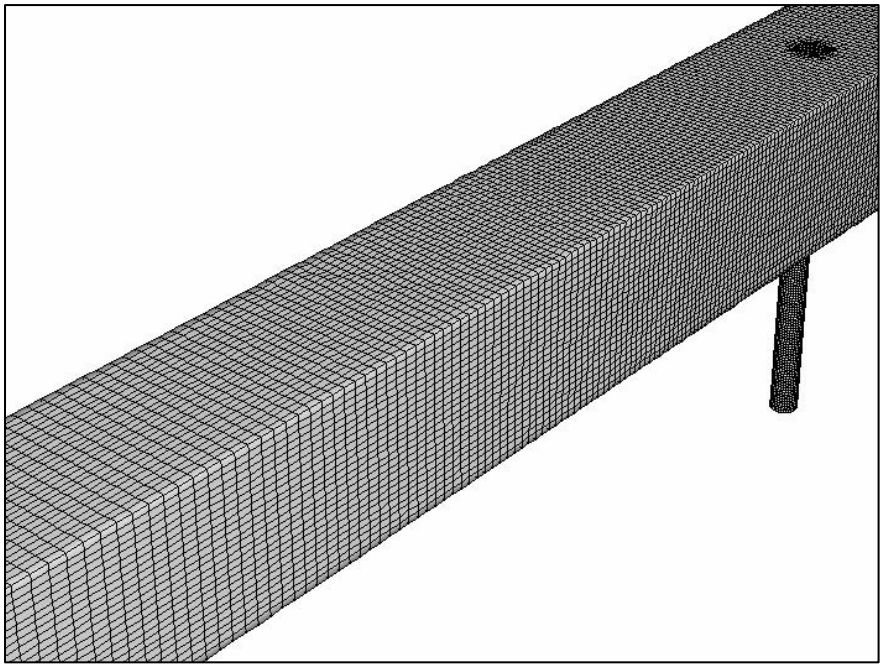

FIGURE 4.3: *Mesh-configuration upstream of the coolant extraction hole*

II. Boundary conditions

The boundary surfaces are displayed in Figure 4.4. A mass flow boundary condition was used at the channel inlet, and pressure boundaries at the channel and bleed hole outlet. Experimentally measured mass flow and extraction hole outlet pressure values were implemented as flow boundary conditions to the numerical model. These values are displayed in Table 4.2.

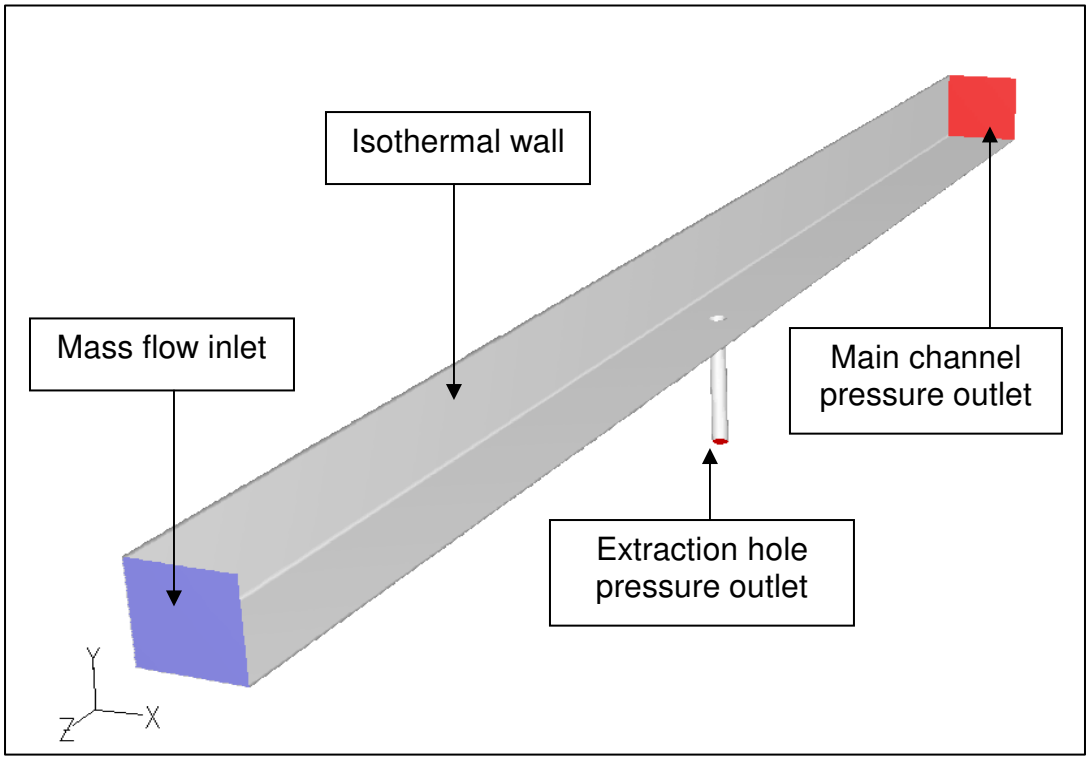

FIGURE 4.4: *Numerical domain with boundary conditions*

The channel walls, coloured in grey, are modelled as isothermal with a wall temperature of 100 °C. This is done to replicate the isothermal substrate walls approximated by the transient experimental technique.

The material properties of air, such as specific heat, thermal conductivity and viscosity were prescribed as a function of temperature [58].

TABLE 4.2: *Boundary Conditions*

Absolute Pressure	187.625 kPa
Inlet Mass Flow Rate	0.1 kg/s
90° Extraction Hole Outlet Gauge Pressure	
Suction Ratio = 5	-3530 Pa
Suction Ratio = 2.5	-960 Pa
150 ° Extraction Hole Outlet Gauge Pressure	
Suction Ratio = 5	-3820 Pa
Suction Ratio = 2.5	-1030 Pa

4.6 CONCLUSION

The first part of this chapter discussed the governing equations with regard to numerical modelling in detail and provided an overview of the turbulence models which were implemented in the current study. This was followed by a review of the near-wall modelling approach adapted by the turbulence models under consideration and a y^+ sensitivity study with the *k*- ω turbulence model. The study showed a negligible influence on the wall heat transfer for a wall adjacent cell size which provides a y^+ value of 30. The chapter was concluded with an overview of the numerical model.

CHAPTER 5
EXPERIMENTAL & NUMERICAL RESULTS

5.1 PREAMBLE

The following chapter presents the experimental and numerical results obtained in the current study. The experimentally measured data is presented as line averaged heat transfer enhancement values downstream of the extraction hole. The position of each measurement is defined as the ratio between the distance downstream of the extraction hole, x, and the diameter of the hole, D, as illustrated in Figure 5.1. The length used for averaging is a distance of two extraction hole diameters ($2D$), and was chosen to superimpose the area of heat transfer enhancement.

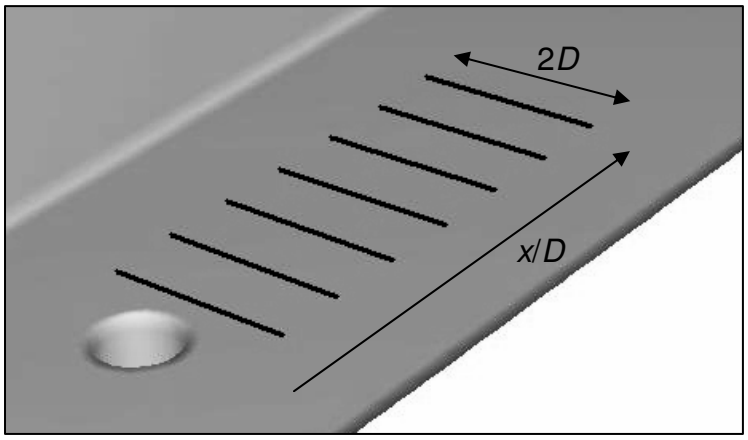

FIGURE 5.1: *Line averages downstream of the extraction hole*

The experimentally measured heat transfer values were non-dimensionalised by dividing the heat transfer measurement downstream of the extraction hole (enhanced region) by the reference surface heat transfer measurement upstream of the extraction hole.

The experimental and numerical results will be presented in the following order:

I. In Section 5.2 the experimental measurements downstream of the coolant extraction hole will be compared with results obtained from a previously published study [27] at $SR = 2.5$ and $SR = 5$.

II. Section 5.3 presents the experimental results downstream of the 90° coolant extraction hole at multiple suction ratios. Line averaged heat transfer enhancement profiles are presented for suction ratios ranging from 0 to 5.

III. Section 5.4 presents the experimental results downstream of the 150° coolant extraction hole. Line averaged heat transfer enhancement profiles are presented for suction ratios ranging from 0 to 5 and are compared with the results obtained for the 90º hole.

IV. A comparison between the enhancement obtained downstream of the 90º extraction hole at $T_{wall}/T_{coolant}$ ratios of 1.3 and 1.4 are compared in Section 5.5.

V. Section 5.6 presents the numerical heat transfer enhancement results downstream of the 90° and 150° coolant extraction holes, along with channel flow profiles.

The chapter is concluded in Section 5.7.

5.2 EXPERIMENTAL COMPARISON

A comparison was made between the experimental results obtained in the current study and an analogous study conducted by Byerley [27]. The enhancement profiles, acquired from the associated study, were calculated from heat transfer enhancement contours measured with the use of liquid crystal thermography. These enhancement contours were

obtained by blowing heated air, with a temperature of 90° C to 100° C, through a channel with ambient wall temperatures. Conversely the current study obtained heat transfer enhancement measurements by introducing cold air in a heated channel. In so doing thermal energy is transferred towards the coolant flow, thereby replicating the density gradient in the coolant boundary layer of an actual turbine cooling passage.

The heat transfer enhancement directly downstream of a perpendicular coolant extraction hole ($x/D < 2$) is influenced by a combination of boundary layer renewal and flow impingement. A smoke-flow visualization study, conducted by Byerley [27] on a 90º extraction hole, has shown that the position of coolant impingement downstream of the extraction hole is dependant on the suction ratio as shown in Figure 5.2.

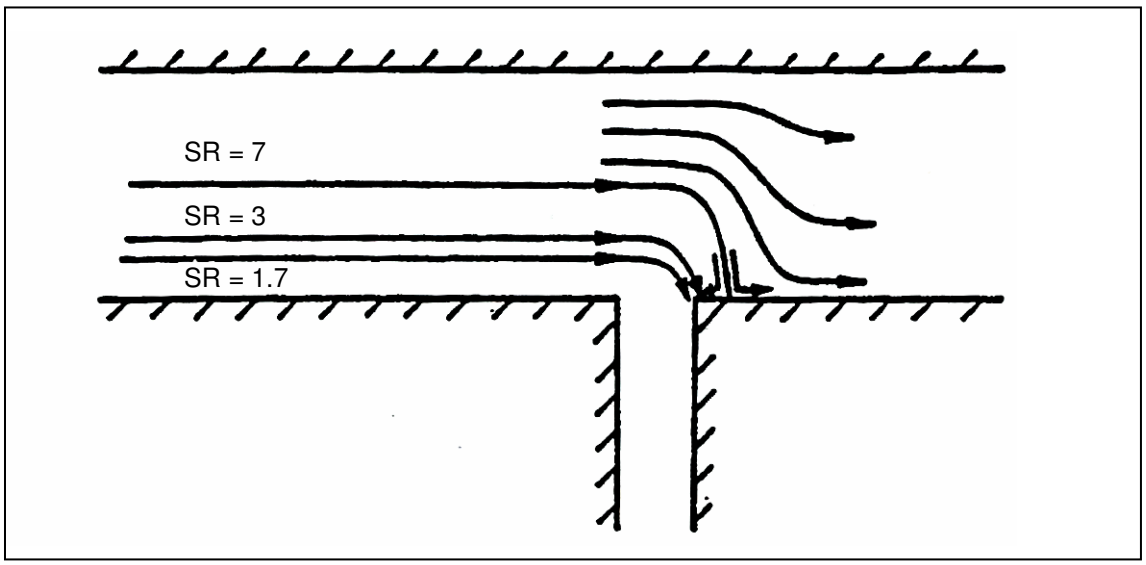

FIGURE 5.2: *Impingement position downstream of a perpendicular extraction hole at different suction ratios* [27]

The study showed that the stagnation point of flow impingement is located near the edge of the coolant extraction hole at a suction ratio of approximately 3. At higher suction ratios the point of impingement moves further downstream of the coolant extraction hole and creates a region of accelerated flow reversal which further contributes to augmentation. From these observations it was concluded that the amount of enhancement directly downstream of a perpendicular extraction hole is primarily influenced by coolant impingement and boundary layer renewal at higher suction ratios ($SR > 3$). At moderate

suction ratios ($SR < 3$) the enhancement induced by impingement is less dominant, which implies that this region is primarily enhanced by boundary layer renewal and to a lesser extent by impingement. For this reason the experimental results obtained in the current study are compared at high ($SR = 5$) and moderate ($SR = 2.5$) suction ratios.

Heat transfer enhancement profiles downstream of the 90º extraction hole, for $SR = 5$ and $SR = 2.5$, are compared in Figure 5.3 with the measurements obtained by Byerley [27]. The measurements show extensive heat transfer augmentation in the near-hole region for both suction ratios.

The near-hole enhancement profile for a $SR = 5$, Figure 5.3, show a difference of less than 10% when compared to the profile obtained by Byerley [27]. Good agreement between the two sets of results is obtained further downstream. The enhancement profile for a $SR = 2.5$, Figure 5.3, provides an even better comparison with the results obtained by Byerley [27], although a small difference is also observed closer to the extraction hole.

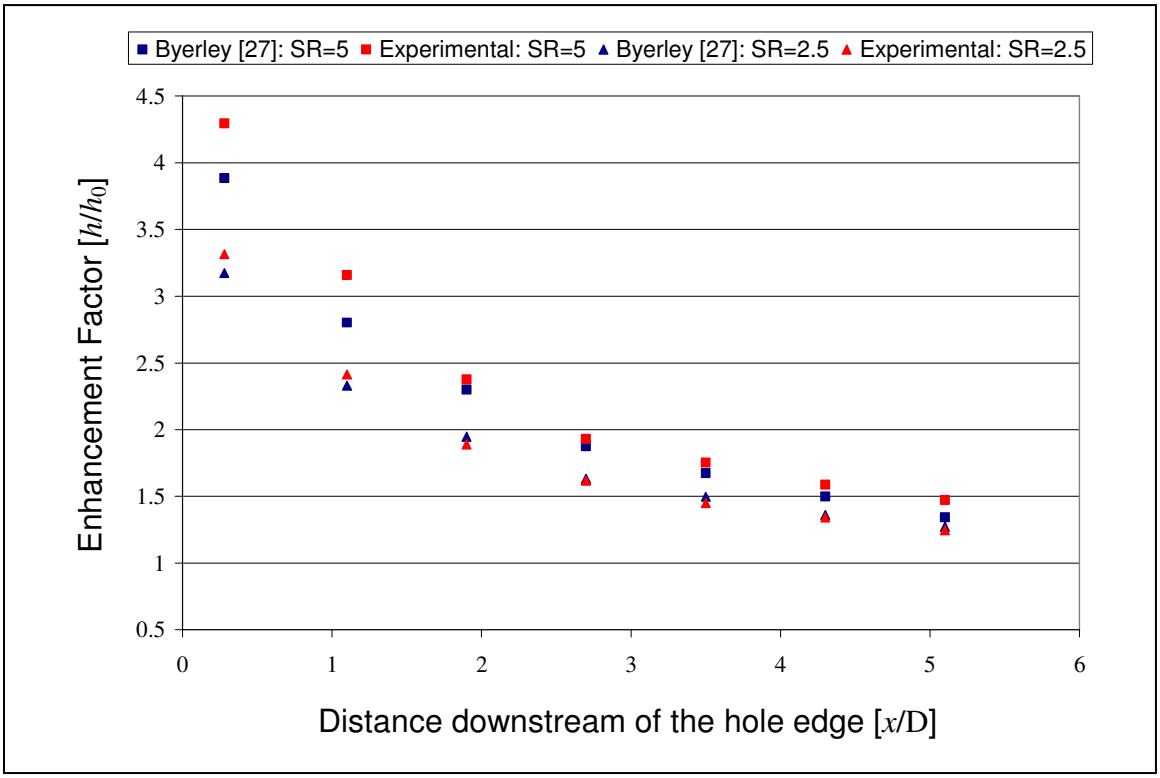

FIGURE 5.3: *Line averaged heat transfer enhancement factors downstream of the 90º extraction hole*

The relevant difference between the two data sets with regard to the near-hole enhancement appears to be greater at the higher suction ratio where impingement is a more dominant enhancement mechanism. Although the difference could be assumed to be negligible, this observation may also indicate that the enhancement induced by impingement is influenced by the thermal gradient in the boundary at the near-hole region.

The heat transfer enhancement profiles downstream of the 150º extraction hole, for $SR = 5$ and $SR = 2.5$, are compared in Figure 5.4. The comparison shows excellent agreement in the near-hole region and further downstream at both high and moderate suction ratios.

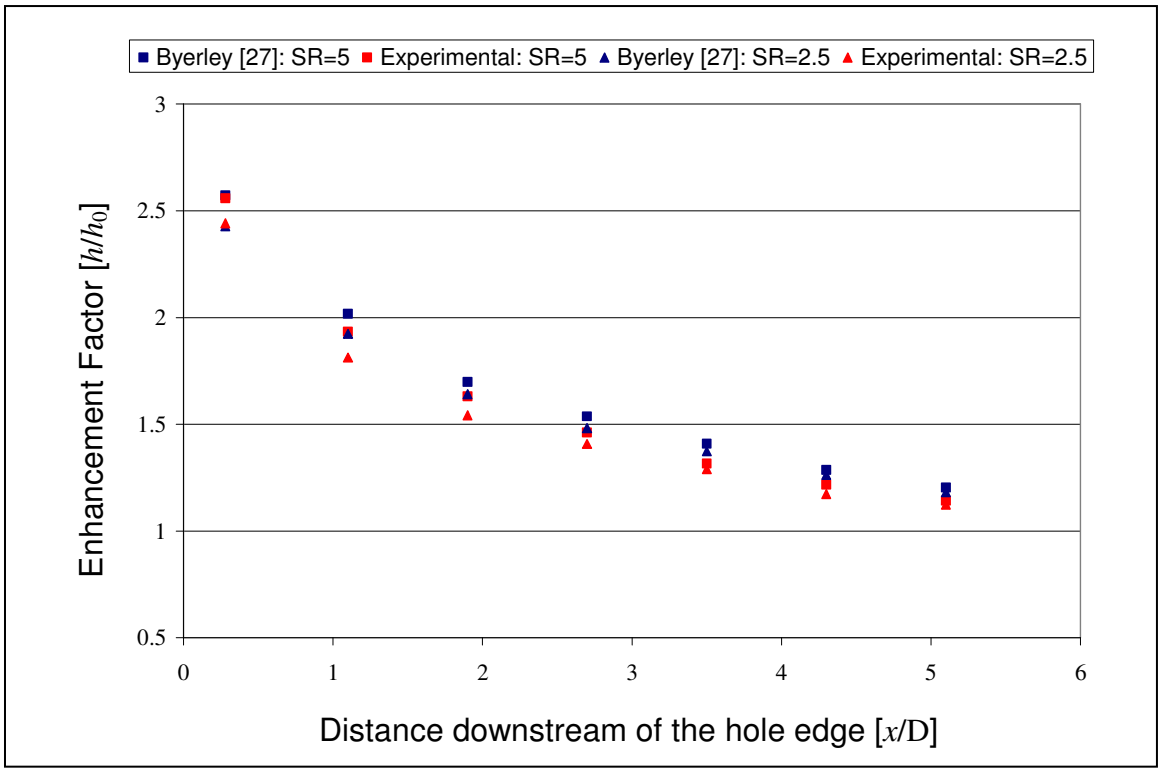

FIGURE 5.4: *Line averaged heat transfer enhancement factors downstream of the 150º extraction hole*

In contrast to the 90º extraction hole comparison, the 150º extraction hole enhancement profiles does not show any significant difference in the near-hole region. It is believed that the higher angle of flow deviation, induced by the backward slanted hole, extensively

limits the amount of coolant impingement downstream when compared to the perpendicular extraction hole. This implies that, contrary to the 90º extraction hole, the near-hole enhancement which is obtained with the 150º extraction hole is primarily influenced by boundary layer renewal at both high and moderate suction ratios.

The good agreement which was obtained between the profiles further downstream ($x/D > 2$), at multiple suction ratios and extraction angles, indicates that the width of the channel has a negligible influence on the heat transfer enhancement induced by coolant extraction. This conclusion can be made since the current study was conducted in a square channel whereas the channel used by Byerley [27] was rectangular, with the sidewalls widened intentionally to neglect any wall effects. Additionally, it should be noted that this observation is made in reference to a channel with a width which is equal to or larger than its height.

Considering the fact that two different measuring techniques were used, good overall agreement was obtained. Furthermore, this observation contributes to the validity of the experimental technique which was implemented in the current study.

5.3 INFLUENCE OF THE SUCTION RATIO

To assess the influence of suction ratio on heat transfer enhancement, measurements were obtained at various suction ratios. Line averaged enhancement profiles downstream of the 90° extraction hole at multiple suction ratios, ranging from $SR = 0$ to $SR = 5$, are displayed in Figure 5.5. Although no coolant is extracted at the zero suction ratio profile, a small amount of near-hole enhancement is observed. This can be attributed to turbulence enhancement in the boundary layer which is induced by flow tripping across the hole edge.

The enhancement profiles show extensive enhancement near the extraction hole, even for a fairly small suction ratio of one. When considering the amount of enhancement across

the suction ratio spectrum, the profiles indicate that the net amount of enhancement decreases exponentially with an increasing suction ratio. This observation is further demonstrated when considering the decreasing gradient of the profile in Figure 5.6, which illustrate the relation between the average heat transfer enhancement and increasing suction ratio for an extraction angle of 90º.

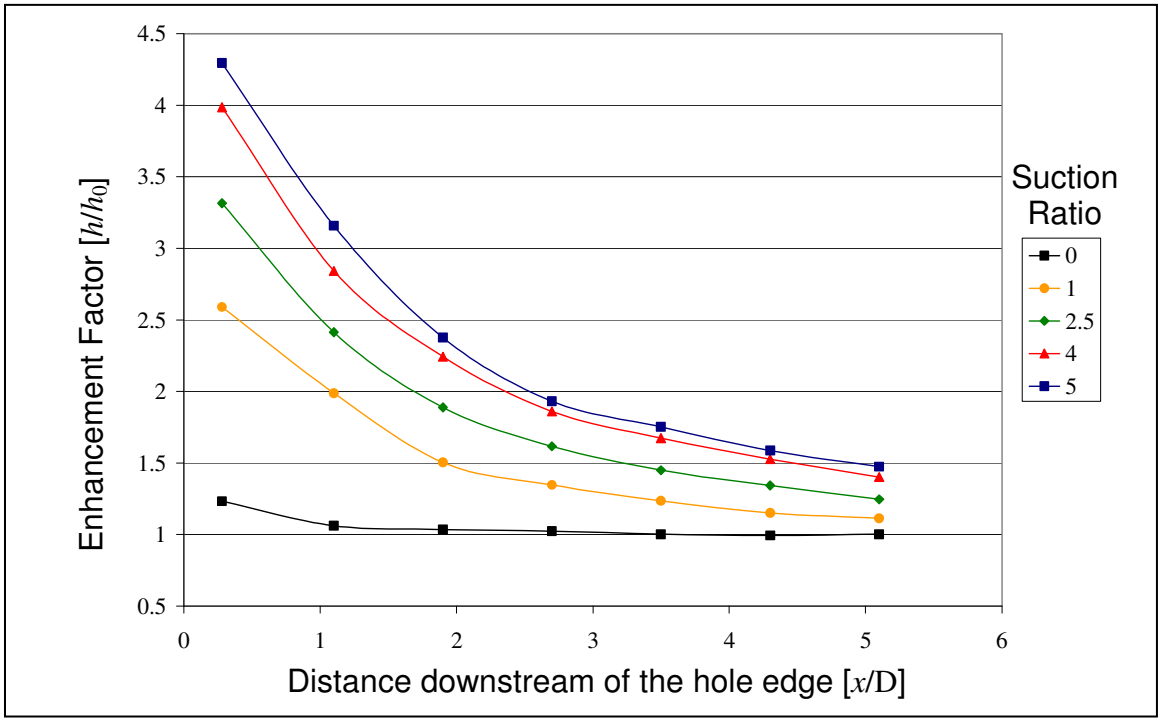

FIGURE 5.5: *Line averaged heat transfer enhancement factors downstream of the 90º extraction hole at multiple suction ratios*

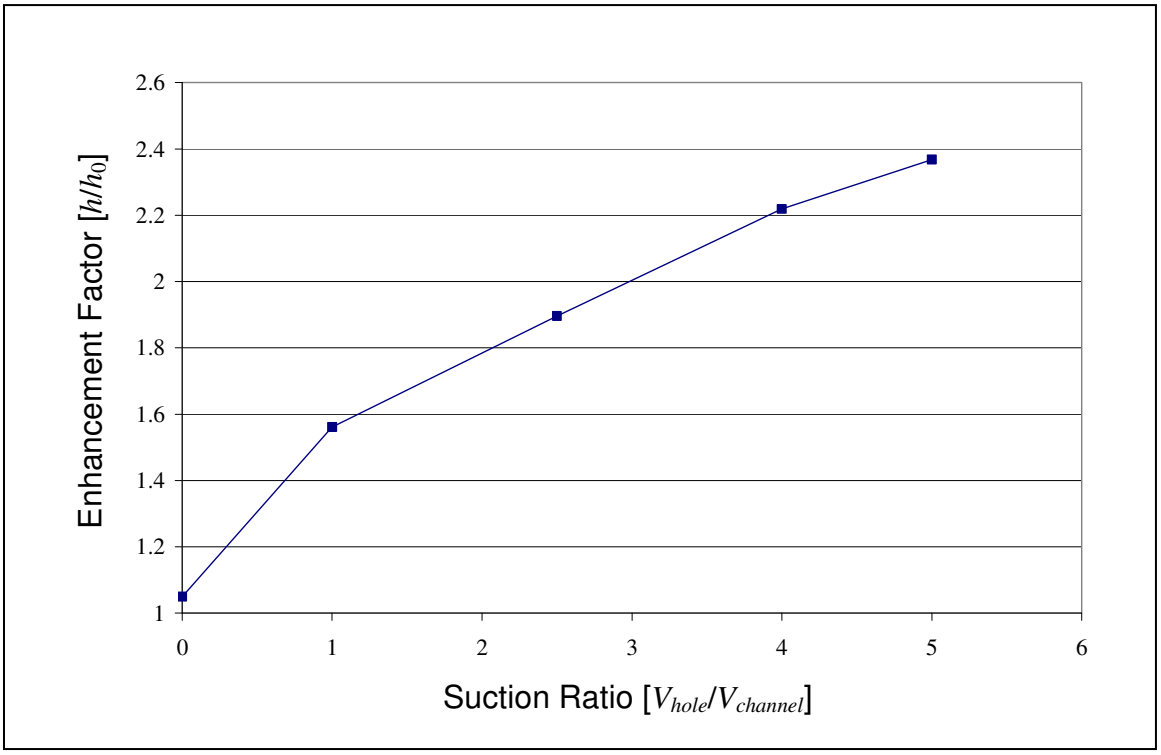

FIGURE 5.6: *Average heat transfer enhancement factors downstream of the 90º extraction hole*

5.4 INFLUENCE OF THE EXTRACTION ANGLE

To asses the influence of the angle of extraction, the line averaged enhancement downstream of the 150° extraction hole at *SR* = 5 and *SR* = 2.5 are compared with the profiles obtained with the 90º extraction hole, as shown in Figure 5.7 and Figure 5.8. Although the 150° extraction hole shows extensive augmentation, it is much less compared to the 90° extraction hole, especially at higher suction ratios. This observation correlates with the findings of Byerley [27]. The comparison shows a decrease in enhancement of approximately 45% in the near-hole region at *SR* = 5, which decreases to approximately 25% in the same region for *SR* = 2.5.

The difference in enhancement between the two extraction angles can be attributed to the amount of impingement downstream of the extraction hole, which is believed to be extensively limited by the backward slanted 150º extraction hole. This observation is further illustrated when considering that the enhancement downstream of the 150º

extraction hole is quite similar at high and moderate suction ratios in contrast to the enhancement observed with the 90º extraction hole at different suction ratios.

Further downstream ($x/D > 3$) the comparison shows a decreasing difference between the two enhancement profiles, although the difference is still significant. This can be expected since the extent of near hole impingement contributes to the amount of downwash and turbulence downstream of the extraction hole.

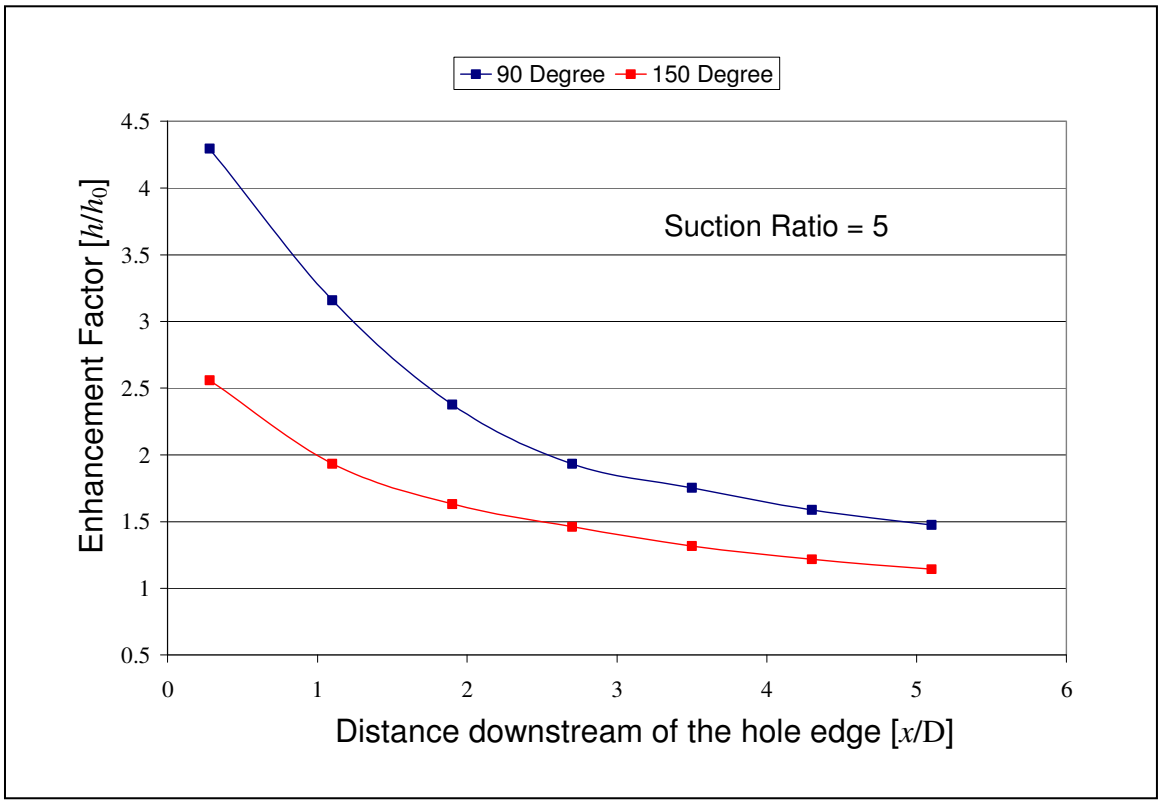

FIGURE 5.7: *Line averaged heat transfer enhancement factors downstream of the 90° and 150º extraction hole*

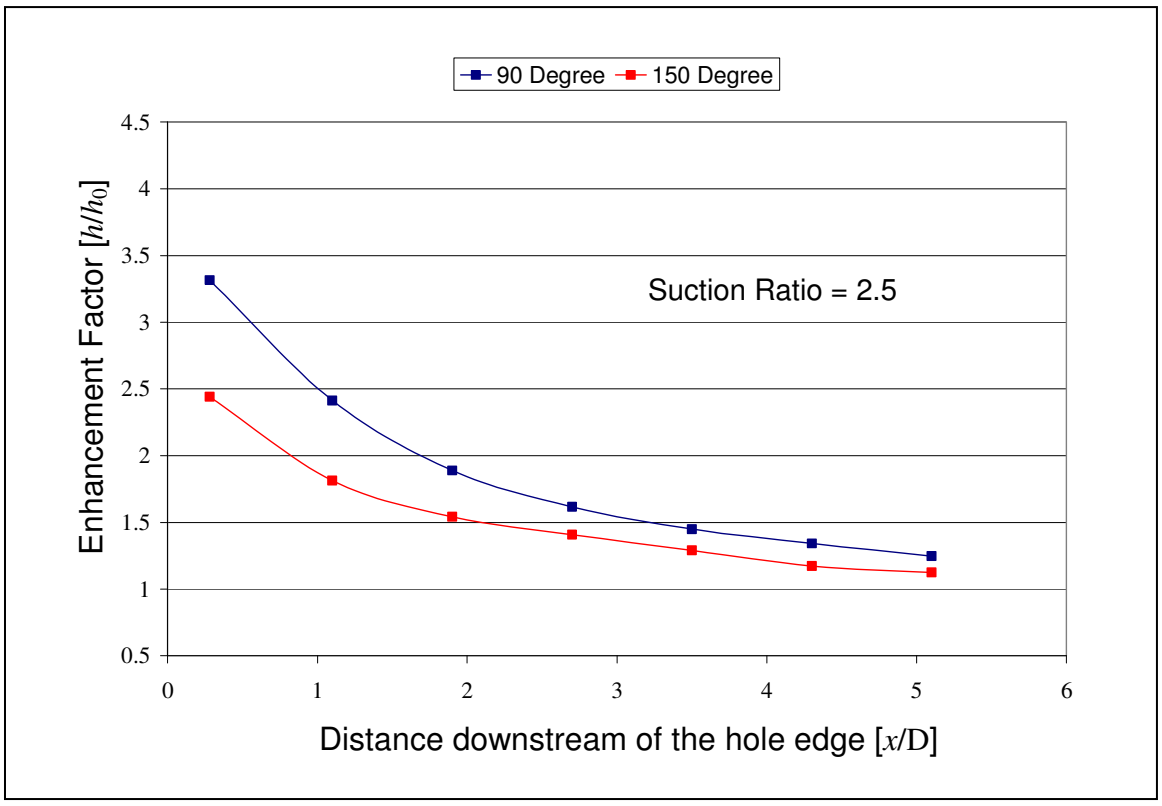

FIGURE 5.8: *Line averaged heat transfer enhancement factors downstream of the 90° and 150º extraction hole*

The enhancement profiles downstream of the 150° extraction hole at multiple suction ratios ranging from $SR = 0$ to $SR = 5$ are displayed in Figure 5.9. The enhancement profiles indicate that the amount of heat transfer enhancement reaches a stagnation point at a lower suction ratio when compared to the 90° extraction hole.

Consequently the rate of enhancement stagnation is extensively more for the slanted hole in comparison with the perpendicular hole. This is illustrated in Figure 5.10, which shows a comparison between the average enhancement factors with regard to the suction ratio for the two extraction angles. The comparison shows a difference of approximately 30% with regard to the average heat transfer enhancement value at SR =5.

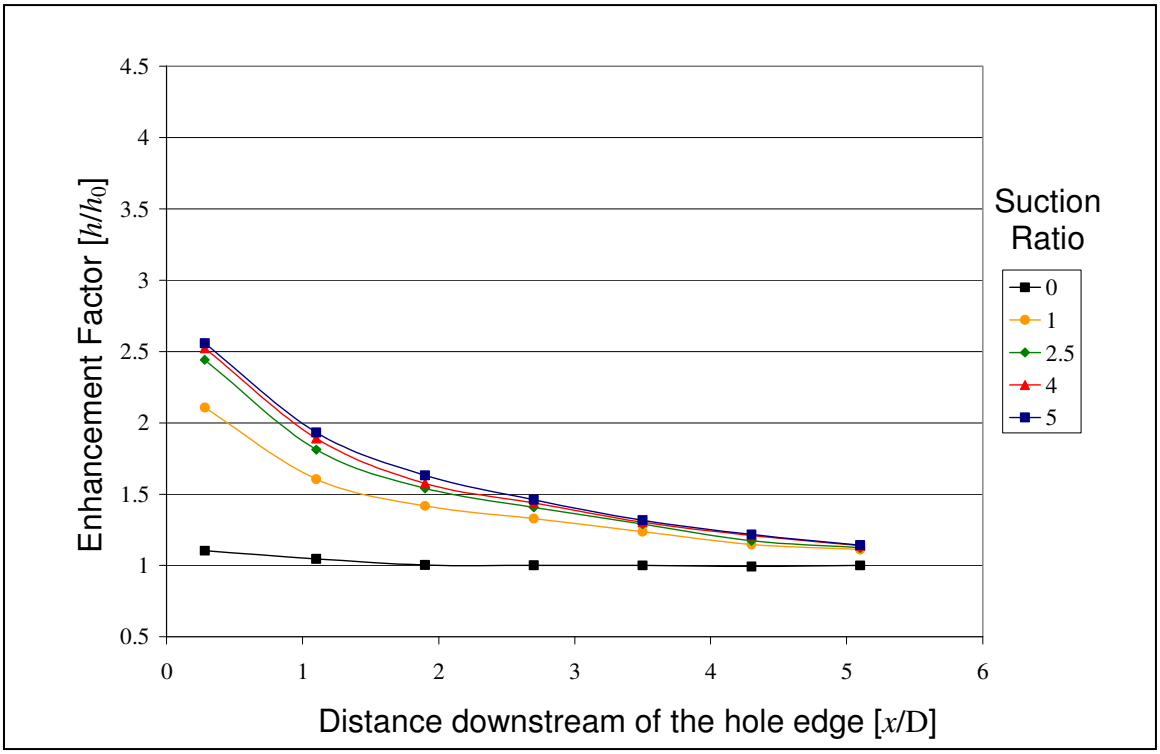

FIGURE 5.9: *Line averaged heat transfer enhancement factors downstream of the 150º extraction hole at multiple suction ratios*

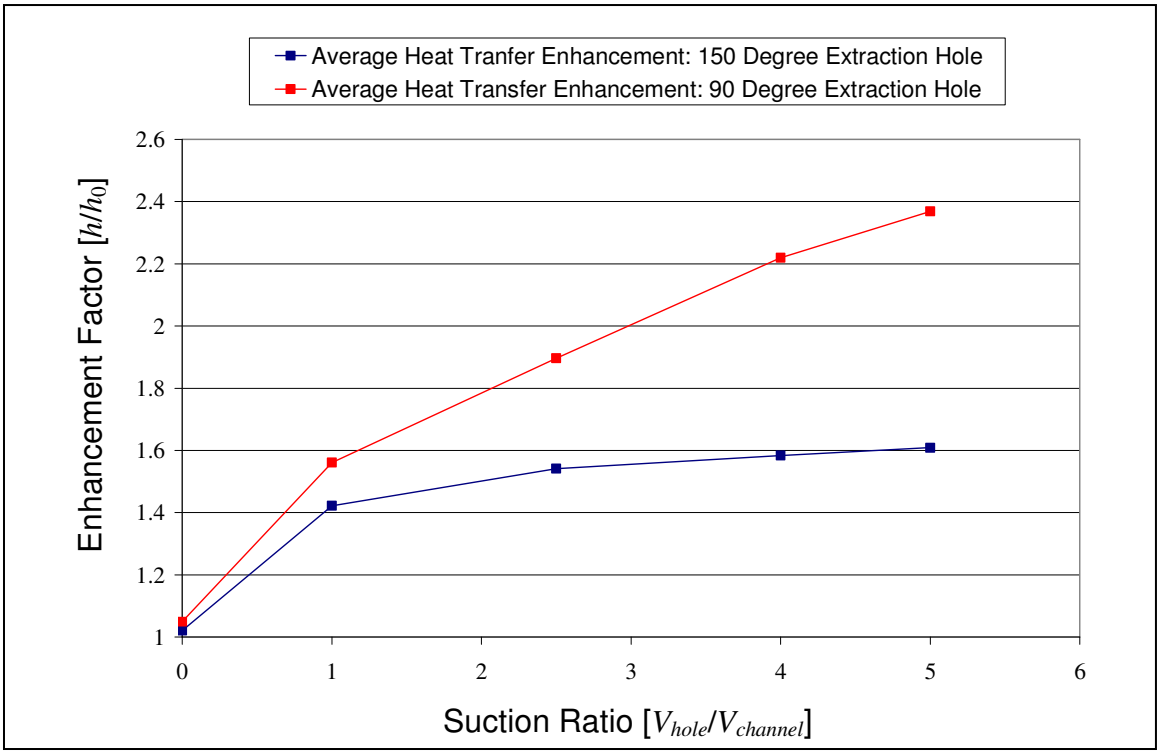

FIGURE 5.10: *Average heat transfer enhancement downstream of the 150ºand 90º extraction hole*

5.5 INFLUENCE OF THE WALL TEMPERATURE RATIO

Heat transfer enhancement at a higher $T_{wall}/T_{coolant}$ ratio was considered to further establish the sensitivity of near-hole enhancement with regard to a decreasing boundary layer density induced by the higher wall temperature. The absolute wall temperature was increased by approximately 10%, which is equal to a wall temperature increase of 30K or $T_{wall}/T_{coolant}$ ratio of 1.4. Measurements were taken at SR = 2.5 and SR = 5. It was expected that if the difference in wall temperature was to influence the amount of enhancement, the discrepancy will most likely occur in the near-hole region where impingement is the primary contributor to enhancement. The enhancement profiles downstream of the 90º extraction hole at $T_{wall}/T_{coolant}$ ratios of 1.3 and 1.4 and suction ratios of 2.5 and 5 are displayed in Figure 5.11. The profiles show good agreement at the both suction ratios, although a small difference is present near the edge of the hole (x/D < 2) at the higher suction ratio. This difference is less than 2% and indicates that the effect of a varied $T_{wall}/T_{coolant}$ ratio on the downstream enhancement is of a second order and can therefore be considered negligible within the chosen experimental domain.

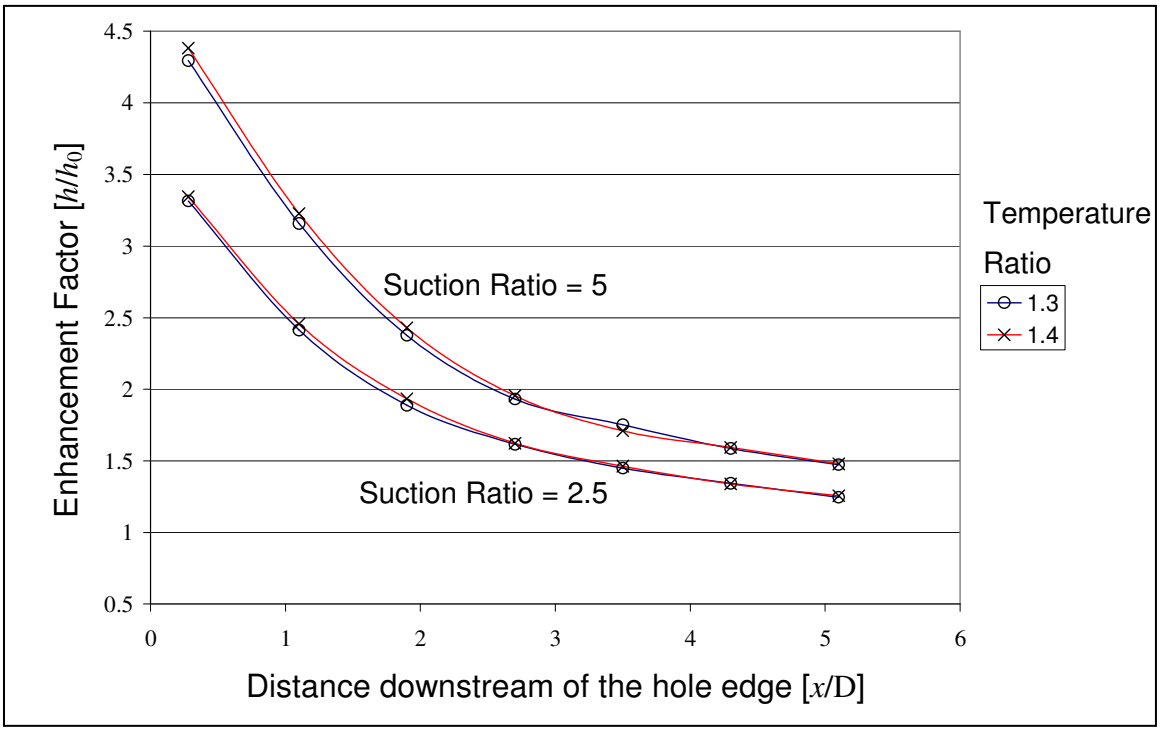

FIGURE 5.11: *Line averaged heat transfer enhancement factors downstream of the 90º extraction hole at $T_{wall}/T_{coolant}$ ratios of 1.3 and 1.4 and suction ratios of 2.5 and 5*

5.6 NUMERICAL HEAT TRANSFER PREDICTIONS

Numerical methods have developed to the extent that it is routinely employed as a design and analysis tool. The primary focus of this study was on obtaining experimental measurements of various parameters that influence near-hole heat transfer augmentation. However, it was also decided to assess the ability of numerical methods to predict the measured results. The numerical heat transfer results were obtained by making use of the k-ω turbulence model with the implementation of wall functions to solve the boundary layer flow field. The numerical heat transfer results were non-dimensionalised in the same manner as the experimental data.

A comparison between the numerically predicted and experimentally measured line averaged heat transfer enhancement downstream of the 90° extraction hole at SR = 5 and SR = 2.5 is displayed in Figure 5.12 and Figure 5.13. The numerical results show a tendency to under predict the heat transfer induced by impingement directly downstream of the coolant extraction hole and to over predict the extent of vortex downwash further downstream. The augmentation directly downstream of the coolant extraction hole is numerically under predicted by approximately 20 % at a higher suction ratio of 5 and by approximately 30 % at a moderate suction ratio of 2.5.

The ability of the numerical code to predict enhancement more accurately at higher suction ratios can be expected, since the amount of enhancement at higher suction ratios is more dependant on the impingement of the mainstream flow and to a lesser extent on boundary layer renewal (keeping in mind that the numerical model made use of wall functions to model the fluid boundary layer).

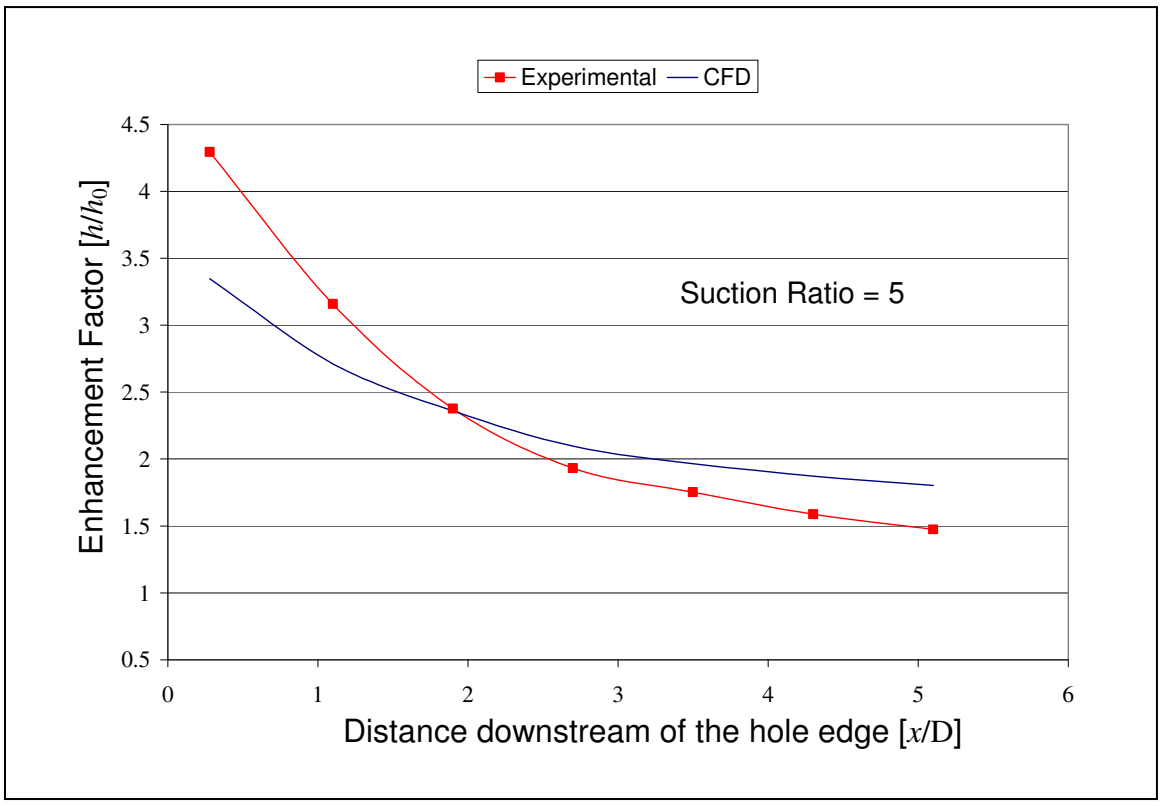

FIGURE 5.12: *Comparison between the numerically predicted and experimentally measured enhancement downstream of the 90º extraction hole*

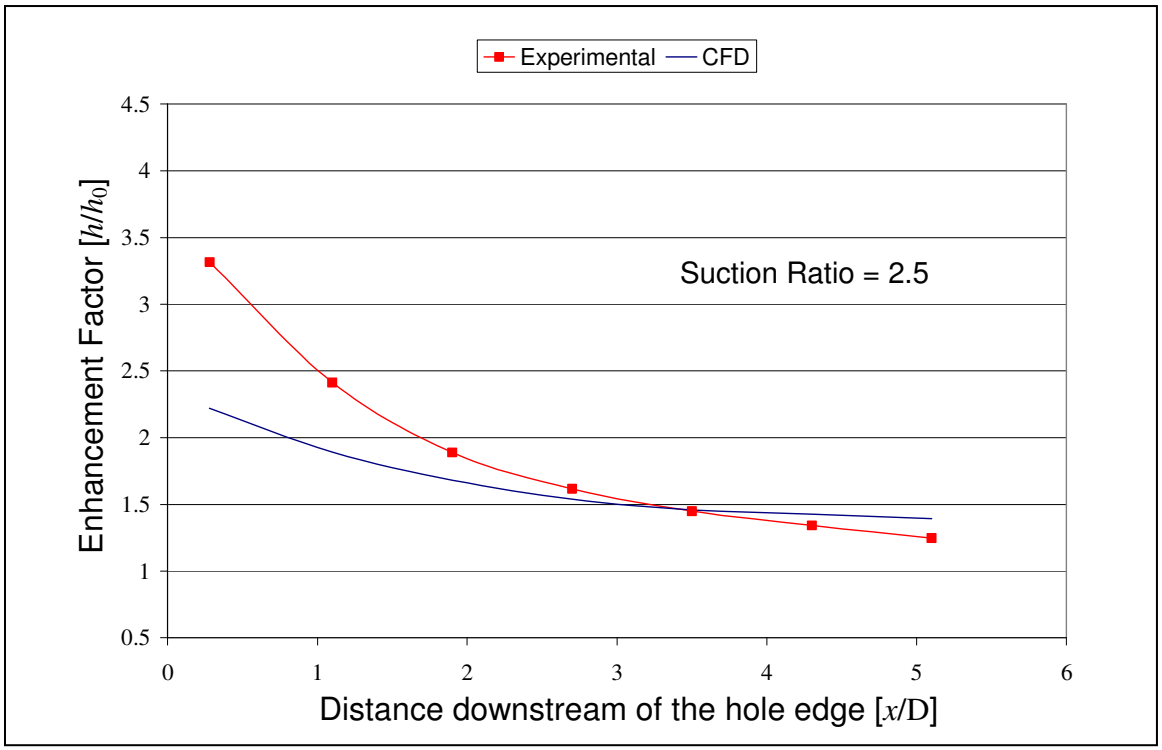

FIGURE 5.13: *Comparison between the numerically predicted and experimentally measured enhancement downstream of the 90º extraction hole*

This observation is further illustrated in Figure 5.14 and Figure 5.15 which is a comparison between the numerically predicted centre-line heat transfer enhancement and the experimentally measured centre-line heat transfer profiles obtained from the experimental results published by Byerley [27]. The centre-line profile is a local measurement across the median of impingement (the point of maximum enhancement), which provides a more prudent indication of the ability of the numerical code to predict the near-hole augmentation.

The numerical centre-line results show a reasonable accuracy in predicting the near-hole enhancement at SR = 5, with a discrepancy of less than 20%. This amount of divergence is similar to the line averaged results at the same suction ratio. At SR = 2.5 the centre-line heat transfer is extensively under predicted by approximately 50 %. This comparison indicates that the numerical model predicts enhancement where impingement is more dominant (i.e. SR > 3) better than when boundary layer renewal is the principal means of augmentation (i.e. SR < 3).

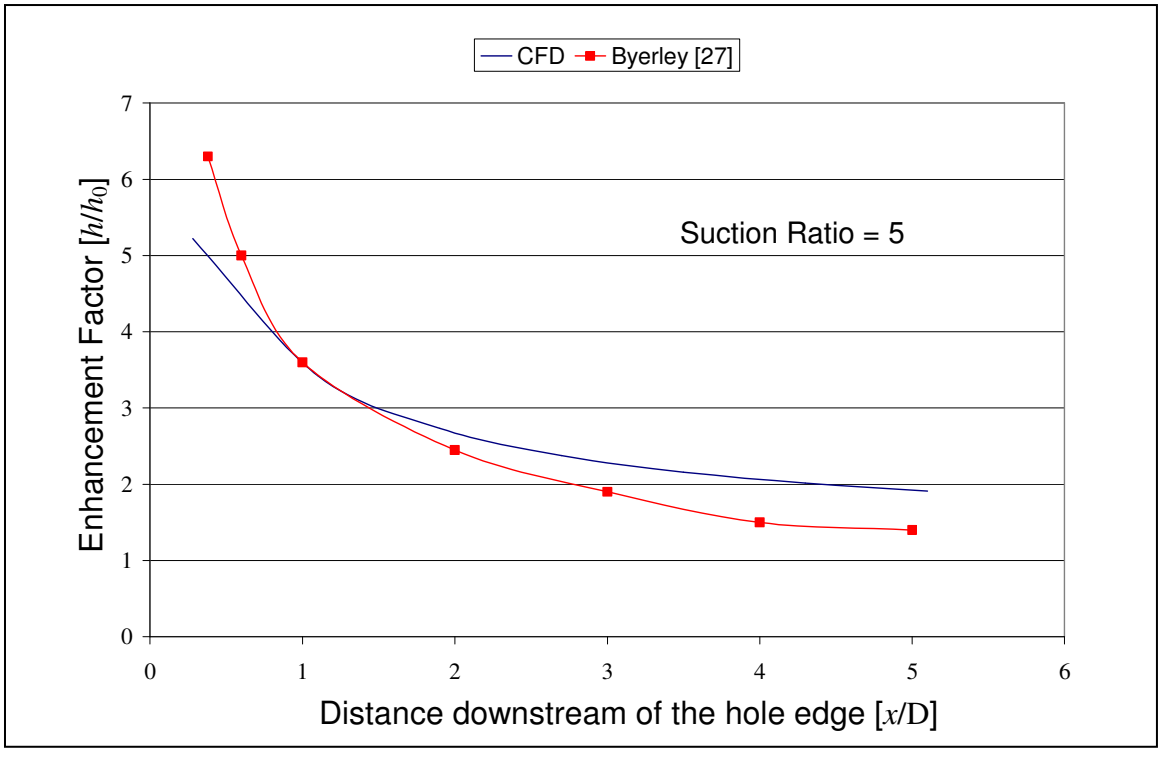

FIGURE 5.14: *Centre-line heat transfer enhancement factors downstream of the 90º extraction hole*

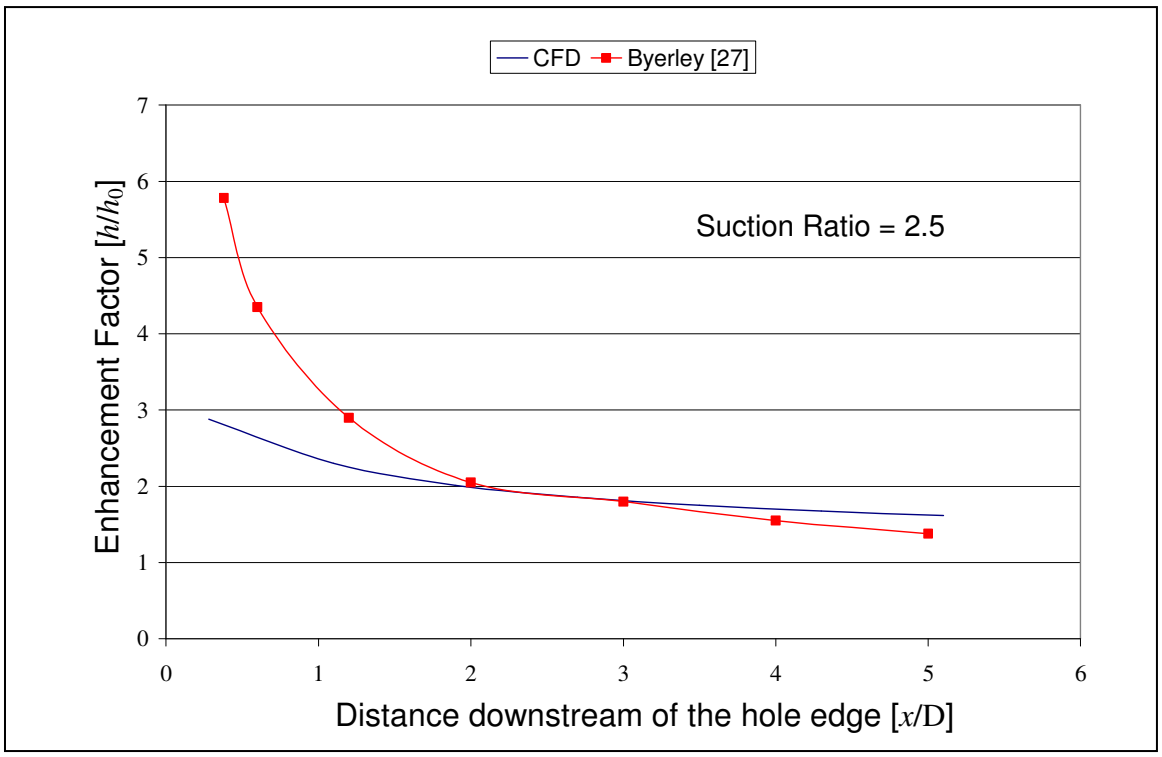

FIGURE 5.15: *Centre-line heat transfer enhancement factors downstream of the 90º extraction hole*

The same pattern is observed when considering the enhancement profiles for the 150º extraction hole, where it is believed that augmentation is primarily induced by boundary layer renewal at moderate and high suction ratios. Figure 5.16 and Figure 5.17 present a comparison between the line averaged heat transfer enhancement downstream of the 150° coolant extraction hole and the experimental results.

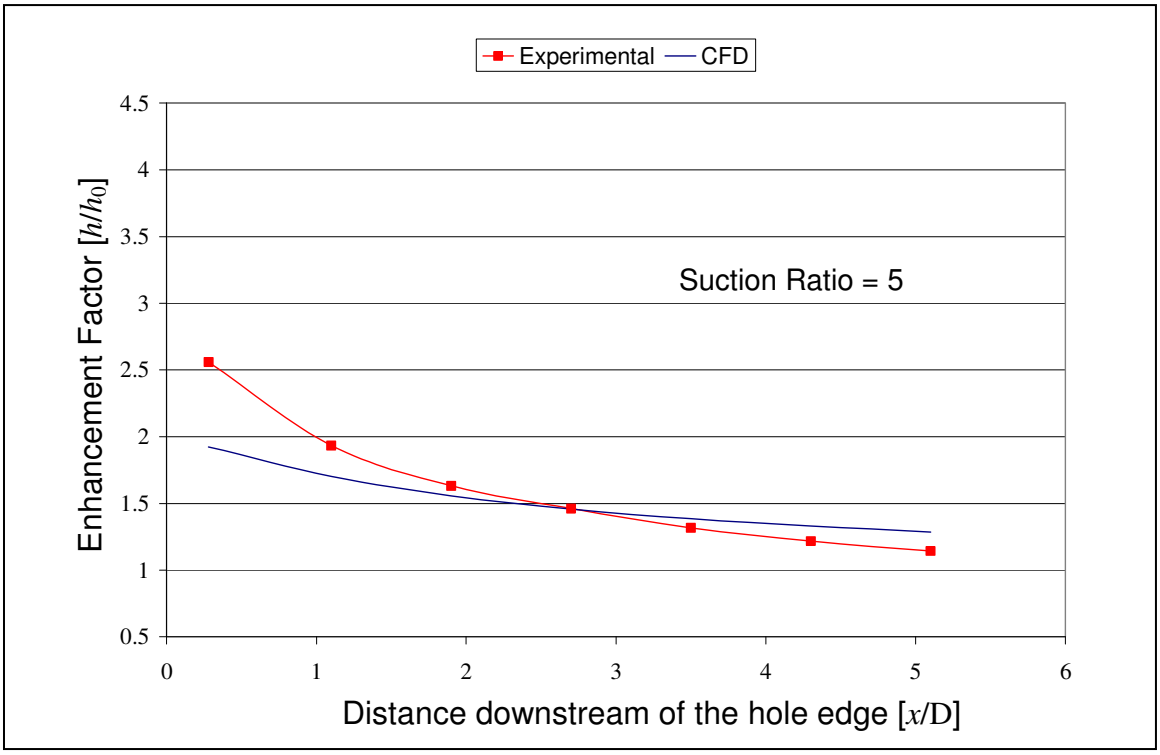

FIGURE 5.16: *Comparison between the numerically predicted and experimentally measured enhancement downstream of the 150º extraction hole*

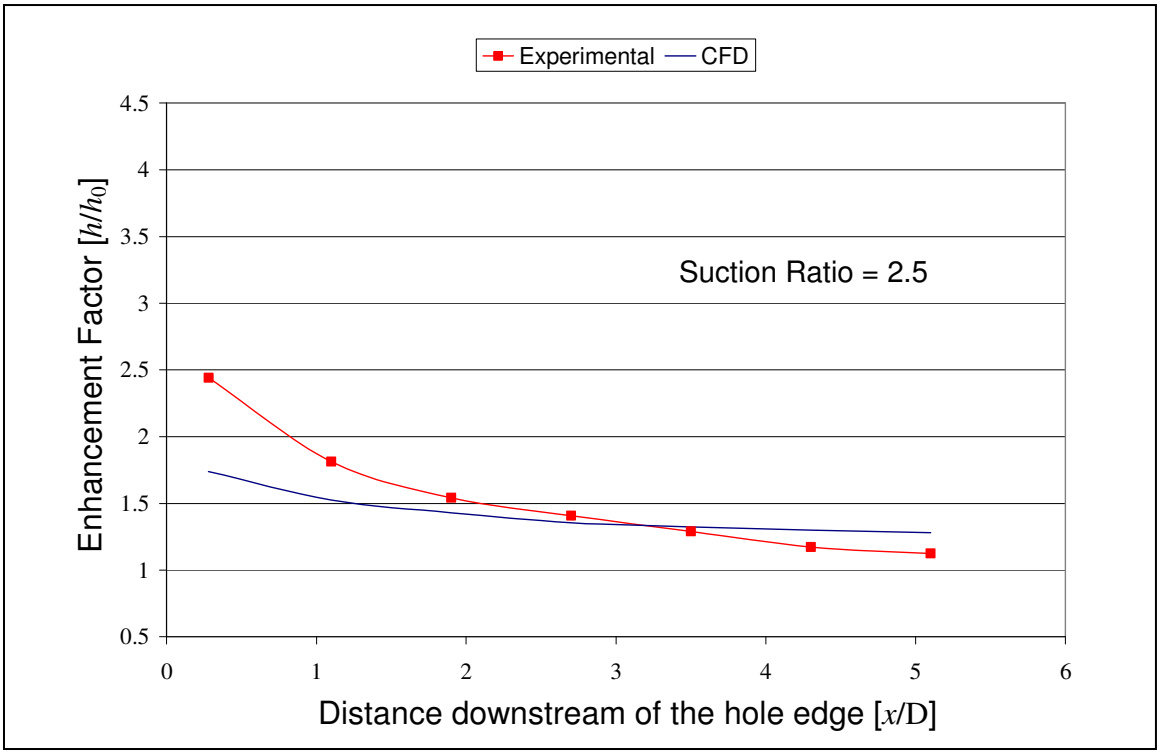

FIGURE 5.17: *Comparison between the numerically predicted and experimentally measured enhancement downstream of the 150º extraction hole*

Numerically predicted velocity vectors in the near-hole region of the 90º extraction hole at a suction ratio of 5 and 2.5 are displayed in Figure 5.18 and Figure 5.19. The encircled area shows the location of flow impingement induced by coolant extraction. When comparing the position of impingement between the two suction ratios, it should be noted that the point of impingement moves further downstream (a distance of approximately 0.5*D*) and that flow reversal takes place near the hole edge at a suction ratio of 5. At the lower suction ratio the point of impingement is on the edge of the extraction hole.

This observation relates strongly with the findings of Byerley [27], who conducted smoke visualization studies in the near-hole region of a 90º extraction hole. Furthermore, it indicates that although the current numerical model provided poor quantitative agreement with the experimental heat transfer results, it showed qualitative agreement with regard to predicting the near-hole flow field.

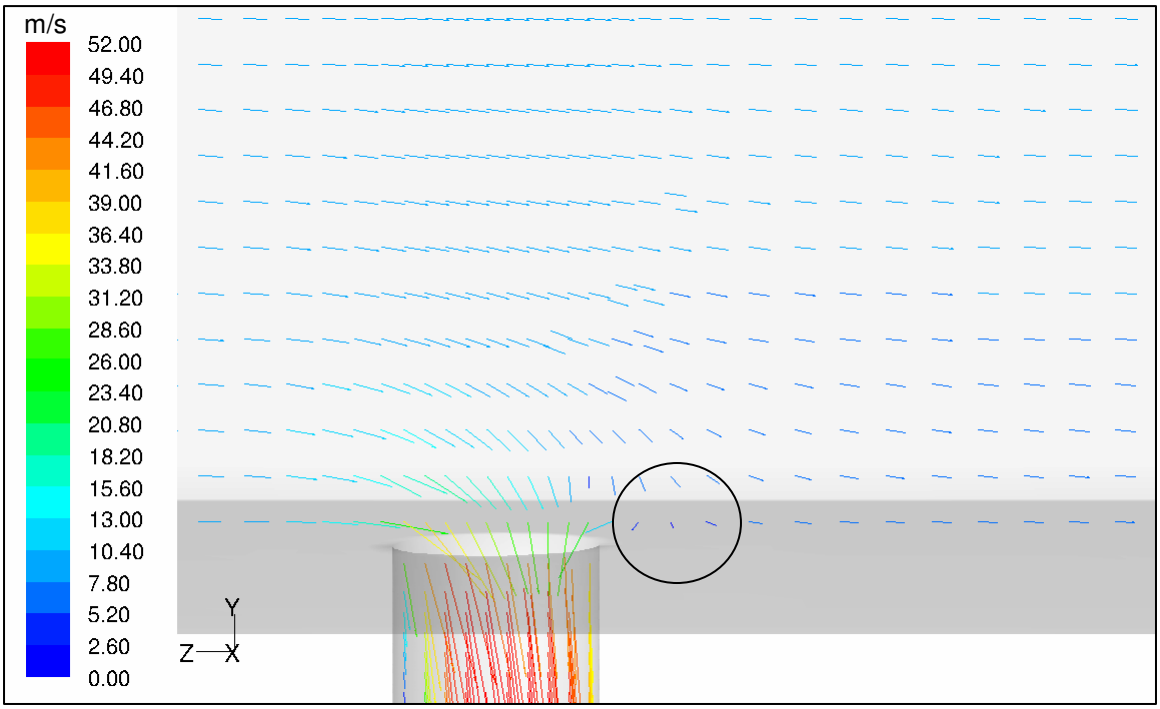

FIGURE 5.18: *Velocity vectors near the entrance to the 90° extraction hole at a SR = 5 (Encircled area indicates coolant impingement)*

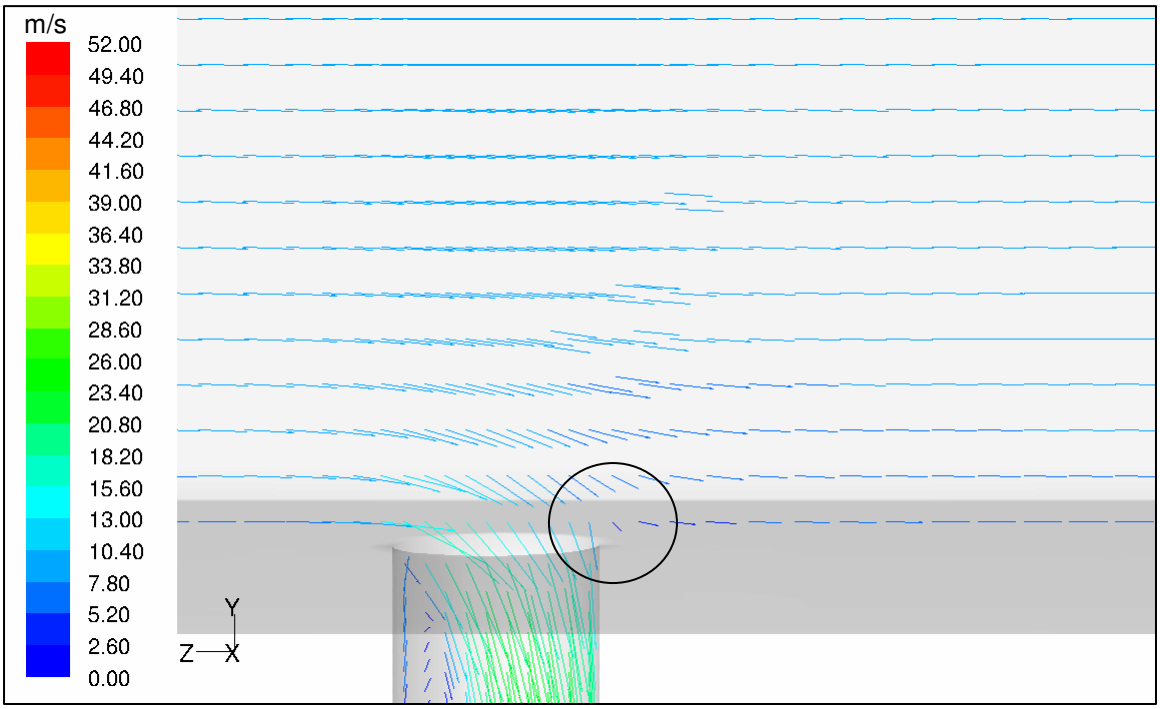

FIGURE 5.19: *Velocity vectors near the entrance to the 90° extraction hole at a SR = 2.5 (Encircled area indicates coolant impingement)*

Velocity vectors near the entrance of the 150º hole at suction ratios of 5 and 2.5 are displayed in Figure 5.20 and Figure 5.21. The velocity vectors of the 150° hole indicate that the impingement area is situated inside the extraction channel at both moderate and higher suction ratios and not downstream as is the case with the perpendicular hole. This confirms that heat transfer augmentation downstream of the 150° extraction hole is to a lesser extent dependant on coolant impingement and to a greater extent on boundary layer renewal. Therefore the heat transfer augmentation downstream of the 150° extraction hole is extensively lower and reaches a stagnation point, regarding enhancement, at a lower suction ratio when compared to the 90° extraction hole. Furthermore the comparison between Figure 5.20 and Figure 5.21 indicate an increased amount of recirculation within the cooling passage in comparison with the 90° extraction hole.

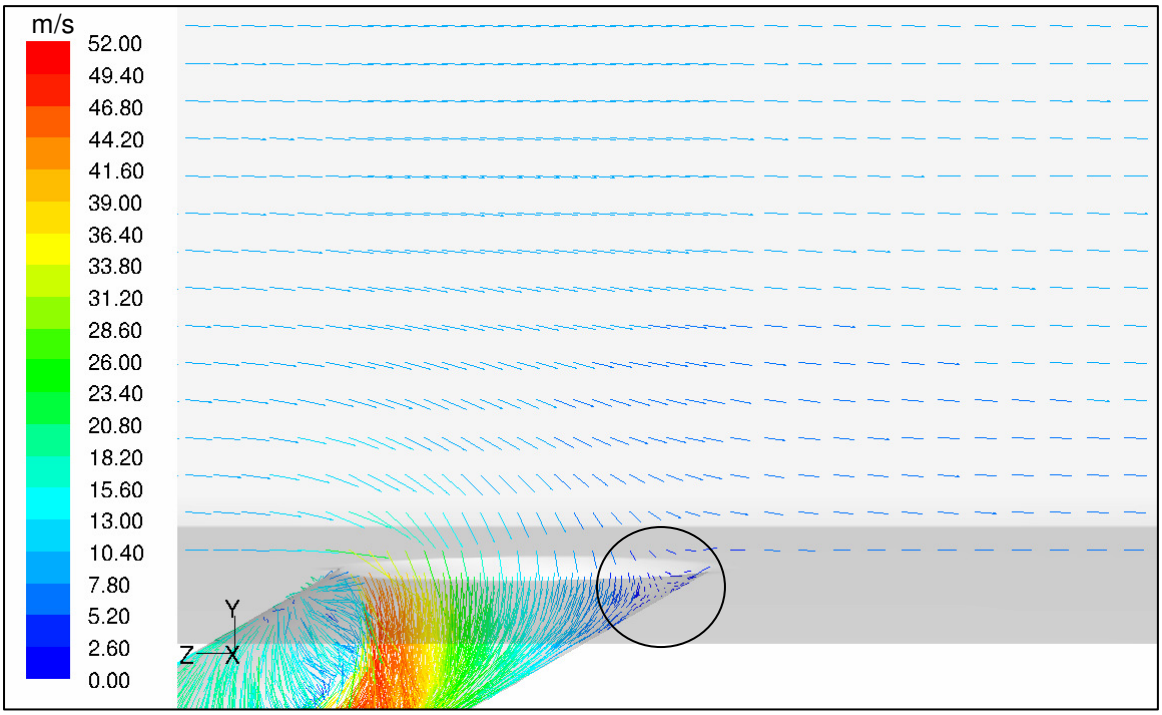

FIGURE 5.20: *Velocity vectors near the entrance to the 150° extraction hole at a SR = 5 (Encircled area indicates coolant impingement)*

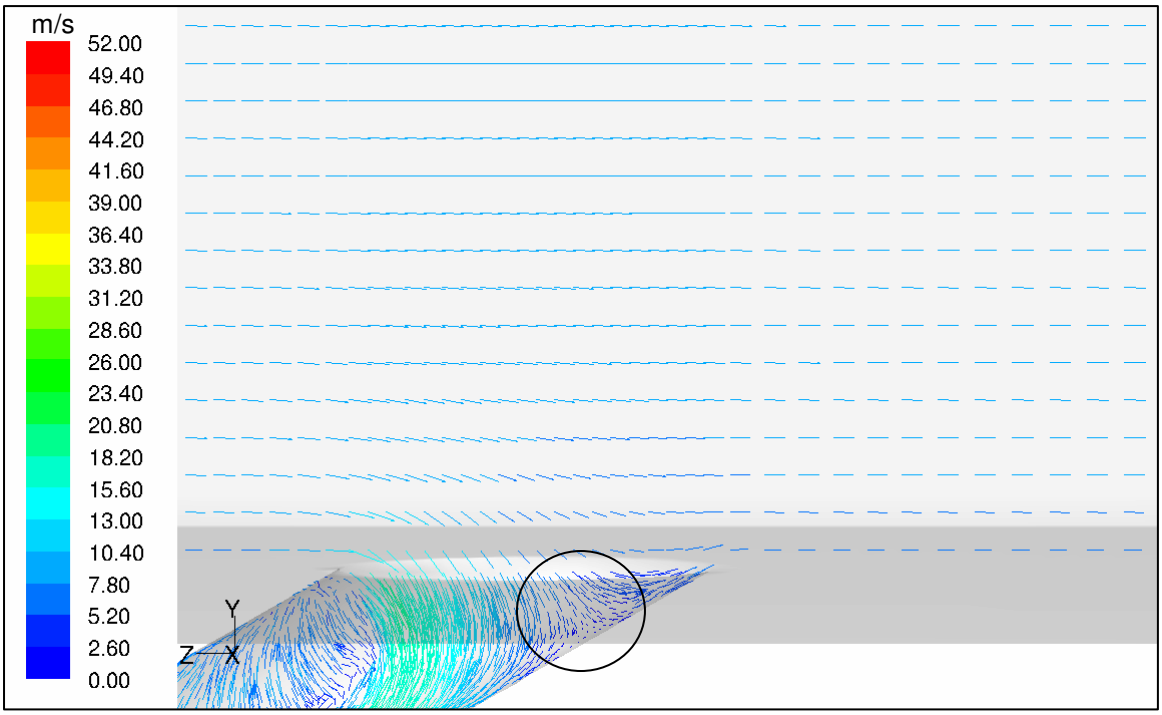

FIGURE 5.21: *Velocity vectors near the entrance to the 150° extraction hole at a SR = 2.5 (Encircled area indicates coolant impingement)*

The numerical results showed that the numerical model predicated the heat transfer enhancement downstream of the coolant extraction hole more accurately at higher suction ratios. The numerical model made use of a wall function approach to calculate the boundary layer flow field, which implies that the near-wall boundary layer was not discretized. It is believed that better agreement was obtained at higher suction ratios since the near-hole enhancement is induced primarily by impingement of the mainstream flow, and to a lesser extent by boundary layer renewal. For this reason the numerical model of the 90º extraction hole at a SR = 5 was used as a case study to compare different turbulence models. The turbulence models which were considered include the k-ω and k-ω SST model, which are two-equation RANS models, the RSM model, which is a seven equation RANS model, and the DES model. The DES model implements the Spalart-Allmaras one-equation RANS model in the boundary layer and the LES model in the mainstream.

The enhancement predicted by the various turbulence models are presented in Figure 5.22. The predicted values are compared with the experimentally measured values for the 90° extraction hole at SR = 5. The k-ω SST and RSM turbulence models show a tendency to under predict the impingement in the near-hole region. These two models do however predict the heat transfer enhancement further downstream better than the k-ω model.

The DES turbulence model predicts the amount of near-hole enhancement quite accurately, but over predicts the size of the impingement area. Although the DES model is not a recommended turbulence model for internal flow field solutions it must be noted that the DES model was implemented outside the boundary layer. Implementation of the DES turbulence model within the boundary layer, which implies lesser dependence of the model on a RANS based turbulence model in the boundary layer, may improve the ability to predict the downstream heat transfer enhancement. Therefore it is recommended that an LES based turbulence model rather be used along with a finer grid, to solve the boundary layer in detail and more accurately capture the flow interaction.

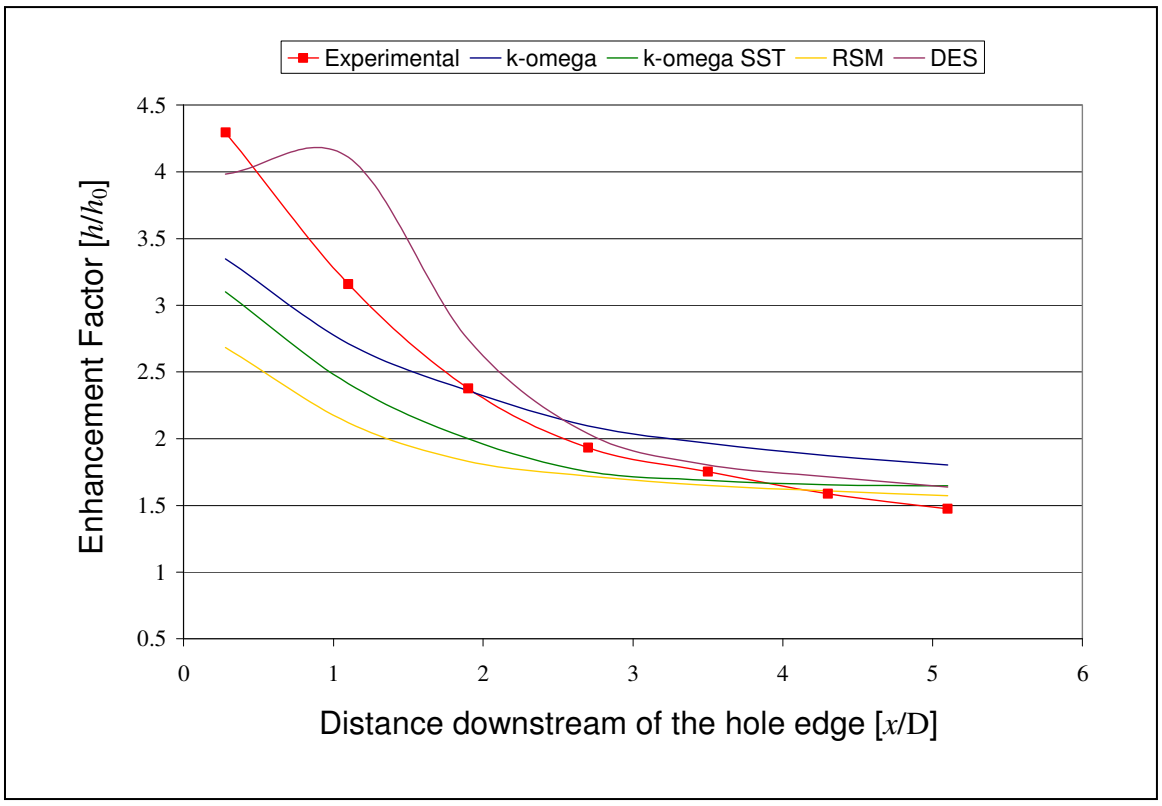

FIGURE 5.22: *Comparison between the experimentally measured and numerically predicted heat transfer enhancement downstream of the 90º extraction hole*

5.7 CONCLUSION

In the current chapter the experimental and numerical results obtained in the study were presented. A comparison between the measured results with that obtained from a previously published study showed good overall agreement. Considering that different measuring techniques were implemented, indicates that the experimental method implemented in the current study is valid.

Furthermore the results were compared at different suction ratios and extraction angles. The comparison showed that the amount of coolant extraction has a considerable influence on the local heat transfer augmentation, and that the amount of local enhancement is primarily dependant on the suction ratio and extraction angle. This observation correlates well with relating studies.

A comparison was made between the numerically predicted enhancement and the experimentally measured values. The numerical model indicated that the implementation of a wall function approach was unable to accurately predict the amount of downstream augmentation. The numerical model did however show the ability to predict the heat transfer enhancement more accurately at higher suction ratios, where the impingement of the mainstream flow is more dominant. The chapter concluded with a comparison between different turbulence models.

CHAPTER 6
CONCLUSION & RECOMMENDATIONS

6.1 PREAMBLE

In the current study the heat transfer augmentation near the entrance to a coolant extraction hole was studied experimentally as well as using numerical methods. A comprehensive literature study indicated that a limited amount of research has been done in this area. Furthermore, relating studies showed that boundary layer renewal and coolant impingement, induced by the extraction of coolant, contributes to extensive heat transfer augmentation downstream of the coolant extraction hole. From the reviewed literature the following uncertainties were identified:

I. The influence of an inverse boundary layer density on the near-hole enhancement or augmentation footprint.

II. The influence of the channel sidewalls on the downstream heat transfer enhancement.

III. The influence of different suction ratios, extraction angles and higher wall-to-coolant temperature ratios on the augmented heat transfer.

The objective of the current study was to contribute to the work which was done in this area by considering the above mentioned uncertainties.

After a review of different experimental heat transfer measurement techniques, thin-film heat flux gauges combined with a numerical technique, based on the resolution of the unsteady conduction equation, was adopted for the experimental investigation. A

single pass square channel, resembling an internal cooling channel, with a coolant extraction hole was designed, built and validated against analytically estimated values as well as experimental results published in the open literature.

Experimental measurements were obtained at different extraction parameters to determine the uncertainties stipulated in the study proposal. These parameters were:

I. Suction ratios ranging between 0 and 5

II. Coolant extraction angles of 90° and 150°

III. Wall-to-coolant temperature ratios of 1.3 and 1.4

Furthermore, a commercial finite volume code was used to numerically simulate the experimental domain. The aim of the numerical investigation was to provide more detail regarding the near-hole flow patterns and thermal interaction. Additionally, to provide an indication of the degree of accuracy with which a wall function approach can predict the heat transfer augmentation induced by coolant extraction.

6.2 CONCLUSION

Initially, the experimental setup was calibrated against previously published results from Byerley [27]. Contrary to the experimental setup of Byerley [27] cooled air was blown through a heated channel wall. Furthermore, use was made of platinum thin-film heat flux gauges, as opposed to liquid crystal thermography to measure the thermal enhancement. Despite these differences, good overall agreement was obtained between the experimental results.

The experimental investigation showed that the primary variables that influenced the heat transfer augmentation constitute the suction ratio and extraction angle of the film-cooling hole. The 90º extraction hole showed significant augmentation in near-hole region with

regard to an increasing suction ratio. The net amount of enhancement appeared to stagnate with an increasing amount of coolant extraction.

Although the 150° extraction hole also showed extensive near-hole augmentation, it was comprehensively lower compared to the 90° extraction hole, especially at higher suction ratios. This observation correlates with the findings of Byerley [27]. The comparison shows a decrease in enhancement of approximately 45% in the near-hole region at $SR = 5$, which decreases to approximately 25% in the same region for $SR = 2.5$. It is believed that this reduction in enhancement can be attributed to the higher angle of coolant deviation, which may limit the amount of downstream impingement.

The good agreement which was obtained further downstream of the extraction hole with the results presented by Byerley [27], indicates that the channel width has a negligible influence on the heat transfer augmentation induced by coolant extraction. In this study a square channel was used as apposed to the study conducted by Byerley [27] which widened the channel to exclude any wall effects.

The enhancement which was obtained at a higher $T_{wall}/T_{coolant}$ ratio showed a difference of less than 2% in the near-hole region. This indicates that this variable which was considered does not primarily influence heat transfer augmentation and can therefore be considered to be negligible within the chosen experimental conditions.

The numerical model showed that although it is capable of predicting the overall trend, the magnitude of average near-hole enhancement was underpredicted by approximately 30%. At higher suction ratios, where the impingement of the mainstream flow is more dominant, the numerical model showed better agreement. The difference between the numerically predicted heat transfer enhancement and the experimental measurements can primarily be attributed to the inability of the wall function approach used to resolve the boundary layer.

Qualitatively the numerical model predicted the near-hole flow field considerably well. The numerical model correlated with a published flow visualization study in predicting the position of impingement downstream of a perpendicular hole. Furthermore, it showed that the area of impingement, in a backward slanted hole, is situated inside the extraction channel at both moderate and higher suction ratios and not downstream as is the case with the perpendicular hole. This confirms that the enhancement downstream of the backward angled extraction hole is primarily induced by boundary layer renewal and to a lesser extent by impingement.

6.3 RECOMMENDATIONS

Although the experimental results obtained in the current study compared adequately with previously published data, the following recommendations can be made to improve the overall study:

I. Implementation of an exponential numerical scheme

The experimental study confirmed that a numerical heat flux measurement technique can successfully be implemented as an alternative with regard to the analogue measurement technique. In the current study the numerical scheme, which converted surface temperature readings into a heat flux, was coded in a script based language. It is recommended that this should rather be coded in a compilable language to reduce the computational time to obtain a converged solution. As an alternative to the Crank-Nicholson scheme it is also recommended that an exponential scheme, described by Patankar et al. [81], be implemented. According to Patankar et al. [66] this scheme is not as sensitive to the time step size as the Crank-Nicholson scheme used in the current study.

II. Gauge construction

The platinum thin-film gauges used in the study were painted onto the ceramic substrate according to VKI specifications [50]. Although these gauges proved to be adequate it is recommended that an evaporation technique should rather be used to apply the platinum to the ceramic substrate. This will provide the ability to manufacture smaller gauges and will also ensure a more evenly distribution of the platinum film.

III. Numerical modelling

The numerical study compared different turbulence models with the experimental results for a perpendicular hole at a maximum suction ratio of 5. The RANS based models showed a moderate agreement regarding the prediction of the heat transfer enhancement profile downstream of the extraction hole. Under prediction of the heat transfer enhancement induced by impingement near the hole edge was noted with all the RANS based models. The DES turbulence model accurately predicted the maximum amount of heat transfer enhancement, but extensively over predicted the impingement region downstream of the extraction hole. It is therefore recommended that an LES turbulence model should rather be implemented using a finer grid.

REFERENCES:

[1] Cumpsty, N., 2000, *Jet Propulsion: A Simple Guide to the Aerodynamic and Thermodynamic Design and Performance of Jet Engines*, Cambridge University Press, Cambridge.

[2] Saravanamuttoo, H.I.H., Rogers, G.F.C., Cohen, H., 2001, *Gas Turbine Theory*, 5th Edition, Prentice Hall, New Jersey

[3] Han, J.C., Zhang Y.M., Lee C.P., 1994, "Influence of Surface Heating Condition on Local Heat Transfer in a Rotating Square Channel with Smooth Walls and Radial Outward Flow", *ASME Journal of Turbomachinery*, Vol. 116, No.1, pp.149-158.

[4] Clifford, R.J., 1985, "Rotating Heat Transfer Investigations on a Multipass Cooling Geometry", *AGARD Conference Proceedings*, No.390: Heat Transfer and Cooling in Gas Turbines, May 6-10.

[5] Smout, P.D., Chew, J.D., Childs, P.R.N., 2002, "ICAS-GT: A European Collaborative Research Programme on Internal Cooling Air Systems for Gas Turbines", *ASME Turbo Expo*, Amsterdam, Netherlands, June 3-6, ASME Paper No. GT-2002-30479.

[6] Han, J.C., Dutta, S., Ekkad, V., 2000, *Gas Turbine Heat Transfer and Cooling Technology*, Taylor & Francis, New York.

[7] Dunn, M.G., 2001, "Convective Heat Transfer and Aerodynamics in Axial Flow Turbines", *ASME Turbo Expo*, New Orleans, USA, June 4-7, ASME Paper No. 2001-GT-0506.

[8] Chyu, M.K., 1990, "Heat Transfer and Pressure Drop for Short Pin-Fin Arrays with Pin-Endwall Fillets", *ASME Journal of Heat Transfer*, Vol. 112, pp. 926-932.

[9] Goldstein, R.J., Jabbari, M.Y., Chen, S.B., 1994, "Convective Mass Transfer and Pressure Loss Characteristics of Staggered Short Pin-Fin Arrays", *International Journal of Heat and Mass Transfer*, Vol. 37, pp. 149-160.

[10] Olson, D.A., 1992, "Heat Transfer in Thin, Compact Heat Exchangers with Circular, Rectangular, or Pin-Fin Flow Passages", *ASME Journal of Heat Transfer*, Vol.114, pp.373-382.

[11] Metzger, D.E., Fan, S.C., Haley, S.W., 1984, "Effects of Pin Shape and Array Orientation on Heat transfer and Pressure Loss in Pin Fin Arrays", *ASME Journal of Engineering for Gas Turbine and Power*, Vol.106, pp.252-257.

[12] Metzger, D.E., Shephard, W.B., Haley, S.W., 1986, "Row Resolved Heat Transfer Variations in Pin-Fin Arrays Including Effects of Non-Uniform Arrays and Flow Convergence", *ASME International Gas Turbine Conference and Exhibit*, Dusseldorf, West-Germany, June 8-12, ASME Paper No. 86-GT-132

[13] Arora, S.C., Abdel-Messeh, W., 1989, "Characteristics of Partial Length Circular Pin Fins as Heat Transfer Augmentors for Airfoil Internal Cooling Passages", *ASME Gas Turbine and Aero Engine Congress and Exposition*, Toronto, Ontario, Canada, June 4-8, ASME Paper No. 89-GT-87.

[14] Johnson, B.V., Wagner, J.H., Steuber, G.D., Yeh, F.C., 1994 (a), "Heat Transfer in Rotating Serpentine Passages with Trips Skewed to the Flow", *ASME Journal of Turbomachinery*, Vol.116, pp.113-123.

[15] Johnson, B.V., Wagner, J.H., Steuber, G.D., Yeh, F.C., 1994 (b), "Heat Transfer in Rotating Serpentine Passages with Selected Model Orientations for Smooth or Skewed Trip Walls", *ASME Journal of Turbomachinery*, Vol.116, pp.738-744.

[16] Han, J.C., Zhang, Y.M., Kalkheuhler, K., 1993, "Uneven Temperature Effects on Local Heat Transfer in a Rotating Two-Pass Square Channel with Smooth Walls", *ASME Journal of Heat Transfer*, Vol.114, pp.850-858.

[17] Han, J.C., Zhang, Y.M., 1992, "High Performance Heat Transfer Ducts with Parallel Broken and V-Shaped Broken Ribs", *International Journal of Heat and Mass Transfer*, Vol. 35, No.2, pp.513-523.

[18] Han, J.C., 2004, "Recent Studies in Turbine Blade Cooling", *International Journal of Rotating Machinery*, Vol.10, No.6, pp.443-457.

[19] Han, J.C., Dutta, S., 1995, *Heat Transfer and Cooling in Gas Turbines*, VKI Lecture Series 1995-05, Von Karman Institute for Fluid Dynamics, Brussels, Belgium.

[20] Taylor, J.R., 1980, "Heat Transfer Phenomena in Gas Turbines", *ASME Gas Turbine Conference and Products Show*, New Orleans, USA, March 10-13, ASME Paper No. 80-GT-172.

[21] Florschuetz, L.W., Berry, R.A., Metzger, D.E., 1980, "Periodic Streamwise Variations of Heat Transfer Coefficients for Inline and Staggered Arrays of Circular Jets with Crossflow of Spent Air", *ASME Journal of Heat Transfer*, Vol.102, pp.132-137.

[22] Florschuetz, L.W., Truman, C.R., Metzger, D.E., 1981, "Streamwise Flow and Heat Transfer Distributions for Jet Array Impingement with Crossflow", *ASME Journal of Heat Transfer*, Vol.103, pp.337-342.

[23] Goldstein, R.J., Behbahani, A.I., 1982, "Impingement of a Circular Jet With and Without Cross Flow", *International Journal of Heat and Mass Transfer*, Vol. 25, pp.1377-1382.

[24] Goldstein, R.J., Timmer, J.F., 1982, "Visualization of Heat Transfer from Arrays of Impinging Jets", *International Journal of Heat and Mass Transfer*, Vol.25, pp.1857-1868.

[25] Goldstein, R.J., Seol, W.S., 1991, "Heat Transfer to Row of Impinging Circular Air Jets Including the Effect of Entrainment", *International Journal of Heat and Mass Transfer*, Vol.34, pp.608-611.

[26] Goldstein, R.J., 2001, *Heat Transfer In Gas Turbine Systems*, Vol. 934, New York Academy of Sciences, New York.

[27] Byerley, A.R., 1989, *Heat Transfer Near the Entrance to a Film Cooling Hole in a Gas Turbine*, Doctoral Thesis, Department of Engineering Science, University of Oxford, UK.

[28] Hay, N., Lampard, D, 1998, "Discharge Coefficient of Turbine Cooling Holes: A Review", *ASME Journal of Turbomachinery*, Vol.120, pp.314-319.

[29] Gritsch, M., Schulz, A., Wittig, S., 2001, "Effects of Crossflows on the Discharge Coefficient of Film Cooling Holes with Varying Angles of Inclination and Orientation", *ASME Journal of Turbomachinery*, Vol.123, pp.781-787.

[30] Hay, N., Lampard, D., Benmansmour, S., 1983, Effects of Crossflows on the Discharge Coefficient of Film Cooling Holes, *ASME Journal of Engineering and Power*, Vol.105, pp.243-248.

[31] Aintsworth, R.W., Jones, T.V., 1979, "Measurement of Heat Transfer in Circular, Rectangular and Triangular Ducts, Representing Typical Turbine Blade Internal Cooling Passages Using Transient Techniques", ASME Paper No. 79-GT-40.

[32] Sparrow, E.M., Kemink, R.G., 1979, "Heat Transfer Downstream of a Fluid Withdrawal Branch in a Tube", *ASME Journal of Heat Transfer*, Vol.101, pp.23-28.

[33] Shen, J.R., Wang, Z., Ireland, P.T., Jones T.V., Byerley A.R., 1991, "Heat Transfer Coefficient Enhancement in a Gas Turbine Blade Cooling Passage Due to Film Cooling Holes*", Proceedings of the Institution of Mechanical Engineers European Conference on Turbomachinery: Latest Developments in a Changing Scene*, Bird Cage Walk, London, pp.219-226.

[34] Shen, J.R., Wang, Z., Ireland, P.T., Jones, T.V., Byerley A.R., 1996, Heat Transfer Enhancement within a Turbine Cooling Passage Using Ribs and Combinations of Ribs with Film Cooling Holes, *ASME Journal of Turbomachinery*, Vol.118, pp.428-434.

[35] Taslim, M.E., Li, T., Spring, S.D., 1995, "Experimental Study of the Effects of bleed Holes on Heat Transfer and Pressure Drop in Trapezoidal Passages with Tapered Turbulators", *ASME Journal of Turbomachinery*, Vol.117, pp.281-289.

[36] Ekkad, S.V., Huang, Y., Han, J.C.,1998, "Detailed Heat Transfer Distributions in Two Pass Smooth and Turbulated Square Channels with Bleed Holes", *International Journal of Heat and Mass Transfer*, Vol.41, No13, pp.3781-3791

[37] Thurman, D., Poinsatte, P., 2000, "Experimental Heat Transfer and Bulk Air Temperature Measurements for a Multipass Internal Cooling Model with Ribs and Bleed", *ASME Turbo Expo*, Munich, Germany, May 8-11, ASME Paper No. 2000-GT-233.

[38] Chanteloup, D., Bölcs, A., 2003, "Flow Effects on the Bend Region Heat Transfer Distribution of 2-Pass Internal Coolant Passages of Gas Turbine Airfoils: Influence of Film Cooling Extraction", *ASME Turbo Expo*, Atlanta, Georgia, USA, June 16-19, ASME Paper No. GT-2003-38702.

[39] Rigby, D.L., Steinhorsson, E., Ameri, A.A, 1997, "Numerical Prediction of Heat Transfer in a Channel with Ribs and Bleed", *ASME International Gas Turbine and Aeroengine Congress and Exhibition*, Orlando, Florida, June 2-5, ASME Paper No. 97-GT-431.

[40] Sonntag, R.E., Borgnakke, C., Van Wylen, G.J., 1998, *Fundamentals of Thermodynamics*, 5th Edition, John Wiley and Sons, New York.

[41] Goldstein, R.J., Taylor, J.R., 1982, "Mass Transfer in the Neighborhood of Jets Entering a Crossflow", *ASME Journal of Heat Transfer*, Vol.104, pp.355-362.

[42] Goldstein, R.J., Spores, R.A., 1988, "Turbulent Transport on the Endwall in the Region Between Adjacent Turbine Blades", *ASME Journal of Heat Transfer*, Vol.110, pp. 862-869.

[43] Goldstein, R.J., Wang, H.P., Jabbari, M.Y., 1995, "The Influence of Secondary Flows Near the Endwall and Boundary Layer Disturbance on Convective Transport from a Turbine Blade", *ASME Journal of Turbomachinery*, Vol.117, pp.657-663.

[44] Han J.C., Chandra P.R., Lau, S.C., 1988, "Local Heat/Mass Transfer Distributions Around Sharp 180° Degree Turns in Two-Pass Smooth and Rib-Roughened Channels", *ASME Journal of Heat Transfer*, Vol.110, pp.91-98.

[45] Mattern, C., Hennecke, D.K., 1996, "The Influence of Rotation on Impingement Cooling", *ASME International Gas Turbine and Aeroengine Congress and Exhibition*, Birmingham, UK, June 10-13, ASME Paper No. 96-GT-161.

[46] Park, C.W., Lau, S.C., 1998, "Effect of Channel Orientation of Local Heat (Mass) Transfer Distributions in a Rotation Two-Pass Channel with Smooth Walls", *ASME Journal of Heat Transfer*, Vol.120, pp.624-632.

[47] Hibbs, R., Acharya, S., Chen, Y., Nikitopoulos, D. E., 2000, "Mass/Heat Transfer in a Ribbed Coolant Passage with Cylindrical Vortex Generators: The Effect of Generator-Rib Spacing", *ASME Journal of Heat Transfer*, Vol.122, pp.641-652.

[48] Snedden, G.C., 1998, *The Use of Naphthalene and the Heat/Mass Transfer Analogy to Measure Heat Transfer Coefficients*, CSIR Report Aero 97/283, Council for Scientific and Industrial Research, Pretoria, South Africa.

[49] Dunn, M.G., 1995*, Measurement Techniques: The Thin Film Gauge*, VKI Lecture Series 1995-01, Von Karman Institute for Fluid Dynamics, Brussels, Belgium.

[50] Ligrani, P.M., Camci, C., Grady M.S., 1982, *Thin film heat transfer gage construction and measurement details*, VKI Technical Memorandum #33, Von Karman Institute for Fluid Dynamics, Brussels, Belgium.

[51] Schulz, D.L., Jones, T.V., 1973, *Heat Transfer Measurements in Short Duration Hypersonic Facilities*, AGARDograph Report 165.

[52] Denos, R., Billiard, N., Iliopoulou, V., Ferrara, F., 2002, "Data Reduction and Thermal Product Determination for Single and Multe-Layered Substrate Thin-Film Gauges", *The 16th Symposium on Measuring Techniques in Transonic and Supersonic Flow in Cascades and Turbomachines*, Cambridge, UK, September 23-24, VKI RP 2002-47.

[53] Snedden, G.C., 1995, *Transient Measurement of Heat Transfer in Steady State Turbine Cascades*, Masters Dissertation, Department of Mechanical Engineering, University of Natal, South Africa.

[54] Abdel-Wahab, S., Tafti D. K., 2004, "Large Eddy Simulations of Flow and Heat Transfer in a 90^{o} Ribbed Duct with Rotation - Effect of Coriolis Forces", *ASME Turbo Expo*, Vienna, Austria, June 14-17, ASME Paper No.GT-2004-53796.

[55] Sewall, E., Tafti, D. K., 2004, "Large Eddy Simulation of the Developing Region of a Stationary Ribbed Internal Turbine Blade Cooling Channel", *ASME Turbo Expo*, Vienna, Austria, June 14-17, ASME Paper No.GT-2004-53832.

[56] He, G., Guo, Y., and Hsu, A.T., 1999, "The Effect of Schmidt Number on Turbulent Scalar Mixing in a Jet-in-Crossflow", *International Journal of Heat and Mass Transfer*, Vol.42, pp.3727-3738.

[57] C.H. Edwards, D.E. Penney, 2000, *Elementary Differential Equations*, 4th Edition, Prentice Hall, New Jersey.

[58] Mills, A.F.,1999, *Basic Heat and Mass Transfer*, 2nd Edition, Prentice Hall, New Jersey.

[60] Oldfield, M.L.G., Burd, H.J., Doe, N.G., 1981, "Design of Wide-Bandwidth Analogue Circuits for Heat Transfer Instrumentation in Transient Tunnels", OUEL Report No. 1382/81, Department of Engineering Science, University of Oxford.

[61] Oldfield, M.L.G., Jones, T.V., Schultz, D.L., 1978, "On-Line Computer for Transient Turbine Cascade Instrumentation", *IEEE Transactions on Aerospace and Electronic Systems*, Vol.AES-14, No.5, pp.738-749.

[62] Meyer, R.F., 1963, "Further Comments on Analogue Networks to Obtain Heat Flux From Surface Temperature Measurements", *NRC Aeronautical Report*, LR-375, File: M49-7-34.

[63] Cook, W.J., Felderman, E.J., 1966, "Reduction of Data from Thin Film Heat Transfer Gauges: A Concise Numerical Technique", *AIAA Journal*, Vol.4, pp.561-562.

[64] Burden, R.L, Faires, J.D., 2001, *Numerical Analysis*, 7th Edition, Brooks&Cole.

[65] Matthews, J.H., Kurtis, D.F., 1999, *Numerical Methods Using Matlab*, 3rd Edition, Prentice Hall, New Jersey.

[66] Patankar, S.V., 1980, *Numerical Heat Transfer and Fluid Flow*, McGraw-Hill, New York.

[67] White, F.M.,1991, *Viscous Fluid Flow*, 2nd Edition, McGraw-Hill, New York.

[68] Skinner, G.T., 1961, "Calibration of Thin Film Gage Backing Materials", *Journal of the American Rocket Society*, Vol.31, No 5, pp.671-672.

[69] Kline, S.J, McClintock, F.A, 1953, "Describing Uncertainty in Single Sample Experiments", *ASME Journal*, Vol.75, pp.3-8.

[70] Skinner, G.T., 1961, "Calibration of Thin Film Gage Backing Materials", *Journal of the American Rocket Society*, Vol.31, No 5, pp.671-672.

[71] Bredberg, J., 2002, *Turbulence Modelling for Internal Cooling of Turbine Blades*, Doctoral Thesis, Department of Thermo and Fluid Dynamics, Chalmers University of Technology, Sweden.

[72] Spalart, P., Allmaras, S., 1992, "A One-Equation Turbulence Model for Aerodynamic Flows", *AIAA Paper* No. 92-04391992.

[73] Launder, B.E., Spalding, D.B., 1972, *Lectures in Mathematical Models of Turbulence*, Academic Press, London.

[74] Wilcox, D.C., 1998, *Turbulence Modeling for CFD*, DCW Industries Inc., La Canada, California.

[75] Menter, F.R., 1994, "Two-Equation Eddy-Viscosity Turbulence Models for Engineering Applications", *AIAA Journal*, Vol.32, pp.269-289.

[76] Launder, B.E., Reece G.J., Rodi, W., 1975, "Progress in the Development of a Reynolds-Stress Turbulence Closure", *Journal of Fluid Mechanics*, Vol.68, pp.537-566.

[77] Shur, M., Spalart, P. R., Strelets, M., Travin A., 1999, "Detached-Eddy Simulation of an Airfoil at High Angle of Attack", *4th International Symposium on Engineering Turbine Modeling and Experiments*, Corsica, France, May 24-26.

[78] Spalding, D.B., 1961, A Single Formula for the Law of the Wall, *Journal of Applied Mechanics*, Vol.28, pp.455-457.

[79] Launder, B.E., Spalding, D.B., 1974, "The Numerical Computation of Turbulent Flows", *Computer Methods in Applied Mechanics and Engineering*, Vol.3, pp.269-289.

[80] Kim, S.E., Choudhury, D., 1995, "A Near-Wall Treatment Using Wall Functions Sensitized to Pressure Gradient", *ASME FED*, Vol. 217, Separated and Complex Flows.

[81] Patankar, S. V., Baliga, B.R., 1978, "A New Finite Difference Scheme for Parabolic Differential Equations", *Numerical Heat Transfer*, Vol.1, pp.27-37.

APPENDIX A

IMPLICIT FINITE DIFFERENCE SOURCE CODE

A numerical technique, using the Crank-Nicholson scheme, was implemented to predict the internal substrate temperature distribution. The scheme made use of the measured surface temperatures as a boundary and it was assumed that the substrate represented a semi-infinite solid. The program listing in Matlab is given below.

```
%%%%%%%%%%%%%%%%%%%%%%%%%%%%%%%%%%%%%%%%%%%%%%%%%%%%%%%%%%%%%%%%%%%%%%%%%%%%
%                                                                              %
% The following code implements the Crank-Nicholson implicit finite           %
% difference algorithm to predict the temperature profile within a             %
% semi-infinite substrate.                                                     %
%                                                                              %
% Programmed by G Scheepers                                                    %
% Updated: June 2005                                                           %
%                                                                              %
%%%%%%%%%%%%%%%%%%%%%%%%%%%%%%%%%%%%%%%%%%%%%%%%%%%%%%%%%%%%%%%%%%%%%%%%%%%%

clear all;
close all;

% Specify the following constants

alfa = ;              % Thermal diffusivity of the substrate
sub_depth = ;         % Discretization depth
n = 0.5;              % Weighting factor
delt = ;              % Timestep size
el_size = ;           % Number of elements
in_T =;               % Initial temp [K]
timesteps = ;         % Number of timesteps

x = (dlmread('Discret.txt',0: '\t'));   % Substrate discretization
j = 1;

T_bound = (dlmread('Temp_bound.txt','\t')); % Temperature boundary
T_bound = T_bound+273;

T =in_T*ones(length(x),length(T_bound));
T(1,1:length(T_bound)) = T_bound; %1:length(T);       % Upper Boundary

for j = 1:length(T)-1
```

```
    for i = 2:length(x)-1

        % A-Value

    if i == 2
            a(i-1) = 0;
        else
            a(i-1) = ((-alfa)*n)/((x(i+1)-x(i))^2);
        end

        % B-Value

    b(i-1) = (1/delt + (2*alfa*n)/((x(i+1)-x(i))^2));

        % C-Value

    if i == (length(x)-1)
            c(i-1) = 0;
        else
            c(i-1) = (((-alfa)*n)/((x(i+1)-x(i))^2));
        end % End C- Value

        % D-Value

    if i == 2
            d(i-1) = T(i,j)/delt...
                    + (alfa*(1-n)*T(i+1,j))/((x(i)-x(i+1))^2)...
                    - (2*alfa*(1-n)*T(i,j))/((x(i)-x(i+1))^2)...
                    + (alfa*(1-n)*T(i-1,j))/((x(i)-x(i+1))^2)...
                    - (((-alfa)*n)/((x(i+1)-x(i))^2))*T(i-1,j+1);
            else

                if i == (length(x)-1) % Sub D-Value

                    d(i-1) = T(i,j)/delt...
                           +(alfa*(1-n)*T(i+1,j))/((x(i)-x(i+1))^2)...
                           -(2*alfa*(1-n)*T(i,j))/((x(i)-x(i+1))^2)...
                           +(alfa*(1-n)*T(i-1,j))/((x(i)-x(i+1))^2)-...
                           -(((-alfa)*n)/((x(i+1)-x(i))^2))*T(i+1,j+1);
                    else
                        d(i-1) = T(i,j)/delt...
                           +(alfa*(1-n)*T(i+1,j))/((x(i)-x(i+1))^2)...
                           -(2*alfa*(1-n)*T(i,j))/((x(i)-x(i+1))^2)...
                           + alfa*(1-n)*T(i-1,j)/((x(i)-x(i+1))^2);
                    end % End Sub D-Value


                end % End D-Value


            end % End i-loop


% Crout Factorization

    for i = 1:length(x)-2
```

```
        A(i,i) = b(i);

        if i > 1
            A(i,i-1) = a(i);
        end

        if i < (length(x)-2)
            A(i,i+1) = c(i);
        end

    end  % End A-Matrix

    A(1:(length(x)-2),length(x)-1) = d';

    l(1,1) = A(1,1);
    u(1,2) = A(1,2)/l(1,1);
    z(1) = A(1,length(A))/l(1,1);

    for i = 2:length(A)-2
        l(i,i-1) = A(i,i-1);
        l(i,i) = A(i,i)-l(i,i-1)*u(i-1,i);
        u(i,i+1) = A(i,i+1)/l(i,i);
        z(i) = (A(i,length(A))-l(i,i-1)*z(i-1))/l(i,i);
    end

    i = length(A)-1;

    l(i,i-1) = A(i,i-1);
    l(i,i) = A(i,i) - l(i,i-1)*u(i-1,i);
    z(i) = (A(i,i+1) - l(i,i-1)*z(i-1))/l(i,i);

    xx(i) = z(i);

    for i = length(A)-2:-1:1
        xx(i) = z(i) - u(i,i+1)*xx(i+1);
    end

    T(2:length(x)-1,j+1) = xx';

end

dlmwrite('GT.txt',T(1:2,1:length(T))','\t');
```